MOLECULAR MODELING OF NANOPARTICLE INTERACTIONS WITH SOFT COMPLEX INTERFACES

By

SEAN MACKENZIE BURGESS

A dissertation submitted to the

School of Graduate Studies

Rutgers, The State University of New Jersey

In partial fulfillment of the requirements

For the degree of

Doctor of Philosophy

Graduate Program in Chemical and Biochemical Engineering

Written under the direction of

Alexander V. Neimark

And approved by

_____

_____

_____

_____

_____

New Brunswick, New Jersey

January, 2020

ABSTRACT OF THE DISSERTATION

MOLECULAR MODELING OF NANOPARTICLE INTERACTIONS WITH SOFT COMPLEX INTEFACES

By SEAN MACKENZIE BURGESS

Dissertation Director:

Alexander V. Neimark

Understanding the interactions between nanoparticles (NP) and soft, complex interfaces, such as lipid bilayers (LB), and high-density polymer grafted substrates, is important for many biological, and technological processes, as well as for assessing health threats related to nanoparticle commercialization. Adhesion, intake, and release of hydrophobic NPs by 1,2-dimyristoyl-*sn*-glycero-3-phosphocholine bilayers are explored, and the dynamics of unforced transport of NP across the LB is evaluated. NP intake may also cause cell instability that is studied by modeling the dynamics of the tension-induced hole formation in Np-loaded LBs. An NP size dependent relationship is established for the probability of membrane rupture within a given time as a function of the membrane tension. Next, the NP motion in polymer brush (PB) grafted channels is explored focusing on the process on NP chromatographic separation. . The existing theory, which considers NP motion in hard-wall channels with is extended for the case of PB-grafted substrates. Additionally, separation experiments are performed to develop a hybrid liquid chromatography model, which combines the hydrodynamic and size-exclusion chromatography approaches to predict the residence time in polymer-grafted chromatographic columns.

ACKNOWLEDGEMENTS

I would like to acknowledge everyone who has helped me along the way whether named or not. I first want to thank my parents for encouraging my intellectual curiosity and helping me turn it in to a career. I want to thank all of my lab mates for the lengthy discussion about both science, and definitely not science. For their guidance and assistance for when I did not have the motivation, I want to thank Dr. Chris Rasmussen, Dr. John Landers, and Dr. Richard Cimino, and Dr. Ming-Tsung Lee. To my committee, Professor Yee Chiew, Professor Meenakshi Dutt, and Professor Aleksey Vishnyakov for their time and support with this process. I further would like to acknowledge Professor Aleksey Vishnyakov for his guidance, assistance, mentorship, and friendship during his time at Rutgers University. He helped me in my scientific endeavor more than I can express. Thank you to my advisor, Professor Alexander V. Neimark. Our lengthy discussions about all these topics below has taught me how to think thoroughly through a problem and defend my ideas. Through your patience, guidance, and direction I have learned an immeasurable amount, and I continue to learn from you as I write this.

Finally, I would like to thank my wife Andree. I would bet she is more knowledgeable about the content of my dissertation than almost anyone. She has listened to me practice all of my presentations, has sat patiently with me during my times of frustration, and has carried my emotional burden when I can't. Throughout this entire process she has been my partner, teacher, student, colleague, and most importantly, my friend. Thank you.

DEDICATION

This work is dedicated to my wife Andree who has helped me become a better communicator, listener, and person.

TABLE OF CONTENTS

LIST OF FIGURES

LIST OF TABLES

1 Background and Motivation

1.1 Introduction to Molecular Modeling of Nanoparticle Interactions with Soft Complex Interfaces

Until a physical unifying theory is developed, every mathematical description of a physical process is an estimation. Therefore, the question when describing a process of interest is "How much of an estimation is acceptable?" The goal is to choose a system with enough precision to observe the phenomena of interest, but not so precise that the simulation takes too long for the phenomena to occur. For example, when describing a chemical reaction, the mathematics must describe probability functions of sub-atomic particles,[1] but when describing how a macroscopic system behaves or flows, this level of precision is not required and systems may be described using Navier-Stokes.[2] In between these two scales lies the so called mesoscale, a scale which is larger than a purely atomistic description, but still small enough to describe the system atomistic behavior.[3, 4] In general, the mesoscale ranges from 10 to 10,000 nm, within a time scale of 1 to 1 million ns.[5]

One of the most widely used mesoscale technique is called dissipative particle dynamics (DPD),[6, 7] which has been employed to a very wide range of systems including complex fluids, fluid flow, and soft complex interfaces.[4] DPD requires atoms to be clumped together into a single unit or bead. This clumping, or coarse-graining (CG), is central to the DPD efficiency, as it decreases the simulation time by about 1000 $N_m^{8/3}$, where N_m is the number of molecules per bead.[8] For example, in this project N_m=3 or 4, indicating a decrease in simulation time by a factor of $2\text{-}4*10^4$ when compared to a fully atomistic simulation method such as molecular dynamics. The speed-up is due to both the

decrease in the number of objects to iterate over and the change from hard-core Lennard-Jones interactions to soft CG interactions.[9] Because DPD is a powerful simulation technique that has already been employed to study nanoparticle-lipid bilayer interactions[8, 10-13] and nanoparticle-polymer brush interactions, the focus of this work, it is the main computational technique employed.[14, 15]

DPD uses Newton's equations of motion to monitor equilibrated positions. The force on a bead '*i*' is calculated using (1.1)

$$dr_i/dt = \mathbf{v}_i; \quad dv_i/dt = \mathbf{f}_i; \quad \mathbf{f}_i = \sum_{j\neq i}\left(\mathbf{F}_{ij}^{(\mathrm{C})} + \mathbf{F}_{ij}^{(\mathrm{B})} + \mathbf{F}_{ij}^{(\mathrm{R})} + \mathbf{F}_{ij}^{(\mathrm{D})}\right) \quad (1.1)$$

All components are typically represented by beads of the same size and interact by linear short-range soft repulsive forces.

$$\mathbf{F}_{\mathrm{ij}}^{\mathrm{C}} = \begin{cases} -a_{\mathrm{ij}}\left(1 - \left|r_{\mathrm{ij}}\right|/R_c\right)\hat{r}_{\mathrm{ij}} \text{ if } \left|r_{\mathrm{ij}}\right| \leq R_{\mathrm{c}} \\ 0 \qquad\qquad\qquad\qquad \text{if } \left|r_{\mathrm{ij}}\right| > R_{\mathrm{c}} \end{cases} \quad (1.2)$$

where a_{ij} represents the repulsion strength and R_{c} the effective bead diameter assumed equal for all bead types. Lipid beads are connected using harmonic bonds $\mathbf{F}_{ij}^{(\mathrm{B})} = -K_i^{(\mathrm{B})}\left(r_{ij} - r_{\mathrm{e}}\right)\hat{r}_{\mathrm{ij}}$ where $K_i^{(\mathrm{B})}$ is the spring constant and r_{e} is the equilibrium spring position. Random and drag forces are implemented using a Langevin thermostat[16]

$$\mathbf{F}_{ij}^{(\mathrm{R})} = \sigma w^{(\mathrm{R})}\left(r_{ij}\right)\theta_{ij}(t)\hat{r}_{ij}; \quad \mathbf{F}_{\mathrm{ij}}^{(\mathrm{D})} = -\gamma w^{(\mathrm{D})}\left(r_{ij}\right)\left(\hat{r}_{ij}\cdot v_{ij}\right)\hat{r}_{ij} \quad (1.3a)$$

$$w^{(\mathrm{D})}\left(r_{ij}\right) = \left[w^{(\mathrm{R})}\left(r_{ij}\right)\right]^2; \quad \sigma^2 = 2\gamma k_{\mathrm{B}}T \quad (1.3b)$$

where $\theta_{ij}(t)$ is a randomly fluctuating variable with Gaussian statistics.

1.2 Molecular Modeling of Nanoparticle Interactions with Lipid Bilayers

Understanding of the physico-chemical mechanisms of nanoparticle (NP) adhesion to soft interfaces like lipid bilayers (LB), which constitute the foundation of cell membranes, is of importance for development of biomedical nanotechnologies (biomedical imaging and drug delivery[17]) as well as for the design of new biomimetic materials and devices[18]. For example, mesoporous silica NPs are employed as intracellular delivery vehicles for controlled release of drugs and other membrane-impermeable chemicals.[19, 20] The knowledge of NP-LB interactions is also important for predictions of health threats related to NP manufacturing as adhesion of inhaled or digested nanoparticles may lead to membrane rupture and cell apoptosis[21, 22]. In many cases, NP adhesion to cell membranes is mainly affected by physico-chemical factors such as particle size and shape, hydrophobicity, charge density, and physisorption of lipids and proteins rather than by specific biochemical interactions[23-25]. Lu et al.,[23] who measured the rates of silica NPs trans-membrane penetration into HeLa cells, found a non-monotonic penetration dependence on the particle size with a maximum at ~50 nm. A prominent effect of nanoparticle porosity on membrane adhesion has been reported by and Lin and Haynes.[24] They found a sizable difference between nonporous and porous silica particle leading to the damage of red blood cells. These and many other experimental observations of the specifics of interfacial interactions of NPs with lipid membranes are still poorly understood, and their effects are hardly predictable by using classical approaches of interfacial and colloid science.

Smith et al.,[10] Alexeev et al.,[11] Ginzburg et al.,[12] and Djohari & Dormidontova[13] demonstrated the feasability of DPD modeling of NP adhesion to and engulfing by LBs.

Yang and Ma[26] employed DPD to demonstrate translocation of NPs through lipid membranes. NP sizes were comparable to membrane thickness and shapes varied. For very small hydrophobic NPs, the energy barriers for encapsulation are low and their transport can be followed in a straightforward manner through coarse-grained simulations.[27-29] Such NPs tend to penetrate into the hydrophobic core of the LB and accumulate there, as observed in simulations and experiments alike.[30-32]

Ding et al.[33] studied translocation of hydrophylic NPs of varied shapes and sizes. NPs were functionalized with reactive amphiphilic ligands that were able to dissociate from the NP and dissolve in the LB on demand, effectively changing NP surface from hydrophobic to hydrophilic. The NPs first eneterd into the hydrophobic LB core due to favorable interactions between the ligands and lipid tails and and then exited as the ligands peeled off. The authors estimated translocation probability and characteristic time at varying ligand density, NP shape and NP size. Yue et al. also conducted a study focusing on NP translocation, but used rotating NPs to interact with lipid bilayers; they observed transport of NPs across the LB and estimated the translocation time by monitoring the number of DPD time steps.[34] Two scenarios were encountered in this study: NP encapsulation within the LB or LB rupture.

In many cases, transport of NPs through LBs is too slow to be directly followed in coarse grained simulations. The mechanisms and dynamics of NP transport can be elucidated from the free energy landscapes: dependence of the free energy on the particle position with respect to the LB. Fiedler et al.[28] employed a constraint force method to move hydrophobic NPs (C60 fullerenes and their fragments) through a tensionless LB. The force acting on the NP was pre-set and the simulation run until an equilibrated NP position was

established. The constraint force method is used in depth to study various NP-LB systems[35-37] because it is convenient in relatively simple systems, but can lead to incomplete scanning of the free energy profile if the latter is complex and feature multiple meta- and un-stable regions. Li et al.[38] explored free energy landscapes for encapsulation of ligand-functionalized NPs into tensionless LBs. The authors effectively tethered the NP to a point in space using a harmonic potential and explored the free energy landscape of NPs in the vicinity of the LB. The NPs were functionalized with pure hydrophobic ligands, pure hydrophilic ligands, and hydrophobic-hydrophilic ligand mixtures. NP diameter was slightly smaller than LB thickness. The more hydrophobic the ligand beads, the easier the NP entered the LB. It was not exactly clear whether the membrane in such an experiment is tensionless: the LB was attached to immobile anchors and deformed in the course of a simulation; thus, the surface tension may have varied. Guo et al.[32] reported investigation into lipid-coated hydrophobic NP penetration into LBs. Simulation observations were interpreted with free energy landscapes obtained with single-chain mean field theory[39] that are consistent with the experiments. Small (<5nm) lipid-covered hydrophobic NPs tended to get encapsulated inside the LB; larger NPs tended to create an opening in the membrane and penetrate through with characteristic time in the order of milliseconds.

Published modeling studies mostly considered NPs of sizes similar to the thickness of the LB, but the free energy landscape of these systems under constant surface tension remains unclear .[40] Another little explored factor that influences NP – LB interactions is the chemical potential of lipid molecules which is directly related to the surface tension of the membrane. In a practical situation (e.g. during NP transport across a cell membrane) it is the surface tension of the membrane (and, correspondingly chemical potential of the lipid

molecules) that remains constant, because a cell is large compared to a NP. The following chapters address the practically important questions: how the nanoparticle size and hydrophobicity affect its encapsulation and release from LB, and how an encapsulated nanoparticle effect LB stability.

1.3 Nanoparticle Flow in Polymer Grafted Channels

Nanoparticle (NP) flow in channels grafted with polymer chains is important for many biological and technological processes, including membrane separations,[41] fabrication of biomedical devices, sensors, and nanocomposites,[42-45] colloidal stabilization,[46, 47] and motion induction of nano-objects and nanofluidics.[48] Of practical relevance to NP flow in pore channels are traditional analytical techniques of NP separations, such as field flow fractionation,[49-51] size exclusion chromatography (SEC),[52-54] and hydrodynamic chromatography (HDC).[55] Modification of channel walls with polymer brushes (PB) greatly improves the precision of NP separation.[15, 56-60] The PB makes the pore wall 'soft' and provides additional functionalities for NP selective adhesion and separation. While the general problem of nanofluidic separations and particle motion in pores with hard walls has been studied extensively both theoretically and experimentally,[61-66] the specifics of NP flow in pores with soft PB-grafted walls remain unexplored. In this work, we study NP flow in PB-grafted channels by using the dissipative particle dynamics (DPD) and determine the scaling relationship between the NP and solvent velocities, which depends on the geometrical parameters of the systems: effective dimensions of the channel, PB, and NP.

The traditional approach considers NP transport within the Poiseuille solvent flow in cylindrical or slit-shaped channels with smooth hard walls.[55] Moving with the solvent, a hard particle is excluded from the near-wall slow-motion region at the distance equaled to its radius, R_{NP}, and experiences a slip along the walls. As shown by various theoretical methods and confirmed experimentally, the average NP velocity, $\bar{u}_{NP}$, is related to the average solvent velocity, $\bar{u}_{solv}$, according to the following scaling equations, derived for slit-shaped and cylindrical channels, respectively,

$$\bar{u}_{NP}/\bar{u}_{slit} = (1 + \lambda - C\lambda^2/2)^{-1} \quad (1.1a)$$

$$\bar{u}_{NP}/\bar{u}_{cyl} = (1 + 2\lambda - C\lambda^2)^{-1} \quad (1.1b)$$

where the scaling factor $\lambda = R_{NP}/w_H$, the ratio of the effective NP radius to the channel hydrodynamic half-width/radius, w_H, and C is an adjustment parameter, which depends on the particle shape and nature. In this work, we consider only spherical particles. In principle, this theory is extendable for non-spherical or penetrable particles like polymers in solutions where the particle radius is defined by its hydrodynamic radius.

With an intuitive yet incorrect supposition that a NP assumes the velocity of the solvent at the position of the NP center of mass, one easily comes to Eqs.1 with $C = 1$, by integrating the parabolic velocity profile in the limits of $\pm(w_H - R_{NP})$. In practice, the values of C do not equal 1, and the NP lags behind the solvent due to a variety of affects, most predominantly, NP rotation caused by the inhomogeneous solvent flow and interaction of the NP with the wall. The parameter C is used to account for this lagging affect. To explain how the NP flows and rotates in a channel, the problem is often split up in to two parts – NP flow in the center of the channel far from the channel wall, and NP flow near the channel wall. When the NP flows in the channel far from the wall, the

solvent velocity across its diameter is not constant; solvent velocity on the NP edge closest to the wall is slower than that farther from the wall. This causes the NP to rotate, creating a slowing affect. When the NP flows near the channel wall, the rotation, and consequently the slowing affect becomes more pronounced. Considering flow in infinitely long cylindrical channels with hard walls, the theoretical work by Brenner and Gaydos[62] suggested $C = 4.9$ for hard impermeable spheres that was further confirmed experimentally.[55] Staben et al.[66] theoretically derived an equation for the particle velocity profile in a slit pore with hard walls, which was experimentally confirmed in the subsequent work by Staben & Davis[67] on polystyrene spheres. Their results fulfill (1.1a) with the parameter $C \approx 2.6$. More complex models exist which consider higher order correction terms to (1),[68-70] however, within the precision of the present study, accuracy between the models cannot be assessed. Dechadilok and Dean[68] provide an in depth discussion of these various models and their differences. It is important to note that in the case of soft particle, e.g. polymer coils and globules, the value of *C* is significantly smaller compared to solid particles, as predicted by theory and experiment alike.[55, 61, 63-65] For example, DiMarzio and coworkers[63-65] have shown that $C \approx 2.7$ for dilute polymer solutions in cylindrical channels, a widely accepted value which has been experimentally verified.[55, 61] Recently, Korolev et al.[71] experimentally measured the velocity of polystyrene standards in capillary columns, finding $C = 2.4$.

In the case of packed bed columns, Eq. 1.1b is commonly employed with the effective hydrodynamic channel width, equaled to the diameter of the cylindrical channel having the same surface to volume ratio as the column.[55, 71, 72] The value of parameter C depends on the column structure and the nature of particles. Tijssen et al.[72] recommend,

based on empirical evidence, the value of $C \approx 2.7$ for calculating the elution time of polymeric coils in HDC. Stegeman et al.[73] studied flow of polystyrene standards in packed bed columns. The columns were packed with non-porous beads of size 1.4, 1.9 and 2.7 μm. The authors found $C \approx 3.7$ best fit the data across the packed bead size. Appreciable differences are found in monolith columns. Compared to packed bed columns, monolith columns have a more regular channel structure.[74] Edam et al.[75] studied flow of polystyrene standards through polymer based monolithic columns. While they do not conclude which value of C is most suitable, from the figures presented, it appears that the value of *C* slightly smaller than 2.7 would best fit their data.

Santo et al.[15, 57] has previously shown that in a polymer grafted channel, the same quadratic profile that is observed in a hard-walled channel is observed. However, to what extent the polymer grafted channel effects the standard assumptions previously describe that lead to (1.1) remains to be seen and is the focus of Chapter 5.

1.4 Chromatographic Application

In the past few decades utilization of monolith columns, both silica-[76, 77] and organic-based,[78] as effective alternative to packed columns for HPLC-type purification and separations, has surged because of their more regular pore structure when compared to packed columns.[77, 79, 80] Monoliths have a continuous porous structure often grown within the confines of a solid column frame. They are made either by polymerization of an organic polymer (organic-based monoliths), or by a sol-gel process (silica based monoliths). Their structure, a single sponge-like skeleton,[81, 82] tends to have a bimodal pore distribution – a macropore region where pore size is on the order of thousands of nanometers, and a mesopore region where pore size is on the order of ten nanometers.[83-85]

The bimodal structure provides monolith columns with the opportunity to be quite effective for separation which combine both SEC and HDC. An illustration of the bimodal pore distribution is presented in Figure 1.1.

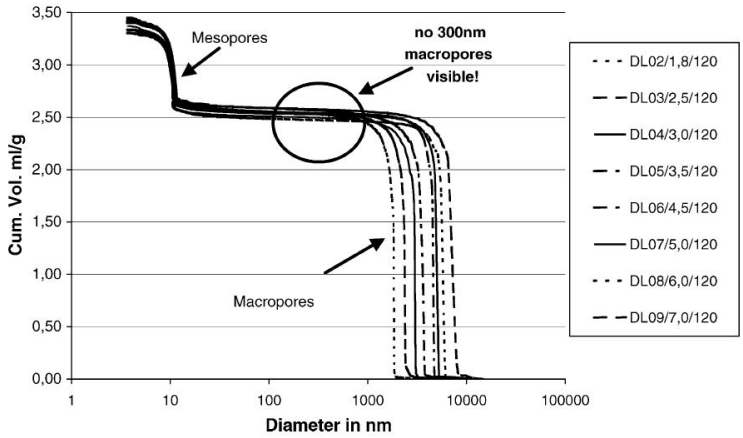

Figure 1.1 – Determination of eight variations (1.8, 2.5, 3.0, 3.5, 4.5, 5.0, 6.0 and 7.0 μm) of macropores using mercury porosimetry.[83]

When compared with their packed bead counterparts, monolith columns have major advantages. Their relatively constant radius flow-through channels[74] and sponge-like skeleton, effectively combines the best aspects of packed and capillary columns while mitigating the downsides. As in a packed column, the particle path length per unit length of column in a monolith is large when compared to a capillary column so adequate separation is observed for relatively short time. The many potential paths the particle can take can effectively act as many parallel channels, preventing column overloading and allowing particle concentration to be on par with packed columns. However, in a capillary column, there is only one path the particle can take, therefore they are easily overloaded. Like capillary columns, monolith columns have a much more regular channel (interstitial space) when compared to packed columns. As a result, monolith columns do not easily become plugged, significantly decreasing the back pressure. Smaller back

pressure allows for higher flow rates and much faster experiments when compared to packed bead columns.[86]

Despite the advantages over existing HDC columns, monolith columns have predominately been used for HPLC-type separations, and only recently have the polymer-based monoliths were analyzed for HDC-type separations.[75, 78, 87, 88] Using monoliths for hybrid separation has been attempted,[58, 87, 88] but on organic-based monoliths using polymer standards. As of yet, no one has implemented this approach on complex polymers such as starch. It is worth noting that commercially available organic-based monoliths have very small mesopore volumes which prevents their use for SEC separation. Also, the absence of a reliable theory of hybrid chromatography could help in the selection of the appropriate column and chromatographic conditions. Because of their large mesopores we use commercially available silica monoliths to study hybrid separations.

1.5 Internship at DuPont

During my Ph.D I also participated in the Grant Opportunities for Academic Liason with Industry (GOALI) internship program sponsored through the National Science Foundation. The goal of this program is to "improve the nation's capacity for intellectual and economic growth by increasing the number of industrial partnerships and collaborations." The GOALI proposal is an independent proposal that requires an industrial partner who will contribute to 'fundamental research.' An additional request made be made which provides supplemental funding for a student interested in conducting research in an industrial setting. This additional request must support the

original GOALI proposal, while providing the student experience in an industrial setting. The details and results of the internship are described in detail in Chapters 6 and 7.

1.6 Research Objectives and Structure of Dissertation

In this work, I attempt to better understand how nanoparticles interact with soft complex interfaces. This question was explored with two main thrust – NP interactions with LBs, and NP flow (and interaction with) polymer grafted channels. Chapters 2-4 cover the former topic, while chapters 5-7 cover the latter,

In chapter 2 I develop simulation tools and novel setups in order to probe NP interactions with LBs and develop free energy landscapes for NP translocation. The goal of these tools is to thoroughly understand how NP size effects the free energy landscape of intake and release. Additionally, these tools are used to qualitatively understand the processes associated with intake and release of the NP. Finally, the free energy results are used to understand NP-LB translocation dynamics through mathematical analysis. The mathematical analysis reveals interesting and significant differences with respect to the time of intake and release.

In chapter 3 I use the tools that were developed in chapter 2 to investigate how LB stability is affected by NP encapsulation. An existing model which describes membrane stability in the absence of a NP is extended to describe the relationship between NP size & shape and LB stability.

In chapter 4, a new set of tools is developed to investigate how LBs interact with supported LBs both with and in the absence of NPs on the substrate surface. The tools require a very large system which necessitates an implicit solvent model, requiring the

development of a model to describe the disjoining pressure between the LB and substrate. With these tools, the effect of NP size and hydrophobicity on a supported LB is investigated. A qualitative understanding to describe pore structure development is developed.

In chapter 5 the overarching topic moves to NP flow with polymer grafted channels. I investigate how the standard theories which describe NP flow in a channel are affected by grafting of a polymer brush to the channel wall. The results from the simulations are compared with experiments so a quantitative comparison between the two systems and two scales can be established.

In chapter 6 I describe my internship at DuPont. This chapter includes data and small projects that are not incorporated into the main 5 projects of this dissertations. Such projects include developing tools to create log-normal particle distributions and calculating the radius and diameter of cylindrical particles using dynamic light scattering. This chapter also briefly describes the work that is described in chapter 7.

In chapter 7 I describe the chromatography work conducted at DuPont. The goal of this project was two-fold. First, I sought to develop a mathematical model that properly described separations in monolith columns. With this model successfully developed, the columns are used to demonstrate their ability to separate complex mixtures such as potato starch.

Finally, in chapter 8 the conclusions of the previous chapters are summarized.

2 Adhesion, Encapsulation, and Release of Nanoparticles by Lipid Bilayers

This chapter is based on work that has been published to the reference shown below, and was used within the author rights as established with publishing company:

- Burgess, S., et al. Adhesion, Encapsulation, and Release of Nanoparticles by Lipid Bilayers. *JCIS* **2020,** 561, 58-70

2.1 Background and Motivation

In this section, we explore adhesion, encapsulation, and release of hydrophobic NPs by a 1,2-dimyristoyl-*sn*-glycero-3-phosphocholine (DMPC) LB. In contrast to earlier works, a novel simulation setup is developed that keeps the LB at a constant surface tension. The "Ghost Tweezers" (GT) method is employed in order to probe the force and free energy landscapes of encapsulation and release for a hydrophobic NP with adsorbed equilibrium lipid monolayer (LM). Using our original setup, a constant surface tension is applied to the LB which allows the lipids to be freely exchanged between LB and solution. This condition is equivalent to the condition of chemical potential constancy of the LB at constant surface tension. Additionally, Fokker-Planck (FP) analysis is used to study the dynamics of NP encapsulation and release from the LB.

2.2 Models and methods

2.2.1 Lipid, Water Models, and Interaction Parameters

The coarse-graining scheme and interaction parameters for lipid and water models are adopted from the work of Groot and Rabone.[89] Water is represented by water beads "W" of the effective radius, R_c = 0.645 nm comprised of 3 water molecules. The DMPC

molecule is dissected into 11 fragments of similar volume represented by 11 beads of the same effective radius, R_c, as the water bead, Figure 2.1.

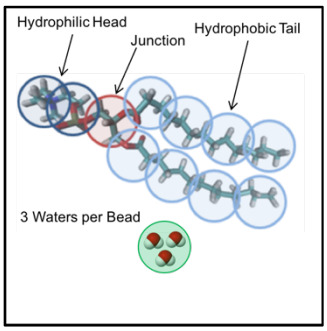

Figure 2.1– Left: Coarse grained model of DMPC composed of 2 hydrophilic 'H' head beads, 1 'J' junction bead, and 8 hydrophobic 'T' tail beads. Water bead "W" contains 3 water molecules.

The zwitterionic choline-phosphate head is represented by two hydrophilic 'H' beads. The carboxyl junction is represented by one semi-hydrophobic 'J' bead, and the two aliphatic tails are represented by 4 'T' beads each. The intra-component self-repulsion parameter, $a_{ii} = a_{WW} = 78$, is the same for all types of beads and secures the density and compressibility of water. The intercomponent repulsion parameters, a_{ij}, are chosen to account for the respective beads hydrophilicity (a_{iW} smaller of equal a_{WW}) or hydrophobicity (a_{iW} larger a_{WW}). It is worth noting that Groot & Rabone[89] modeled 1,2-dipalmitoylphosphatidylcholine (DPPC), whereas we model DMPC, the only difference being the DMPC model has one less bead per tail.

To verify the model validity, the surface tension was varied within the experimentally tested range of -2 to 4 pN/nm. The comparison between the simulation results is presented in **Error! Reference source not found.**.[90, 91] We conclude that our model very reasonably reproduced the experimental density and elasticity of freestanding DMPC LB's.

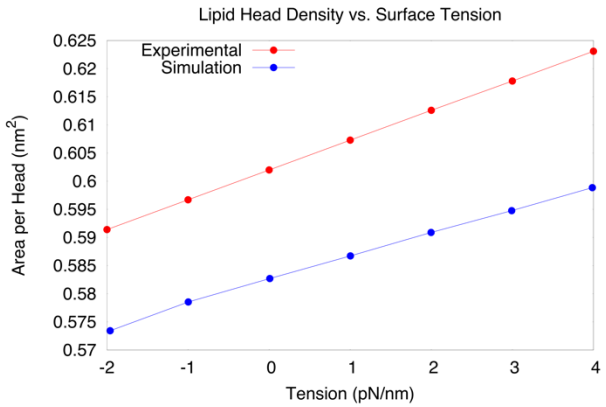

Figure 2.2 - Area per lipid as a function of membrane surface tension[92]

The force-field parameters between the beads of different types are listed in Table 2.1.

Table 2.1 – Parameters for repulsion and harmonic bond interactions. Bead types: H – lipid head; J – lipid junction; T – lipid tail; F – frame; R – roller bar; W – water; U – upper part of pulling bar; B – bottom part of pulling bar; S – outer shell of NP; C - inner core of NP; G – ghost NP. Note that for NP-GT bonds, $MK^{(B)}$ *rather than $K^{(B)}$is given where M is the total number of beads in NP and depends on NP size.

Repulsion parameters a_{ij}

	H	J	T	F	R	W	U	B	S	C	G
H	86.7	89.3	104	78	104	75.8	78	104	104	104	0
J		78	86.7	78	104	79.3	78	104	104	104	0
T			78	25	104	104	25	104	78*	104	0
F				78	78	78	78	78	78	104	0
R					78	78	78	78	78	104	0
W						78	78	78	104	104	0
U							78	78	78	104	0
B								78	78	104	0
S									78	78	0
C										78	0
G											0

Bond Parameters

Bond	NP-NP	NP-GT	H-H	J-T	T-T
$K^{(B)}$	100	17.75	4	4	4
r^e	0.8	0	0	0	0

2.2.2 Nanoparticle Model

The NP is formed from beads arranged into a 3D hexagonal simple lattice. The nearest neighbors are bonded together by harmonic bonds. Bond length is chosen to provide bead density of 3 beads/R_c^3. The NP is designed to represent an approximately spherical particle carved out of a crystal, which maintains its shape due to high bond rigidity. The inner layers of the NP are formed by core, 'C', beads that strongly repel all other beads in the system (except the outer layer of the NP) to ensure that the NP is impenetrable. The shell layers of the NP consist of hydrophobic 'S' beads, which effectively attract lipid tail beads (Figure 2.3).

NPs of three diameters are considered in order to probe three distinct situations: small NP of 2 nm in diameter (NP diameter approximately equals the thickness of the hydrophobic core of LB; total number of all beads in NP $M = 44$), a 4nm NP (NP diameter comparable with the LB thickness, $M = 355$), and an 8 nm NP (NP diameter double the LB thickness, $M = 2996$).

It is worth noting that a hydrophobic NP in a biological environment swiftly adsorbs various amphiphilic molecules including phospholipids. Therefore, an equilibrium monolayer of lipids is pre-adsorbed to the NP prior to the modeling of NP-LB interactions as observed in Figure 2.3.

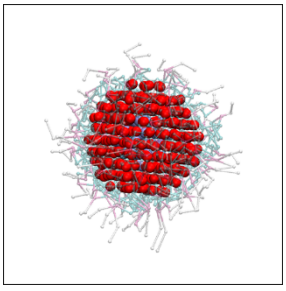

Figure 2.3 – 2 nm NP (red) with pre-adsorbed LM

For the purpose of creating a LM, a configuration is created where the NP is encapsulated in the hydrophobic core of the LB (as described in Section 2.3.1) and gradually removed. Eventually, the NP detaches with the LM adsorbed at its surface, and the chemical potential of the LM approximately equals that in the LB at the surface tension considered. Over ten trials, the average LM density is 1.8 lipids/nm^2, standard deviation of 3.7%.

2.2.3 System Setup

One of the main goals of this work is to explore the free energy landscapes of a hydrophobic NP interacting with a LB under isotension conditions. A surface tension of 10 mN/m is chosen for all force and free energy calculations for computational efficiency due to substantial fluctuations of the membrane at low tensions, as we do not stabilize the membrane by applying external potentials.[93] Although this tension exceeds the range of tensions of stable LBs in experiments, the simulated membranes are stable up to applied tensions of ~30 mN/m.[94] To create a system that allows for the NP-LB interactions to be probed without compromising the LB integrity, the system must be large enough that there are no periodic or edge effects, yet small enough that the simulation is relatively fast. For this purpose, two simulation setups are developed, as presented in Figure 2.4.

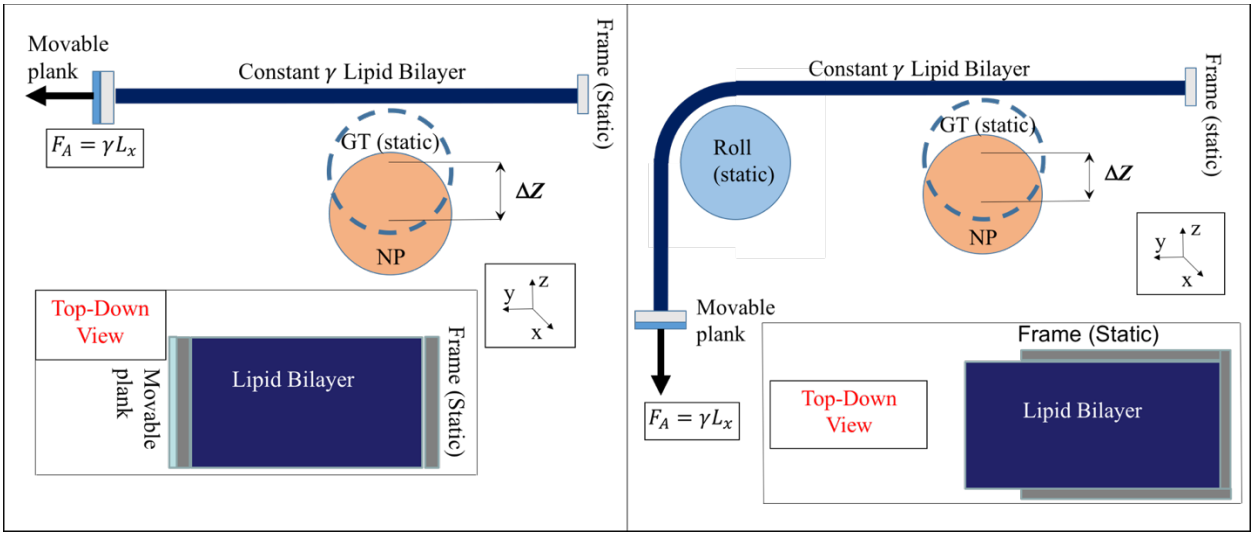

Figure 2.4 – Linear and rollover simulation setups to study the free energy landscape of NP-LB interaction under isotension conditions. The inserts show the top-down projections. The LB is placed on a *Π*-shaped static frame and stretched by a movable plank to which a constant force is applied to maintain given membrane tension.

A LB is placed in a Π-shaped frame that is formed from three horizontal planks: two along the *y*-axis and one along the *x*-axis. The planks are made of two layers of beads: inner layer of hydrophobic 'F' beads on the inside of the Π – frame, and outer layer of hydrophilic 'R' beads on the outside of the Π – frame. This construction allows the lipid bilayer to stick to the frame without wrapping around. On the open end, the LB is pulled either horizontally in the linear set-up (Figure 2.4, left) or in the rollover set-up (Figure 2.4, right) vertically down over a "roll" – a cylindrical block made of hydrophilic 'R' beads. The LB is stretched by a movable plank, to which a constant force is applied in order to maintain given LB tension by allowing the LB to advance/recede when it is deformed by the NP. The movable plank is constructed in the same manner as the static planks but rotated by 90 degrees - hydrophobic side facing up and hydrophilic side facing down. To each bead in the movable plank, a constant force F_p is applied to maintain membrane

surface tension, $\lambda = F_p M_p / L_x$ (Figure 2.4). Here M_p is the number of beads in the movable plank, and L_x is the length of that plank in the x-direction. While the linear setup is simpler, it requires larger y-dimension to prevent the movable plank from interacting with the static plank. It also requires larger x-dimension to prevent bending of the LB across the periodic image. The rollover setup allows for a smaller simulation box size since the LB is stretched downward in the z-direction. Most of the simulation were performed with the rollover setup.

The proposed setup, which imitates the standard experimental set-up for measuring the tension of thin films, is found practically efficient for maintaining isotension conditions and keeping the membrane location fixed in the process of translocation NP. hydrophobic NPs pre-coated by lipid monolayers. The existence of the lipid monolayer pre-adsorbed at the NP surface makes a principal difference as it prevents the membrane position stabilization using an external field (as done in ref. [95]), since the lipids adsorbed on NP mix with the membrane lipids, as the NP passes into LB, and are not distinguishable for the external field. NPs prior to intake and after release contain different lipid molecules in their coatings. This factor makes it nearly impossible to regulate the mutual arrangement of the NP and LB with a single external field, harmonic or otherwise, as it not clear to which beads the field should be applied. Another factor is that the membrane in our system experiences large expansion and contraction in the processes NP intake and release due to absorption and extraction of lipids coating NP. NPT simulations with semi-isotropic pressure coupling in the system with such large fluctuations of the membrane area could be extremely computationally expensive as one needs to reshape the entire box to extend/contract the membrane that brings about the convergence problem. The proposed

setup with the membrane placed on the immobile frame allows to avoid drastic changes in the box shape during the simulation in the NPT ensemble. The rollover setup is computationally more efficient in comparison with the horizontal setup, as it utilizes the vertical dimension to relax the film.

2.2.4 Computational Details

The simulations are performed in the simulation box of size 56x40x70 R_c (36x26x45 nm). The system has a density of 3 beads per unit volume (R_c^3), giving a total of 470,400 beads. The velocity Verlet leapfrog integration algorithm[96] is implemented, with a time step size of 0.01, a 1,000,000-step initial equilibration run, then eight parallel 400,000-step data runs on 16 cores in an NVT ensemble. Calculations presented in the main text are performed with LAMMPS[97] run on the Extreme Science and Engineering Discovery Environment (XSEDE)[98]. Additional simulations with DL_Meso[99] and an in-house DPD package are run. The results between the different software packages are comparable and are discussed in section III.

2.2.5 Force and Free Energy Calculations using the Ghost Tweezer Technique

To calculate force and free energy landscapes, we use the GT method developed in our earlier work.[100] The GT is implemented by introducing a "twin" GT particle, that is identical in the bead configuration to the real NP. The "ghost" NP beads are kept in undisturbed hexagonal order and do not interact with any system beads except for the NP beads. Harmonic spring potentials are applied between each respective pair of real NP and GT beads (i=1,...,M). Each GT bead interacts with no other bead but the corresponding NP

bead through a harmonic bond, effectively tethering the real NP to a point in space. Thus, the NP is attached to a certain position by the GT force between the NP and its ghost image:

$\mathbf{F}_{\mathrm{GT}} = \sum_{i=0}^{M} k_{\mathrm{GT}}^{(B)}\left(\mathbf{R}_{NP,i} - \mathbf{R}_{\mathrm{GT},i}\right)$ (2.1) where $\mathbf{R}_{NP,i}$ and $\mathbf{R}_{\mathrm{GT},i}$ represent the coordinate of bead 'i' within the NP and the GT respectively, and $k_{\mathrm{GT}}^{(B)}$ is the spring constant of the harmonic potential between the respective NP and GT beads. Because the average lateral contribution to $\mathbf{F}_{\mathrm{GT}}$ due to the system symmetry is zero and the structures of the NP and its ghost image are the same, the average force on the NP from the GT is equal to

$F_{\mathrm{GT}} = K_{\mathrm{GT}}^{(B)}(\bar{Z} - Z_{\mathrm{GT}})$, (2.1b)where $\bar{Z}$ is the average normal coordinate of the NP center of mass, Z_{GT} is the normal coordinate of the center of mass of the immobile GT particle, and $K_{\mathrm{GT}}^{(\mathrm{B})} = Mk_{\mathrm{GT}}^{(\mathrm{B})}$ is the overall GT spring constant acting between the real and ghost NPs. $K_{\mathrm{GT}}^{(\mathrm{B})}$ is chosen to optimize the efficiency of calculations. The overall spring constant between the real and ghost particle, $K_{\mathrm{GT}}^{(\mathrm{B})}$ =176 kT/R_{c}^2 (1.7 N/m), is used independent of the NP size, whereas the individual spring constant varies. An image illustrating the GT method is presented in Figure 3. This GT setup with multiple spring bonds between the NP and GT beads prevents NP rotation and reduces fluctuations of the NP position and, the calculated GT force, respectively as presented in Figure 2.5.

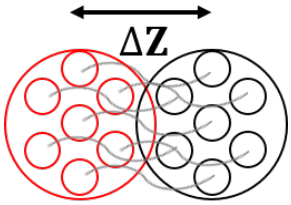

Figure 2.5 – Diagram of the GT implementation. The twin GT particle (black), formed of the beads arranged in the same manner as the beads in the real NP, is placed at given position Z_{GT} in space. The real NP (red) is attached to the GT by the springs connecting respective NP and GT beads. The average separation, $\Delta Z = \bar{Z} - Z_{\mathrm{GT}}$, between the two is measured allowing for the force needed to keep NP at given distance $\bar{Z}$ from the membrane to be calculated through (b).

At the initial state, the GT is placed in a certain position sufficiently far from the membrane, the system is equilibrated with the NP fluctuating around the GT with zero mean displacement and, respectively, zero mean force. After the system equilibration, the GT is placed in a new position on the z-axis (the x and y coordinates are constant), and a new simulation is run, probing the force at the new location. This process is continued in incremental steps and the force experienced by NP from LB is measured in a quasi-equilibrium fashion along the translocation trajectory until a spontaneous transition takes place (e.g. NP intake by LB). This method ensures that no force or energy minima are missed although it does not allow calculation of the free energy change during spontaneous transformations. It is important to note that this is not a towing process, but rather a sequential, quasi-static, quasi-equilibrium, incremental process that was confirmed by checking the reproducibility of the results and scanning the trajectory backwards. Exceptions are the points of spontaneous transitions of the NP insertion into LB in the process of intake and NP detachment from LB in the process of release. While at these points the GT position is kept fixed, the NP experiences a finite displacement across the LB boundary "jumping" from one valley of the energy landscape to another. These

spontaneous irreversible transitions make impossible to make the transfer of NP across LB along a continuous trajectory that prevents the use of standard methods of free energy calculations like umbrella sampling. The GT method enables the construction of the two energy landscapes, outside and inside the LB, which resemble two valleys separated by the ridge that is impassible in incremental steps: a mountaineer ascending the ridge from one valley can find a pass and climb up to the crest of the ridge and then jump down. This is illustrated in Figure 2.6. The advantages of the GT method compared to umbrella sampling are the simplicity and relevance to experimental optical tweezers method.

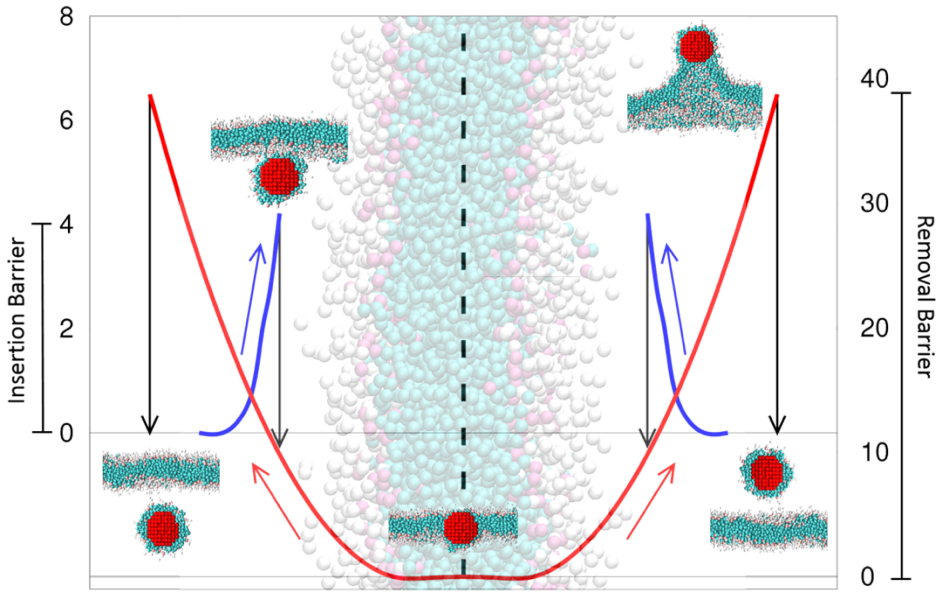

Figure 2.6 – An example energy landscape for the 4 nm NP. The NP begins with a coated monolayer on the outside of the LB. As the NP approaches the LB, the energy barrier increases following the blue line. At some point when the LM contacts the LB, they merge, and the NP enters the bilayer. The NP finds an energy minimum at the center of the LB. The barrier increases following the red line until a NP coated LM spontaneously breaks from the LB and the system returns to its initial state. The left y-axis represents the energy barrier of insertion corresponding to the blue line, whereas the right y-axis represents the energy barrier of removal corresponding to the red line. The semi-transparent LB represents the real LB thickness and helps visualize why the barriers are increasing as they are.

From the force the GT exerts on the NP, $F_{GT}(Z)$, the Helmholtz free energy, $E_{NP}(Z)$, can be obtained by thermodynamic integration and calculation of the mechanical work needed to bring the NP from the initial state at position Z_0 to given position Z in the vicinity of the membrane. There are two characteristic initial states where the NP equilibrium is achieved without applying an external force: free state in the solvent bulk, $Z_0 = Z_b$, far from the membrane and encapsulated state at the center of LP, $Z_0 = 0$. These initial states are used to monitor the NP intake and release, respectively. In our simulation set-up, the process of NP-LB adhesion and translocation is associated with the deformation of the membrane and redistribution of lipids and respective displacement of the movable plank. The plank displacement causes the work done against the constant force F_p applied to the plank to maintain given membrane tension. To measure this work, the average position $\bar{L}(Z)$ of the mobile plank is determined during the NP equilibration at the position Z. $\bar{L}(Z)$ determines the membrane extension between the static and mobile planks. The work done by the GT equals the change of the Helmholtz free energy of NP-LB, $\Delta E(Z)$, plus the mechanical work performed against the plank force:

$$\Delta E(Z) = \int_{Z_0}^{Z} F_{GT}(Z)dZ - \gamma L_x[\bar{L}(Z) - \bar{L}(Z_0)] \quad (2.2)$$

where $[\bar{L}(Z) - \bar{L}(Z_0)] = \Delta L)$ is the displacement of the plank corresponding to either contraction or extension of the membrane. Note that $\gamma L_x \Delta L$ represents the work needed to extend/contact the membrane area by $L_x \Delta L$. In the process of intake, the membrane first bends and the plank displacement ΔL is negative, however, upon incorporation of the NP and absorption of lipids in the NP coating, the membrane extends causing the positive plank displacement. The maximum membrane extension is achieved at the equilibrium position with the NP fully encapsulated at the LB center at $Z_o = 0$. In the course of NP

release from the fully encapsulated state at $Z_0 = 0$, the membrane bends and $\bar{L}(Z)$ progressively decreases up to the point of spontaneous rupture of the NP-LB junction and NP detachment from the membrane.

2.3 Results and Discussion

2.3.1 Free energy landscape of hydrophobic NPs in the vicinity of LB

2.3.1.1 1 nm nanoparticle

Figure 2.7 shows the force experienced by the NP as a function of NP position and the free energy landscape for a 1 nm NP near a DMPC LB

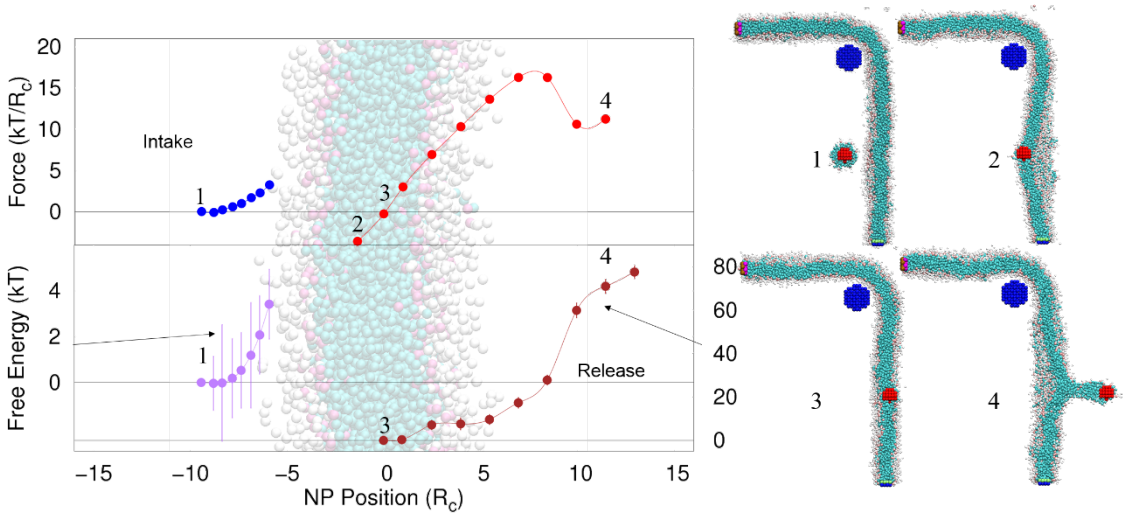

Figure 2.7 – The position dependence of the GT force counterbalancing the NP-LB interaction force (top) and the free energy landscape (bottom) for the 1 nm NP. The LB snapshot in the graph background is scaled to the characteristic bilayer thickness. The left portion represents intake barriers, and right release. Note the different free energy scales for intake and release. Blue (purple) and red (brown) circles show, respectively, the force (free energy) in the course of intake and release. Z coordinate represent the center of mass position of the NP. The panels on the right are the snapshots of characteristic configurations. (1) – initial position of NP in bulk solvent; (2) – immediately after NP intake; (3) – equilibrium state with the NP in the center of LB, initial position for the release process; (4) – NP-LB junction formation at the onset of the spontaneous detachment of the NP.

At the initial reference state, the NP pre-coated with LM is placed far from the LB in the solvent bulk and does not feel the presence of the LB: $F_{GT} = 0$ (Figure 2.7 snapshot 1). As the NP approaches the LB, it experiences repulsion due to the disjoining pressure in the water film squeezed between the NP coated by LM and the outer leaflet of LB. This repulsion force is counter balanced by a positive GT force. As the NP advances towards the LB, the GT force increases up to a maximum value of 3.2 kT/R_c (2.04×10^{-11} N), which is weaker than a characteristic force between neighboring DPD beads. The respective free energy landscape is calculated with (2.2). The LB bending on NP approach causes a free energy increase with a maximum of 3.4 kT, a relatively low barrier meaning the intake would occur rapidly in a biological system. Upon achieving the free energy maximum, the system experiences a spontaneous transformation: the LM adsorbed on the NP surface merges with the LB, resulting in the NP intake by the LB hydrophobic core. The membrane extends due to the pulling force applied to the mobile plank (the work made against the pulling force on the system accounted for in (2.2)). The statistical error in the energy barrier calculations is high, due to the small magnitude of the barrier and large fluctuation of the plank position (the graphs of the plank position $L(Z)$ and the free energy error calculations are discussed in section 2.3.3).

It is worth noting that during the spontaneous interfacial transfer, the position of NP with respect to the LB center plane changes on the order of NP diameter upon incremental displacement of the GT that cause discontinuity of the GT force. Immediately after the intake (position 2 in Figure 2.7), the GT force acting on the NP is negative in order to retain NP from moving further into the equilibrium state in the LB center (Z=0). The equilibrium corresponds to a free energy minimum with zero effective force acting on the

NP. It is taken as the initial reference point for monitoring the process of NP release. For the encapsulated configurations, the effective force on the NP increases linearly as the NP departs from the equilibrium position up to $Z < 4.5$ nm due to the elasticity of the LB. Due the spontaneous nature of the NP encapsulation, the free energy profile for NP motion is asymmetric: the state with an encapsulated NP has a different free energy than the state with a free NP located and the same coordinate. As the NP moves further, the LB configuration changes, and a cylindrical junction forms between the NP and the LB. The LB relaxes, moving closer to the frame plane (Figure 2.7 and Figure 2.8). The GT force magnitude decreases. The junction formation causes the number of lipid molecules inside the LB to decrease, therefore the movable plank recedes which brings about a negative contribution to the free energy. As a result, the free energy landscape shows a plateau (Figure 2.7, bottom panel). This behavior is reliably observed for small NPs, even with different parameters. The dynamics of junction formation is illustrated with the characteristic snapshots in Figure 2.8. During the first three frames, the system evolves with time with the GT kept in the same position. The LB pulls away from the NP and creates a cylindrical junction connecting the LM to the LB. In the fourth frame, the GT is moved once again causing the junction to rupture.

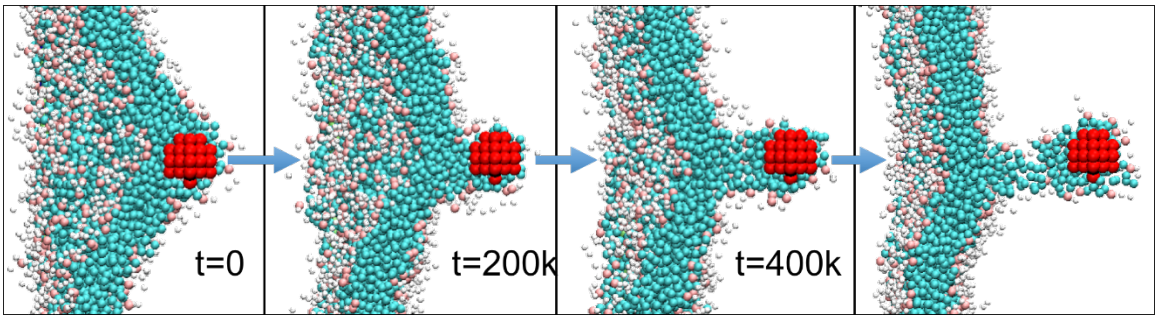

Figure 2.8 - Dynamics of the formation and breakup of the NP-LB junction. The left most image is taken immediately after the GT is incrementally displaced outwards the frame plane, the second image (after 200,000 timesteps) is taken as the junction begins to

form, and the third image (after 400,000 timesteps) shows the equilibrated state with a well-developed junction. As the junction forms, the LB curvature decreases causing the free energy to increase dramatically and the force to decrease as observed in Figure 2.7, point 4. In the fourth image, the GT is positioned farther away from the frame plane, and the junction begins to rupture causing spontaneous detachment of the NP.

Scanning simulations are performed, varying back and forward the GT position around the point of junction formation. No hysteresis on $F(Z)$ dependence is found confirming that the junction formation is reversible. The forces observed on the NP approach to the frame plane reasonably equal those on reproach, which indicates an absence of a spontaneous transition associated with the junction formation. As the NP moves farther from the plane frame, the junction neck spontaneously ruptures, and the NP separates from the LB. The release process is now complete. The necessity to proceed through the junction configurations creates a high potential barrier (75.1 kT) that the 1 nm NP must overcome in order to escape the LB core.

2.3.1.2 2 nm nanoparticle

The process is qualitatively similar to what is observed for the 2 nm NP. As the NP moves towards the LB from solvent bulk (Figure 2.9, snapshot 1, $F_{GT} = 0$) it experiences repulsion due to LB deformation. The force reaches a maximum of 3.1 kT/R_c (0.47×10^{-10} N), and free energy a maximum of 4.2 kT. As the GT advances further, a spontaneous intake of the NP by the LB (Figure 2.9, snapshot 3) is observed, with a step-like drop in the force magnitude. NP intake and its incorporation into the LB hydrophobic core is preceded by water displacement from the NP-LM gap and fusion of the LM with the outer leaflet of LB (Figure 2.10). The LB spontaneously relaxes and the mobile bar advances.

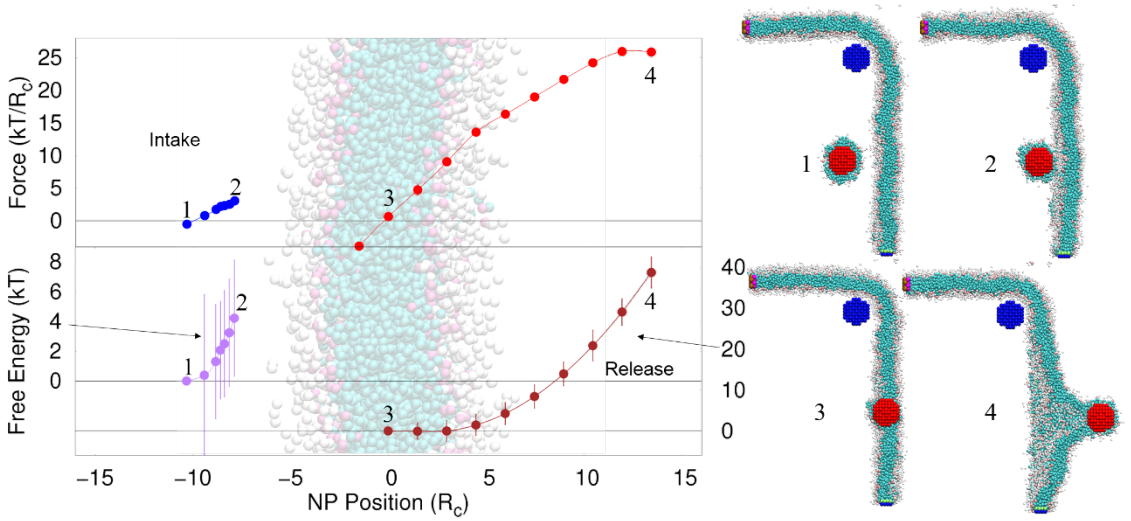

Figure 2.9 – The position dependence of the GT force counterbalancing the NP-LB interaction force (top) and the free energy landscape (bottom) for the 2 nm NP. The LB snapshot in the graph background is scaled to the characteristic bilayer thickness. The left portion represents intake barriers, and right release. Note the different free energy scales for intake and release. Blue (purple) and red (brown) circles show, respectively, the force (free energy) in the course of intake and release. Z coordinate represent the center of mass position of the NP. The panels on the right are the snapshots of characteristic configurations. (1) – initial position of NP in bulk solvent; (2) – LB bends as NP approaches LB just before NP intake; (3) – equilibrium state with the NP in the center of LB, initial position for the release process; (4) – maximum stretching of LB before the NP breaks free of the LB. Note the lack of pronounced junction compared to the 1 nm NP in **Error! Reference source not found.**

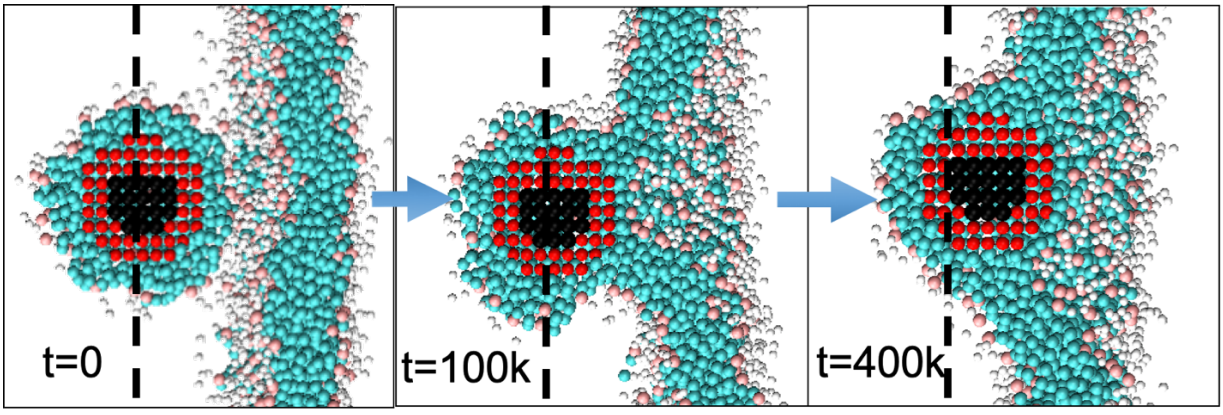

Figure 2.10 – Dynamics of the LM fusion with the LB for the 2 nm NP. The left most image represents the point immediately after the GT is moved. The second image (after 100,000 timesteps) is taken as water is displaced from the NP-LB gap and the LM begins to merge with the outer leaflet of the membrane. Finally, in the third image, the system is equilibrated, and the NP is completely encapsulated within the LB. The black line represents the location of the GT, and black beads represent NP core beads. The GT is in

the same position relative to the frame plane in all snapshots. The same process occurs for the 2 nm NP.

The process of release is also similar to that for 1 nm NP: as the encapsulated particle moves from the equilibrium position at the frame plane, the LB stretches (**Error! Reference source not found.**, snapshot 4) and the NP experiences a positive force increasing approximately linearly with Z. (**Error! Reference source not found.** top panel) An important distinction from the 1 nm NP is an absence of the cylindrical junction between the NP and LB. The LB does not recede back to the frame, and the GT force levels out rather than decreases. As the GT moves farther, the lipid junction ruptures, the NP coated by LM separates from the LB and the LB returns to its equilibrium position within the frame plane. The maximum effective force experienced by the NP on the onset of spontaneous detachment is 25.0 kT/R_c (1.7×10^{-10} N), and the free energy barrier is 37.2 kT (**Error! Reference source not found.**, snapshot 4).

2.3.1.3 4 nm NP

The translocation of the largest NP (4 nm in diameter) considered in this chapter follows similar stages as the translocation of smaller NPs, the energy barriers are higher. The intake transition takes place much later compared to 1 nm and 2 nm NP. It requires a substantial deformation of the LB (Figure 2.11, snapshot 2) and therefore is associated with a substantial repulsion force (about 34 kT/R_c or 2.2×10^{-10} N, see Figure 2.11, top left) and free energy barrier of about 40 kT (Figure 2.11, bottom left). Following the intake, the qualitative snapshot is like that of smaller NPs – the NP sits in the center of the LB relaxed within the frame plane.

The barrier is much higher than those observed with smaller NPs. However, it is not high enough to effectively prohibit the intake transitions in natural environment. The reason for the difference between 4 nm and smaller particles is the increase of the stability of the LM adsorbed on the particle surface in its size. The 1 nm NP is about the effective length of the hydrophobic tail of the DMPC molecule. The NP surrounded by DMPC molecules is essentially a spherical micelle, and a micelle is generally less stable than an LB, has lower barrier for merging with the latter. An LM adsorbed on an 4 nm NP is denser and, most importantly, more uniform. It therefore reasonable that the barrier associated with LM and LB fusion increases with the NP size, and this dependence is most pronounced when the latter is comparable with the LB thickness or slightly exceeds it.

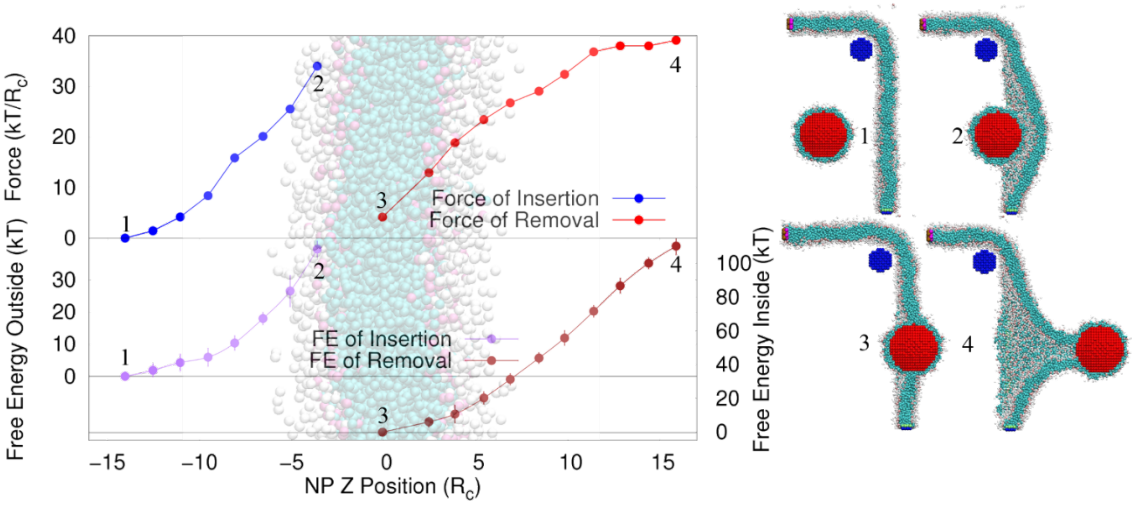

Figure 2.11 - The position dependence of the GT force counterbalancing the NP-LB interaction force (top) and the free energy landscape (bottom) for the 4 nm NP. The LB snapshot in the graph background is scaled to the characteristic bilayer thickness. The left portion represents intake barriers, and right release. Note the different free energy scales for intake and release. Blue (purple) and red (brown) circles show, respectively, the force (free energy) in the course of intake and release. Z coordinate represent the position of the NP center of mass. The panels on the right are the snapshots of characteristic configurations. (1) – initial position of NP in bulk solvent; (2) position just prior the spontaneous intake; - LB bends as NP approaches; (3) – equilibrium state with the NP in the center of LB, the initial position for the release process; (4) – position just prior the

spontaneous detachment with maximum stretching of the LB before the junction break-up.

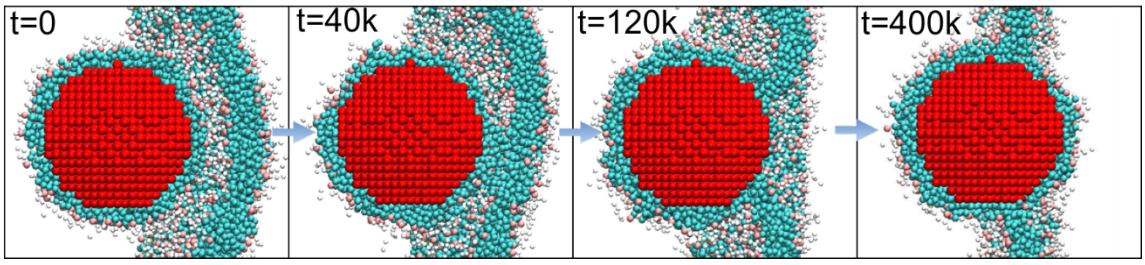

Figure 2.12 – Dynamics of the LM fusion with the LB for the 4 nm NP. The left most image represents the initial position of the simulation run immediately after the GT is incrementally moved toward the membrane; NP coated with LM is separated from the membrane by a water layer. The second image (after 40,000 timesteps) is taken at the onset of water expulsion and fusion of LM with the outer leaflet of LB. In the third image (after 120,000 timesteps), the LM is progressively absorbed and the membrane, in order to accommodate additional lipids, begins to stretch around the NP. In the last image (after 400,000 timesteps), the system has reached equilibrium with fully encapsulated NP. The GT remains at the same position relative to the frame plane during the simulation run.

The mechanism of NP release is illustrated in Figure 2.13. During the process of release, outward displacement of the encapsulated NP deforms the membrane, which bends creating elastic resistance. As the NP moves further, a similar phenomenon to the smaller NPs' release is observed: a junction forms between the NP and the LB (Figure 2.13, images a-c). The shape of the junction resembles a tubular micelle with water inside the bilayer neck, rather than a thin rope-like bridge with a single hydrophobic core observed for 1 and 2 nm NPs. As the LB stretches, the water is squeezed out and a cylindrical junction forms (Figure 2.13, images d-e). This junction forms a neck, which at a certain point (Figure 2.13, image f) ruptures. During the junction extension, the GT force becomes nearly independent on the NP position, while the free energy increases in excess of 110 kT before the junction snaps and the NP covered by LM escapes the LB. The barrier of such height practically prohibits unforced translocations via this mechanism.

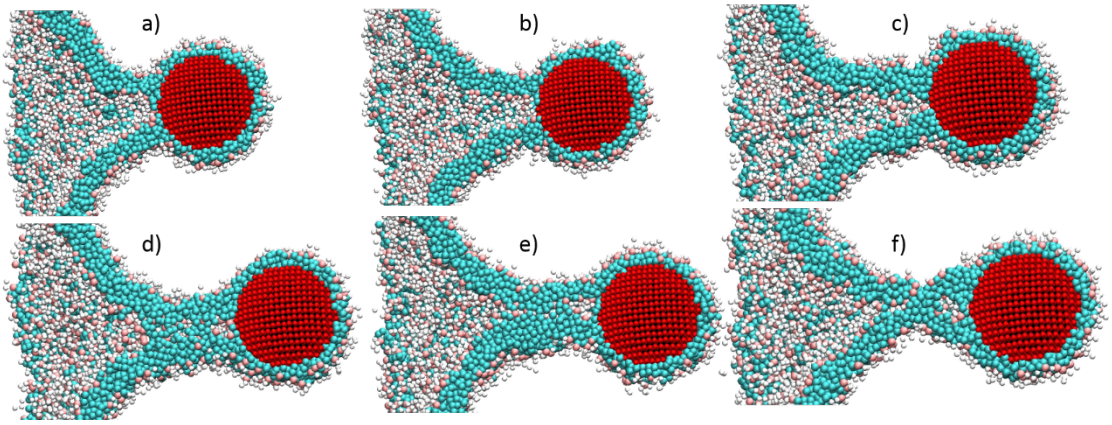

Figure 2.13 – Dynamics of release for the 4 nm NP. Snapshots correspond to a set of consequent GT positions. Beginning in the top left, the LB experiences extreme bending caused by the LM-coated NP. As the force increases (the GT is moved further from the frame plane) water filled tube-like junction forms (images a-c). Further along, the water is squeezed out, a cylindrical junction forms, and the LB recedes (images d-e). Junction formation is similar to 2 and 4 nm NPs, but with much stronger bending of the LB. Finally, the junction ruptures and the NP is detached from the LB. The final snapshot is a non-equilibrated configuration just at the onset of junction break-up.

2.3.2 Comparison of Different Software Packages and Interaction Parameters

As mentioned previously, the simulations were run with different interaction parameters between the NP and lipid tails and in different software packages. Presented in Figure 2.14 are the force and free energy landscapes for the 2 nm NP using different software packages and interaction parameters.

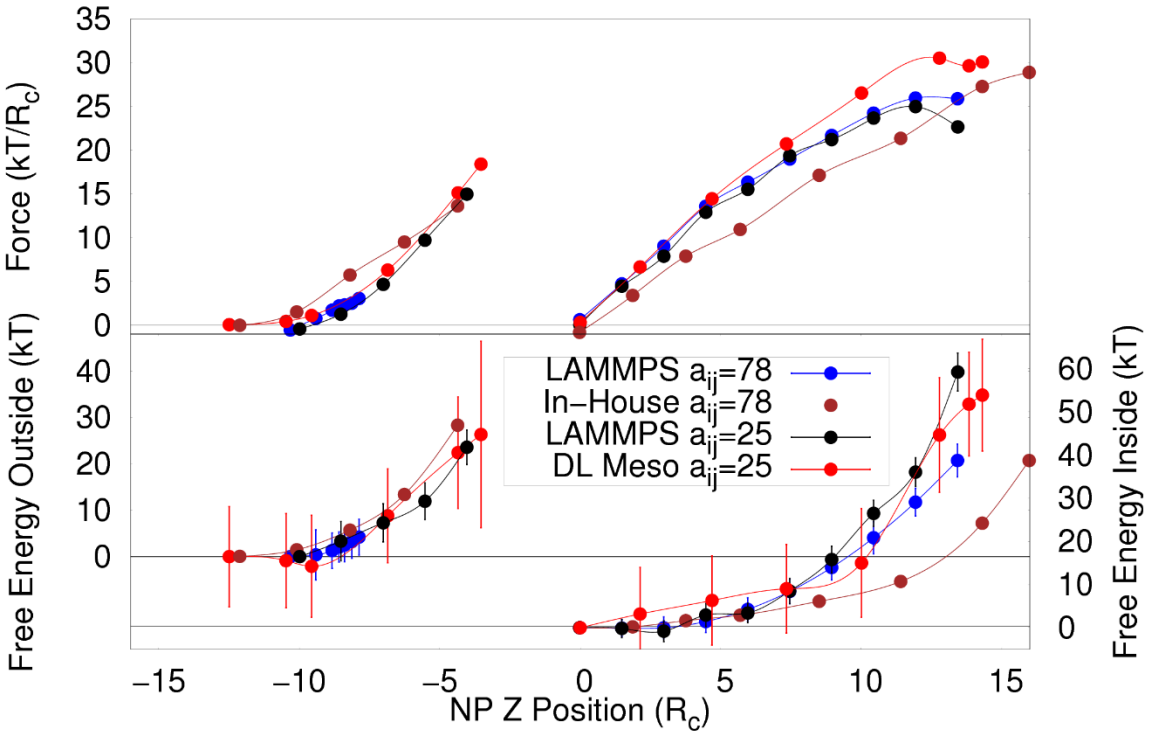

Figure 2.14 – Different systems force and free energy landscapes for the 2 nm NP. In blue is LAMMPS with $a_{TS} = 78\ kT/R_c$ (T-beads denote the lipid tail, and S-beads are surface beads of the NPs), given in black are LAMMPS results with $a_{TS} = 25\ kT/R_c$, red DL_Meso with $a_{TS} = 25\ kT/R_c$, and brown in-house with $a_{TS} = 78 kT/R_c$

The results for NP intake agree within the statistical error except for the maximum force and free energy values for LAMMPS for $a_{TS} = 78$. It is clear from the simulation images that the difference is a result of the easier merge between the LM and the LB. The LM surrounding the NP easily merges with the LB as discussed in the main text. As a result, the NP is encapsulated much sooner. For the other simulations, the LB experiences much more significant bending before NP intake. To be clear, all of the simulations follow a similar trend, but NP intake occurs much earlier for the system discussed in the main text. Calculations with DL_Meso had larger fluctuations in the bar and, as a result, more error in the free energy calculations. The two systems with $a = 25$ agree within error. The results for NP release all agree within error except those done with in-house calculations.

In-house calculations were done with a linear setup (no Π-shaped frame) and due to size restrictions, the LB bent at the edges which allowed the NP to move further from the frame center.

Presented in Figure 2.15 are the force and free energy landscapes for the 1 nm NP using different software packages and interaction parameters.

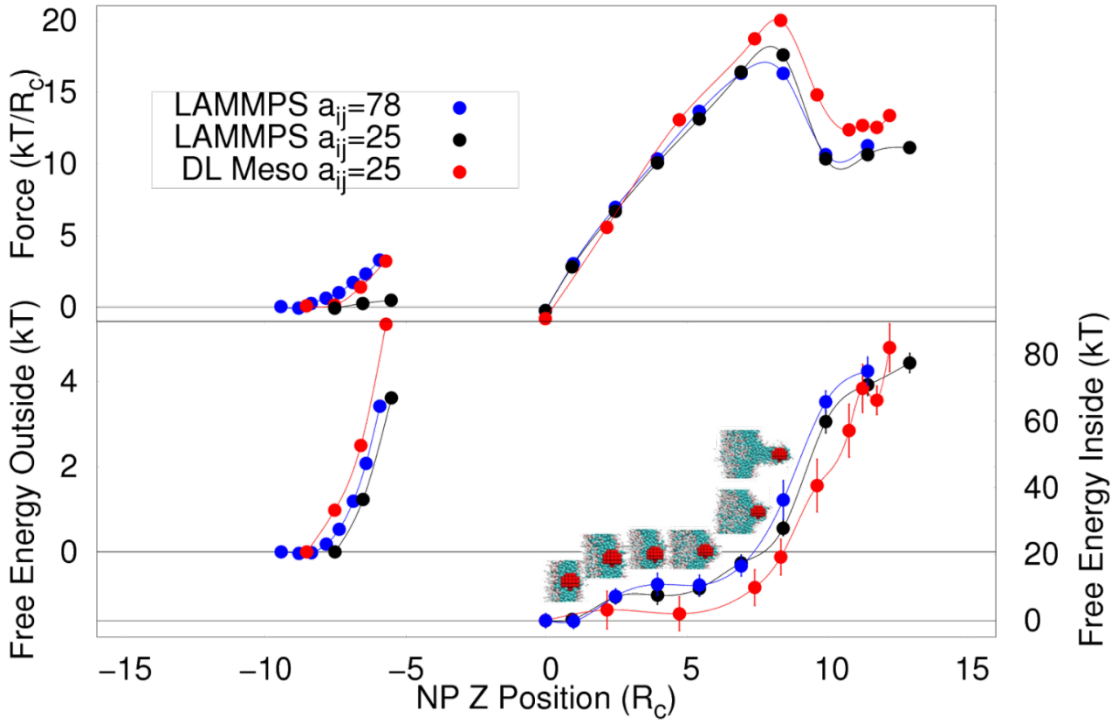

Figure 2.15 – Different systems force and free energy landscapes for the 1 nm NP. In blue is LAMMPS with a_{rs}= 78kT/R_c between the lipid tail and NP shell, black - LAMMPS with a_{rs}= 25 kT/R_c, and red - DL_Meso with a_{rs}= 25 kT/R_c. The snapshots illustrate the process of junction formation. Error not included for insertion for clarity because error bars for DL Meso are an almost order of magnitude larger than the NP intake value.

The difference between the 3 systems is within error of the calculations. Simulations with DL Meso showed larger fluctuations of the mobile plank position, which contributes to the error in the energy barrier. In the release stage, the dependence of the free energy on the NP position "levels out" just before a junction between the NP and the LB starts to form and the LB starts receding to the frame plane. That effect is observed in all three

simulations. The first snapshot in Figure 2.15 shows the first step of NP release stage (second data point) where the NP sits at an energy minimum in the hydrophobic core of the bilayer. As the NP moves further from the frame plane, the lipids restructure around the NP and the LB begins to bend slightly, but the environment around the NP does not appear to change. The NP then forms a cylindrical junction between the LB and LM. As the junction forms, a sharp, but continuous drop in force is observed. Yet, the free energy increases because the LB recedes back to the frame plane allowing the bar to extend.

We also attempted to perform translocation simulations for an 4 nm NP, which is about twice as large as the LB thickness. The NP follows the same trend to the other NPs: the barrier associated with NP encapsulation steeply increases with the NP diameter. However, we did not manage to achieve NP intake. The NP crossed the frame plane without the intake by the hydrophobic core of the membrane (Figure 2.16) and the repulsive force continued to increase until we could no longer maintain the integrity of our setup. That is, the mobile pulling plank moved passed the roll and the LB was ripped from the frame. The GT force at the breaking point reached 60 kT/R_c (3.8×10^{-10} N). Such a high barrier makes encapsulation an extremely rare event. We suggest that encapsulation of such particles should happen via a different mechanism, such as engulfment of NP by the LB with a gap between the LB and adsorbed lipid monolayer. Simulations of this mechanism requires different models and system sizes and is out of the scope of this study.

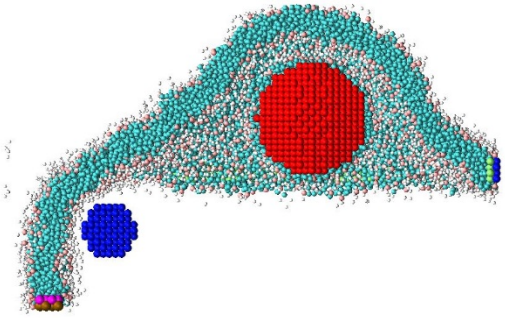

Figure 2.16 – Last state for 4 nm particle before loss of system integrity. The half of the LB is removed in the visualization so the intact monolayer surrounding the NP and extreme LB bending can be observed

It is clear that with such a strong attraction between LM and the NP surface caused by a very low a_{ns} in conjunction with a large NP size makes the LM very stable and uniform. Therefore, fusion of LM with the LB outer leaflet is associated with a very high barrier. The effect is not as pronounced if the NP is smaller: a natural shape of lipid layers is flat. In case of a spherical micelle with small nanoparticle inside (say, 1 nm hydrophobic NP), the surface density of heads is insufficient for covering the entire surface. The hydrophobic core of the monolayer becomes easier exposed to the hydrophobic beads of the LB, causing LM-LB fusion and NP intake.

2.3.3 Error Calculations and Individual Contributions of the Work

Referring to (2.2), The integral $\int_{Z_0}^{Z_1} F_{\mathrm{GT}}(Z_{NP})dZ$, is carried out using Simpon's rule, the error of which is calculated in the standard manner. The error of each force and position measurement is calculated as $\left(\sigma/\sqrt{N}\right)$. As is displayed in Figure 2.17, the error in this term is relatively small. The second term, $\gamma L_x[\bar{L}(Z_1) - \bar{L}(Z_0)]$ is calculated by taking $\gamma L_x\sqrt{\left(\sigma_n/\sqrt{N}\right)^2 + \left(\sigma_0/\sqrt{N}\right)^2)}$, where N is the number of trials per measurement, σ_n and

σ_0 are the standard deviations of the n[th] and reference bar position measurements respectively. While the error in bar position is O~10[-1] R$_c$, the prefactor, γL_x, causes the error O~10[0], resulting in the visually large error bars when free energy is small in Figure 2.17.

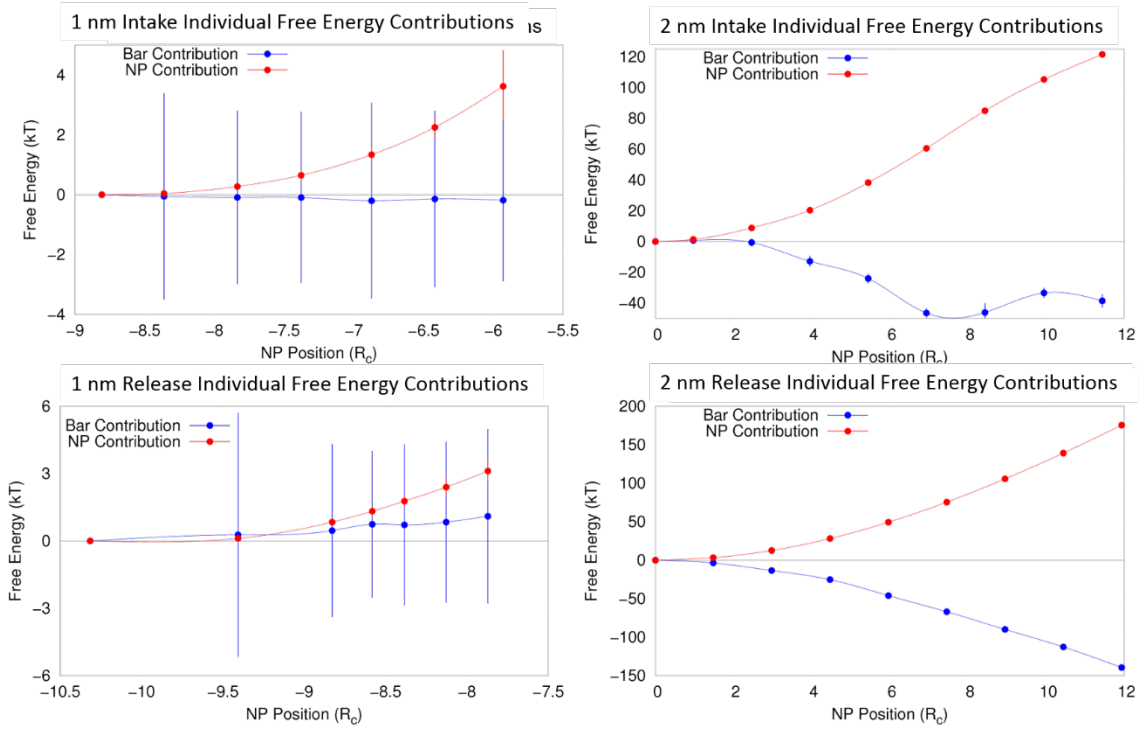

Figure 2.17 – Contributions to the free energy from the work performed by the GT force and the mobile plank for the intake and escape stages of 1 nm and 2 nm NPs.

All points (excluding the initial position) in Figure 2.17 are shown with error bars. Wherever the error bars are not shown they are smaller than the symbol size. For the intake stage, it is clear the contribution from the mobile pulling plank (second term in (2.2)) has little effect on the overall free energy. On the intake stage with both the 1 nm and 2 nm nanoparticles, the plank contribution is below 1 kT. The small positive contribution from the plank for the 2 nm intake is likely due to lipid exchange between

the LM and LB which slightly increases the length of the LB. However, the contribution from the plank to the free energy on the release stage is quite large, about 50 *kT* and 140 *kT* for the 1 nm and 2 nm respectively. An interesting non-monotonic contribution from the bar is observed for the 1 nm release. This is a result of the junction formation, which is explained in the previous section and in Figure 2.15.

2.3.4 Dynamics of unforced NP transport through LBs

2.3.4.1 The Fokker-Planck Equation

GT simulations show that both NP intake and release processes are associated with particular energy barriers. In the absence of external forces, these barriers should be overcome due to thermal fluctuations that cause NP Brownian diffusion that is possible within realistic experimental timescales only in case of reasonably low barriers. To evaluate the timescale needed for NP intake and release from the LB we employ the Fokker Planck (FP) equation, which describes particle motion as a random walk along a free energy landscape. The FP approach has been used extensively in a wide range of applications, from translocation dynamics,[101, 102] nucleation,[103] and of particular interest to this study, probabilistic tracking of particle locations whose positions evolve according to Langevin dynamics.[104-106]

The Fokker-Planck Equation can be derived as shown below. To simplify the explanation, we assume a single particle in a one-dimensional phase space. In each time step, $\tau + \Delta\tau$, the particle has probability to make one of three moves – it can move forward, backward, or stay in the same location. This is represented by k^+, k^-, or k^0 respectively. The probability of all three moves summed is 1. Additionally, we can

multiple both sides of the equations by $W(Z,\tau)$, the particle probability distribution function, to be used later.

$$k^+ + k^0 + k^- = 1;\ \ W(Z,\tau)[k^+ + k^0 + k^-] = W(Z,\tau) \quad (2.3)$$

Next, we obtain a function for $W(Z,\tau+\Delta\tau)$, by conducting a probability balance (Figure 2.18)

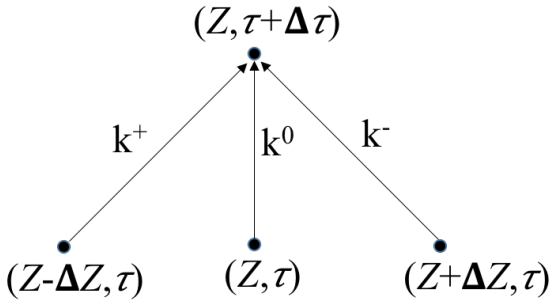

Figure 2.18 – Probability balance for the particle. Beginning at time τ, this gives the three possible routes to end up at position Z at time $\tau+\Delta\tau$.

From the probability balance in Figure 2.18, we obtain

$$W(Z,\tau+\Delta\tau) = [W(Z-\Delta Z,\tau)k^+ + W(Z,\tau)k^0 + W(Z+\Delta Z,\tau)k^-]\Delta\tau \quad (2.4)$$

Subtracting (2.3) from (2.4), gives (2.5)

$$W(Z,\tau+\Delta\tau) - W(Z,\tau)/\Delta\tau = W(Z-\Delta Z,\tau)k^+$$

$$-W(Z,\tau)[k^- + k^+] + W(Z+\Delta Z,\tau)k^- \quad (2.5)$$

Finally taking the continuum limit and setting $(k^+ + k^-)/2 = B(Z)$ and $k^+ - k^- = A(Z)$, we obtain

$$\frac{\partial W(Z,t)}{\partial t} = \frac{\partial}{\partial Z}\left[A(Z)\,W(Z,t) + B(Z)\frac{\partial W(Z,t)}{\partial Z}\right] \quad (2.6)$$

While (2.6) gives a general FP equation, this can be derived in a more specific manner. It can be shown that $B(Z)$ represents diffusion and $A(Z)$ velocity. If we assume diffusion does not depend on position, we obtain

$$\frac{\partial W(Z,t)}{\partial t} = \frac{\partial}{\partial Z}\left[-\frac{f(Z)}{\zeta}\, W(Z,t) + D\frac{\partial W(Z,t)}{\partial Z}\right] \tag{2.7}$$

where $f(Z)$ is the external force acting on a particle, ζ is the friction coefficient of a particle, and D is the effective diffusion coefficient of the particle in solvent. The effective diffusion coefficient, D, in the FP equation characterizes NP mobility and hydrodynamic resistance to its motion. In a bulk solvent, it can be estimated through the Stokes-Einstein (SE) relationship, as $D = kT/6\pi\eta R_{\mathrm{P}}$, where η is the viscosity of water and R_{P} is the hydrodynamic radius of a LM-coated NP (R_{P} equals the NP radius augmented by the effective thickness of the LM covering the NP). For NPs of 2, 4, and 8 nm, the SE relationship gives $D = 2.45 * 10^{-10}, 1.23 * 10^{-10}, \text{and } 6.13 * 10^{-11}\ \mathrm{m}^2/\mathrm{s}$, respectively. The effective diffusivity of the NP interacting with the LB is difficult to estimate. Moreover, a NP's mobility outside (for intake processes) and inside (for release processes) may differ. For example, the release of an encapsulated NP involves LB bending which increases hydrodynamic resistance to the NP translocation. It may be agreed that the SE equation gives the upper estimate for D. For the FP model numerical calculations, the free energy landscapes determined in the simulation by the GT method are approximated with 4th ordered polynomials. Exact equations are presented in Figure 2.18. Noting that $\zeta = k_B T/D$, $f(Z)/k_{\mathrm{B}}T = -\left({}^{\partial E(Z)}/_{\partial Z}\right)_{V,T}$ where $E(Z)$ represents unit-less free energy, and $\tau = tD/L^2$, then substituting back into (2.7), we obtain

$$\frac{\partial W(Z,\tau)}{\partial \tau} = \frac{\partial}{\partial Z}\left[\frac{\partial E(Z)}{\partial Z}\, W(Z,\tau) + \frac{\partial W(Z,\tau)}{\partial Z}\right] \tag{2.8}$$

As a model, the energy barriers for all systems are approximated with a 4th-ordered polynomial, $(E(Z) = AZ^4 + BZ^3 + \cdots CZ + D)$. The plots of which are provided in Figure 2.19.

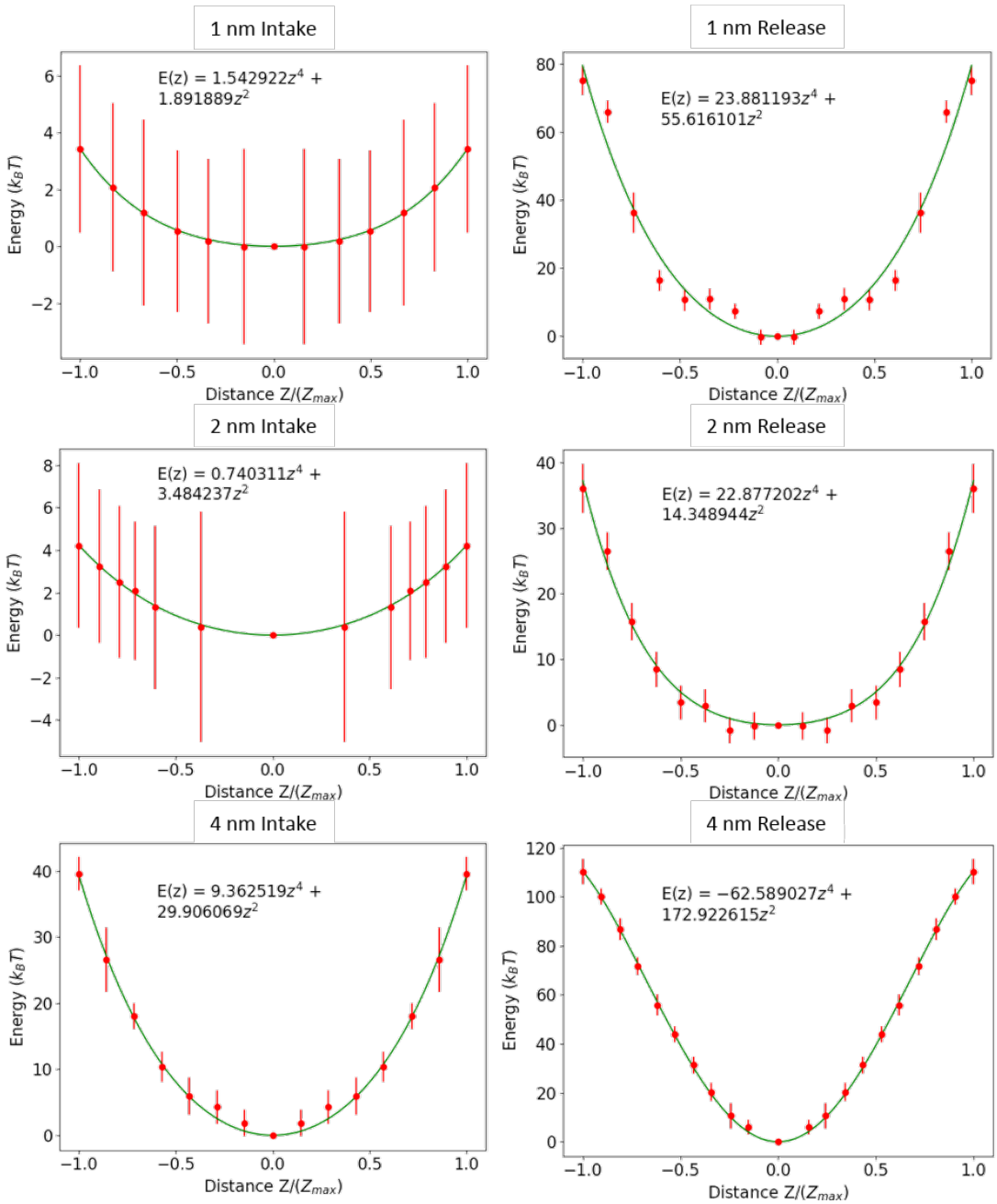

Figure 2.19 – Polynomial regression fit for all systems

The fit is restricted such that $E(0) = 0$ and $\partial E(Z)/\partial Z = 0$. Equations for $E(z)$ for each event are also provided.

2.3.4.2 Dynamics of NP Release

The FP equation (2.8) requires initial and boundary conditions which reflect the physics of the process under consideration. In the case of release of an encapsulated NP from the LB, we deal with a symmetric system. At time zero, the NP is placed in the equilibrium position at the center of the LB and can diffuse inside the free energy potential well until it achieves the edge of the potential barrier on either side of the LB at $Z = \pm 1$ and is released. In this case, the initial condition is represented by δ-function at $Z = 0$. The system has absorbing boundary conditions:

$$W(Z, \tau) = \delta(Z_0) \text{ at } \tau = 0 \tag{2.9a}$$

$$W(Z, \tau) = 0 \text{ at } Z = \pm 1 \tag{2.10a}$$

Pairing (2.8), (2.9a), and (2.10a) with the free energy landscape $E(Z)$ obtained by the GT simulation, (2.2), the particle location probability distribution function, $W(Z, \tau)$, is found. The inner term in (2.8), represents the probability flux, $J(\tau) = [\partial E(Z)/\partial Z \; W(Z, \tau) + \partial W(Z, \tau)/\partial Z]$, allowing (2.8) to be rewritten as $\partial W(Z, \tau)/\partial \tau = \partial J/\partial Z$. The translocation probability, defined as the probability of approaching the system boundaries at given time τ, $P_{\mathrm{T}}(\tau)$, is equaled to the sum of the probability fluxes at the boundaries,

$$P_{\mathrm{T}}(\tau) = J|_{Z=1} - J|_{Z=-1} \tag{2.11a}$$

The probability distribution $P_{\mathrm{T}}(\tau)$ is normalized as in the limit of infinite observation time the NP is released with the probability of one, $\int_0^\infty P_T(\tau)d\tau = 1$. The mean time of translocation, $\langle\tau\rangle$, represents the first moment of this distribution,

$$\langle\tau_{\mathrm{T}}\rangle = \int_0^\infty \tau\, P_{\mathrm{T}}(\tau)d\tau \quad . \tag{2.12a}$$

Alternatively, the mean first passage time can be calculated directly using the Kramers method[49] as is done by Su et al.[107,108]

$$\langle\tau_{\mathrm{T}}\rangle = \int_0^1 dZ \exp(E(Z)/kT) \int_0^Z dZ' \exp(-E(Z')/kT) \tag{2.13}$$

In the process of a random walk along the symmetric free energy landscape, the NP makes multiple attempts to achieve the barrier and escape, returning to the initial equilibrium state after each attempt. As such, the dynamics of release may be considered differently. The FP equation with absorbing boundary conditions at $Z = 0$ and $Z = 1$,

$$W(Z,\tau) = 0 \text{ at } Z = 0, 1 \tag{2.10b}$$

describes one translocation attempt which may be either successful, when the NP achieves the barrier at $Z = 1$ and escapes, or unsuccessful when the NP returns to the initial state at $Z = 0$. Note that in this case, the initial δ-function condition must be shifted from $Z = 0$, by a small increment, ΔZ, equal to the finite difference for integration $W(Z,0) = \delta(Z_0 - \Delta Z)$. ΔZ ranges from 0.01 to 0.0001 depending on the system. Smaller ΔZ is selected for higher energy barrier systems to increase precision.

The probabilities of successful translocation into the LB, $p_{\mathrm{T}}(\tau)$, and return to the bulk, $p_{\mathrm{R}}(\tau)$, within given time τ are given by the respective probability fluxes:

$$p_{\mathrm{T}}(\tau) = J|_{Z=1} \text{ and } p_{\mathrm{R}}(\tau) = -J|_{Z=0} \tag{2.11b}$$

Here, we denote the probabilities of successful translocation $p_{\mathrm{T}}(\tau)$ and return $p_{\mathrm{R}}(\tau)$ in small letters to distinguish them from the probability $P_{\mathrm{T}}(\tau)$, associated with multiple attempts of translocation in the symmetric potential well. The average times of successful $\langle\tau_{\mathrm{T},1}\rangle$ and unsuccessful $\langle\tau_{\mathrm{R},1}\rangle$ translocation attempts are given by

$$\langle\tau_{\mathrm{T},1/\mathrm{R},1}\rangle = \int_0^\infty \tau p_{\mathrm{T/R}}(\tau)d\tau / \int_0^\infty p_{\mathrm{T/R}}(\tau)d\tau \tag{2.12b}$$

Subscript "1" stands for the single translocation attempt. The normalization constants in (2.12b) equal the probabilities of successful p_{T} and unsuccessful p_{R} translocation within one translocation attempt, $p_{\mathrm{T}} = \int_0^\infty p_{\mathrm{T}}(\tau)$, $p_{\mathrm{R}} = \int_0^\infty p(\tau), p_{\mathrm{T}} + p_{\mathrm{R}} = 1$. The probability of a successful translocation attempt, p_{T}, allows one to calculate the probability, $p_{\mathrm{T},n}$, that the translocation occurs during the *n*-th translocation attempt. This means that the first (*n*-1) attempts failed and the NP returned to the initial state at $Z = 0$, but the *n*-th attempt is successful. Thus, since the translocation attempts are statistically independent,

$$p_{\mathrm{T},n} = p_{\mathrm{T}}(1 - p_{\mathrm{T}})^{n-1} \tag{2.13}$$

The mean number of attempts needed for successful translocation,

$$\langle n\rangle = \sum_1^\infty n p_{\mathrm{T},n} = p_{\mathrm{T}} \sum_1^\infty n(1 - p_{\mathrm{T}})^{n-1} = 1/p_{\mathrm{T}} \tag{2.14}$$

The mean time of translocation, $\langle\tau_{\mathrm{T}}\rangle$, is proportional to the mean number of unsuccessful attempts, $\langle n\rangle - 1$, multiplied by the mean time of return $\langle\tau_{\mathrm{R},1}\rangle$ plus the mean time of one successful translocation event $\langle\tau_{\mathrm{T},1}\rangle$,

$$\langle\tau_{\mathrm{T}}\rangle = \langle\tau_{\mathrm{R},1}\rangle(\langle n\rangle - 1) + \langle\tau_{\mathrm{T},1}\rangle \approx \langle\tau_{\mathrm{R},1}\rangle\langle n\rangle \tag{2.15}$$

This equation gives the mean translocation time in dimensionless units reduced to (L^2/D). The approximation in (2.15) holds when $\langle n\rangle \gg 1$ and $\langle\tau_{\mathrm{R},1}\rangle\langle n\rangle >> \langle\tau_{\mathrm{T},1}\rangle$ which is always the case in the systems studied.

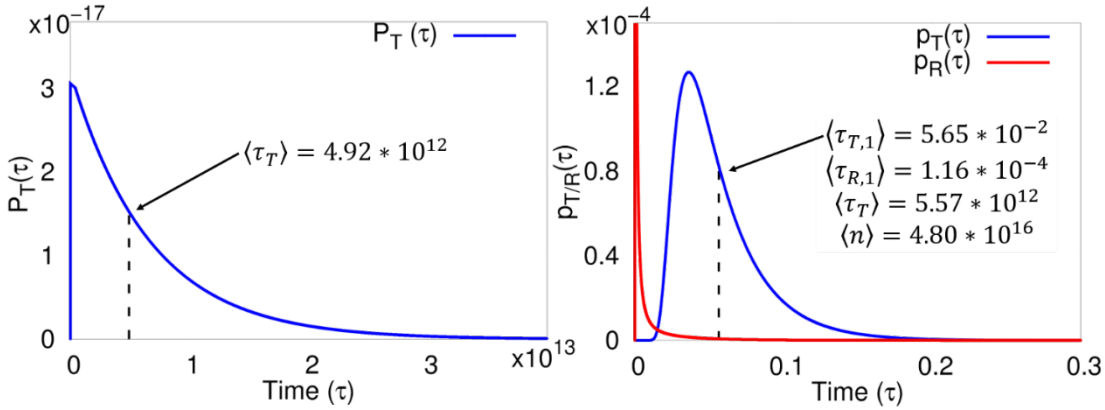

Figure 2.20 – Distributions of the release and return times for the 4 nm NP trapped in the LB core. Time is given is dimensionless units. Left: The probability distribution, $P_{\mathrm{T}}(\tau)$, of the translocation time from the solution of the FP equation with symmetric boundary conditions (2.8) (2.10a). Insert shows the mean translocation time indicated by the broken line. Right: The probability distributions $p_{T/R}(\tau)$ of the successful escape and return time during a single translocation attempt from the solution of FP equation with asymmetric boundary conditions (2.10b). Note the difference in the time scales. Insert shows the mean times of release $\langle\tau_{\mathrm{T},1}\rangle$ and return $\langle\tau_{\mathrm{R},1}\rangle$ during one translocation attempt, the mean number of attempts needed for achieving the successful escape $\langle n\rangle$, and the mean translocation time $\langle\tau_{\mathrm{T}}\rangle$. Note that despite of the huge difference in the timescales, the mean translocation time $\langle\tau_{\mathrm{T}}\rangle$ estimated by the two methods are in reasonable agreement.

A characteristic example of calculation results for the 2 nm NP release obtained by solution of the FP equation with symmetric and asymmetric boundary conditions (2.10b) and (2.11b)) is given in Figure 2.20. The left graph represents the probability distribution, $P_{\mathrm{T}}(\tau)$, of the release time defined as the first passage time of NP diffusion within the symmetric energy landscape. Since this process consists of multiple cycles of NP return to the initial equilibrium state at Z=0, the mean time of translocation $\langle\tau_{\mathrm{T}}\rangle$ is very large, of the order of 10^{13} in dimensionless units. The right graph represents the probability distributions $p_{\mathrm{T/R}}(\tau)$ of the successful release and return time during a single translocation attempt. This process is defined within the asymmetric energy landscape with the boundary condition (8b). This process has a very short time scale because it describes the escape and return time during a single translocation attempt, of the order of 10^{-4} for the return and 10^{-1} for

release. The probability of release is so small that it requires on average $\langle n \rangle \approx 5\text{x}10^{16}$ attempts for successful translocation. As expected, the mean time of translocation $\langle \tau_T \rangle$ estimated via (2.15), that is proportional to $\langle n \rangle$, reasonably agrees with $\langle \tau_T \rangle$ found via the symmetric case solution. Both estimates agree well with the Kramers relationship that gives $\langle \tau_T \rangle \approx 5\text{x}10^{12}$. It is worth noting, that solution of the FP equation with asymmetric boundary conditions is more computationally efficient, especially for the systems with large energy barriers, than with the symmetric boundary conditions due to the significant timescale difference. Also, it contains a more detailed description of the physics of translocation. At the same time, the Kramers relationship (2.13) provides a direct easy method for calculating the mean translocation time. Results of calculations are summarized Table 2.2.

Table 2.2 – Dynamics of the NP release

	1 nm	**2 nm**	**4 nm**
Energy barrier, ΔE (kT)	75.1	37.2	110.3
Translocation scale, L (nm)	7.40	7.71	10.28
Time unit, L^2/D (s)	$2.23 * 10^{-7}$	$4.85 * 10^{-7}$	$1.72 * 10^{-6}$
Mean translocation time, $\langle \tau_T \rangle$	$2.21 * 10^{30}$	$4.90 * 10^{12}$	$5.38 * 10^{43}$
Number of escape attempts, $\langle n \rangle$	$1.06 * 10^{35}$	$4.80 * 10^{16}$	$8.20 * 10^{48}$

The translocation probability and characteristic time is mainly determined by the height of the energy barrier. Interestingly, that the energy barrier for release is not monotonic – the 2 nm NP has the lowest energy barrier for release. To overcome this barrier is takes about $5\text{x}10^{16}$ attempts, yet it's feasible to escape with a reasonable physiological time (this estimate is made assuming the SE diffusion coefficient). For 1 and 2 nm NPs the energy barriers are too high, and the release probability is so small, that it would require an unrealistic number of attempts. The high energy barriers are explained by the mechanism of interfacial NP transfer related to the membrane bending, formation and rupture of lipid

junctions, as discussed above in Section 0. The 1 nm NP nicely fits the LB hydrophobic core and thus is strongly retained. Diffusion of 4 nm NP release from the membrane requires substantial LB deformation that is restricted by the condition of constant tension.

2.3.4.3 Dynamics of NP Intake

NP transport in the process of intake is physically different, as the system is asymmetric – the successful translocation occurs only in one direction, towards the LB. In order to translocate inside the membrane, the NP has to first diffuse from the bulk toward the membrane and then to attempt to overcome the energy barrier by diffusion along the free energy landscape. This attempt may be either successful or unsuccessful. If the translocation attempt is unsuccessful, the NP returns to the bulk and this cycle of external diffusion and translocation attempts are repeated until the NP successfully reaches the edge to the energy barrier and translocates into the membrane. The characteristic time of the external diffusion stage depends on the environment outside the membrane and can be estimated as $t_{\text{ext}} = L_{\text{ext}}^2/D$, where L_{ext} is the characteristic length of the external diffusion. One may expect that depending on the environment, L_{ext} varies on the order from microns to millimeters. Therefore, the Stokes-Einstein equation for NP diffusion provides an estimate for t_{ext} ranging from 10^{-3} to 10^{3} sec for NPs of different size.

The FP equation (2.8) with absorbing boundary conditions (2.11b) describes the dynamics of a single translocation attempt. The probabilities and mean times of successful and failed translocation attempts, and the mean number of attempts needed for the successful translocations are given by (2.10a)-(2.14). Accounting for the mean time of

external diffusion during each of the translocation attempt cycles, the mean time of translocation $\langle t_{\mathrm{T}} \rangle$ is given by the similar equation as (2.14) for the mean time of release,

$$\langle \tau_T \rangle = \big(\langle \tau_{\mathrm{R},1} \rangle + \tau_{\mathrm{ext}}\big)(\langle n \rangle - 1) + \langle \tau_{\mathrm{T},1} \rangle \approx \ \tau_{\mathrm{ext}} \langle n \rangle \tag{2.14}$$

Here $\tau_{\mathrm{ext}} = t_{\mathrm{ext}}/(L^2/D)$ is the dimensionless mean time of external diffusion. The approximate equality holds for all cases considered, since the time of external diffusion significantly exceeds the time of return, $\tau_{\mathrm{ext}} \gg \langle \tau_{\mathrm{R},1} \rangle$, the number of attempts $\langle n \rangle \gg 1$, and the time of the single successful translocation attempt makes insignificant contribution compared with the time of multiple return cycles. In the real units of time, (2.15) converts into

$$\langle t_T \rangle = \big[\langle \tau_{R,1} \rangle (\langle n \rangle - 1) + \langle \tau_{T,1} \rangle\big](L^2/D) + t_{ext}(\langle n \rangle - 1) \approx t_{ext} \langle n \rangle \tag{2.15}$$

Table 2.3 – Dynamics of NP intake. $\langle t_T \rangle$ provided considers external diffusion with $L =$ 1μm and NP respective SE diffusion coefficient. All times (except the last) are dimensionless

	1 nm	**2 nm**	**4 nm**
Energy barrier, ΔE (kT)	3.4	4.2	39.6
Translocation scale, L (nm)	1.86	1.58	6.73
Time unit, L^2/D (s)	$1.41 * 10^{-8}$	$2.03 * 10^{-8}$	$7.40 * 10^{-7}$
Single attempt return time $\langle \tau_{R,1} \rangle$	$4.53 * 10^{-3}$	$1.84 * 10^{-3}$	$2.63 * 10^{-5}$
Single attempt escape time $\langle \tau_{T,1} \rangle$	0.187	0.168	$4.06 * 10^{-2}$
Number of escape attempts, $\langle n \rangle$	430	1710	$1.15 * 10^{18}$
Mean translocation time, $\langle t_T \rangle$ (s)	1.6	14.0	$1.89 * 10^{16}$

The results of simulations are summarized in Table 2.3. The energy barriers of intake are substantially lower than those of release. The energy barriers of several kT for small NPs do not represent any hindrance for translocation, as the required number of attempts does not exceed several thousand. Several thousand attempts translate into the timescale of intake on the order of seconds, assuming that the characteristic scale of external diffusion is in microns.

The energy barrier, ΔE, and respectively the number of required translocation attempts, $\langle n \rangle$, dramatically increases with the NP size, scaling exponentially with the energy barrier, $\langle n \rangle \sim e^{\Delta E/kT}$, as shown in Figure 2.21. For the 8 nm NP, the energy barrier amounts $\Delta E \approx 40\ kT$ and the respective number of required translocation attempts is $\langle n \rangle \approx 10^{18}$. At these conditions, the characteristic time of intake, $\langle t_T \rangle$, is determined by the time of external diffusion t_{ext}, (2.14) which, by any conservative estimates, exceeds milliseconds. That leads to absolutely unrealistic probability of unforced encapsulation.

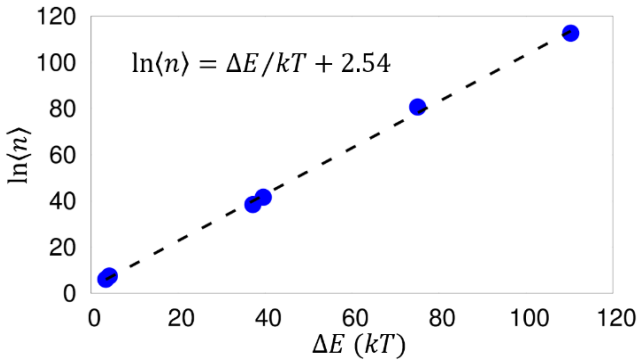

Figure 2.21 – Scaling of $ln\langle n \rangle$ as a function of the energy barrier, ΔE.

2.3.4.4 Comparison of Calculated Mean First Passage Times

Given below in Table 2.4 is a comparison of the estimates of the first passage times calculated with various methods.

Table 2.4 – Comparison of mean first passage times calculated with different techniques and different boundary conditions. Methods presented are Kramers, symmetric boundary conditions FP and asymmetric boundary condition FP. Symmetric and asymmetric FP use numerical integral, whereas Kramers is solved analytically. Times given in seconds.

	1 nm Intake	2 nm Intake	4 nm Intake	1 nm Release	2 nm Release	4 nm Release
Energy Barrier (kT)	3.4	4.2	39.6	75.1	37.2	110.3
L (nm)	1.86	1.58	6.73	7.40	7.71	10.28
Time Unit L^2/D (s)	$1.41 * 10^{-8}$	$2.03 * 10^{-8}$	$7.40 * 10^{-7}$	$2.23 * 10^{-7}$	$4.85 * 10^{-7}$	$1.72 * 10^{-6}$

$\langle \tau_T \rangle$ Kramers	1.86	2.70	$3.14 * 10^{13}$	$2.21 * 10^{30}$	$4.90 * 10^{12}$	$5.38 * 10^{43}$
$\langle \tau_T \rangle$ Symm.	2.14	3.69	$3.33 * 10^{13}$	Integration Fails	$4.92 * 10^{12}$	Integration Fails
$\langle \tau_T \rangle$ Asymm.	2.20	3.84	$3.00 * 10^{13}$	$7.77 * 10^{30}$	$5.57 * 10^{12}$	$8.01 * 10^{44}$
$\langle n \rangle$	430	1710	$1.15 * 10^{18}$	$1.06 * 10^{35}$	$4.80 * 10^{16}$	$8.20 * 10^{48}$

Numerical integration for the asymmetric boundary condition FP begins to fail at the two higher energy barriers (75 kT and 110 kT) hence the order of magnitude difference between the Kramers value and numeric integration solution. For the symmetric boundary condition system, numerical integration fails after ~40 kT (the integration does not converge). Expectation times between the three methods agree well indicating they describe the same process. As discussed in the main text, the asymmetric FP has the advantage that it can be used to find the average number of attempts the particle makes before successfully escaping. After each attempt, the NP may diffuse in the bulk before making another attempt. This process describes the process a NP entering the LB would take. The discrepancy in time between the symmetric and asymmetric FP solutions described in the main text is a result of bulk diffusion. When bulk diffusion is ignored, the two descriptions agree.

Figure 2.22 illustrates the difference in time distributions and probability density distributions functions for the symmetric and asymmetric boundary conditions. The 1 nm NP is taken as a case example. Both images below represent the same energy barrier. As can be seen, the times between the two cases are comparable.

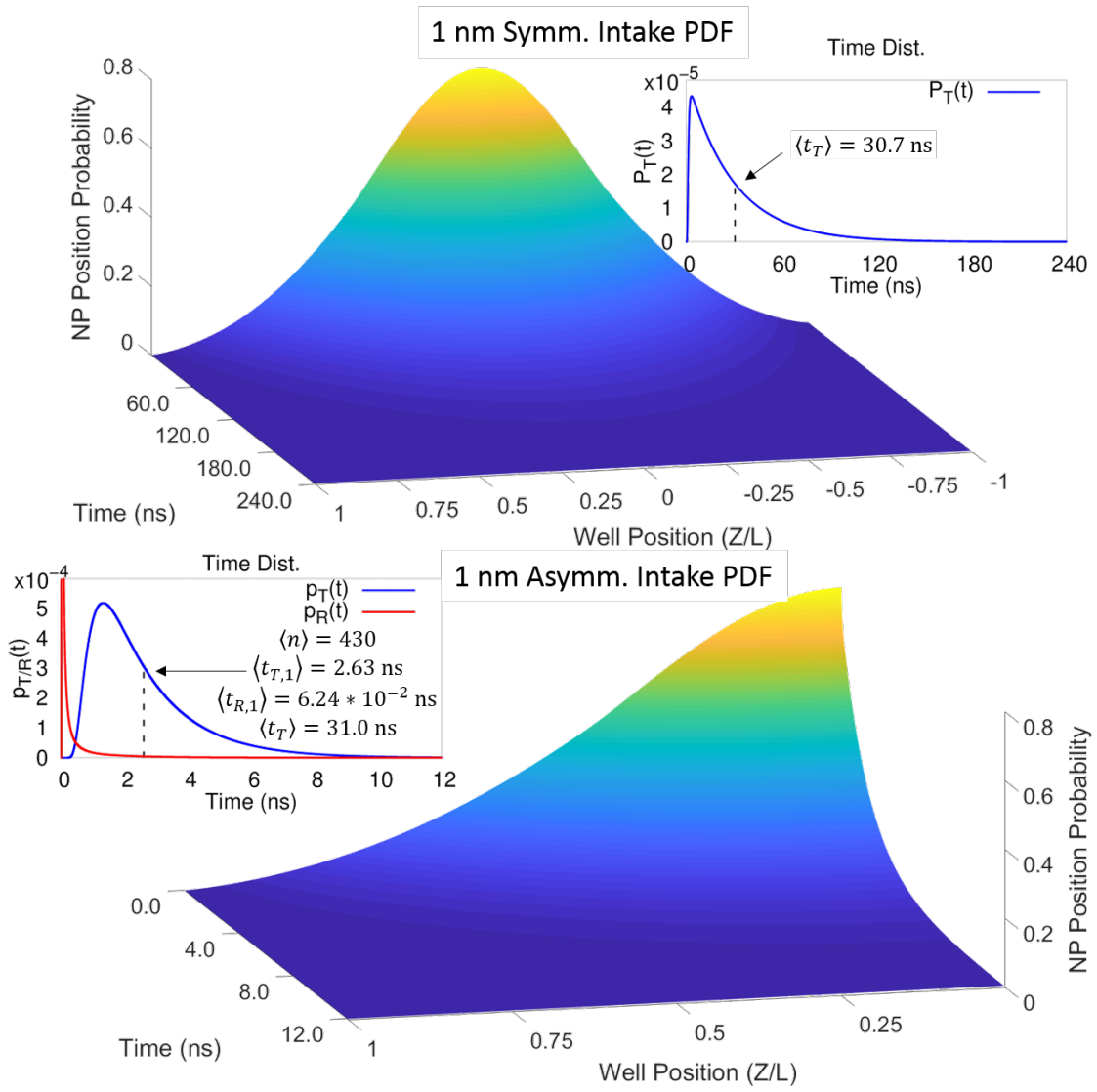

Figure 2.22 – $W(Z,\tau)$, Position probability density distribution for a particle inside a polynomial energy well for the symmetric case (top) and asymmetric case (bottom) (initial position not shown). Boundaries are ±1 with symmetric boundary conditions and 0,1 with asymmetric boundary conditions. The inserted figures show the normalized insertion probability time distribution $P_T(t)$; the time distribution for the NP to escape the well. The blue line represents the time distribution for successful translocation, and red (in the case of FP with asymmetric B.C.s), an unsuccessful attempt with the NP returning to the bulk. The dotted black line represents the mean first passage time for one attempt equal to the mean first passage time, $\langle\tau\rangle$ and $\langle\tau_T\rangle$ for the symmetric and asymmetric cases respectively.

Because the initial point is a delta function, the first few points in Figure 2.22 are

removed for ease of viewing. Figure 2.22 effectively describes the probability a particle

will be in a specific position, Z, and a specific time t. Initially, the particle has probability 1 to be found at Z/L=0. As time proceeds, the probability to find the particle at Z/L=0 decreases, while increasing elsewhere within the well. As $t \to \infty$, the probability the NP escapes the energy well approaches 1. Correspondingly, the PDF flattens and the probability to find the particle in the well, $W(Z, \infty) = 0$.

In the inset of Figure 2.22, the probability the particle successfully escapes the well is presented. After some delay time, the probability the NP escapes the energy well increases until it reaches a maximum. The probability for the NP to escape then begins to decrease until it reaches zero. That is, the probability the NP has escaped is 1. The average escape time can be calculated by finding the average value of the function previously described, $\overline{p_T}(t)$. All NP intake/release events are qualitatively similar to Figure 2.22 since they are all represented by a 4th ordered polynomial.

2.4 Conclusions

Using DPD simulations, we investigated the interactions between LB membranes at isotension conditions and hydrophobic NPs covered by the equilibrium LM. A novel simulation setup was developed, permitting us to probe the force of NP-LB interaction and to calculate the free energy landscapes of NP intake and release. The simulations were performed for particles of 1 (comparable with the LB hydrophobic core thickness), 2 (comparable with the LB thickness), and 4 nm (exceeding the LB thickness), interacting with a DMPC bilayer held at isotension conditions. We reveal the mechanisms of NP intake and release, which are associated with irreversible spontaneous interfacial transitions. In the course of intake, hydrophobic NP must overcome the resistance of the water interlayer

between particle and membrane, which prevents fusion of the LM coating and the outer leaflet of the membrane. As the result, the membrane bends counter-balancing the disjoining pressure in the water interlayer until the latter becomes unstable and ruptures allowing for rapid absorption of monolayer lipids by the membrane and spontaneous encapsulation of NP in the LB exterior. The process of release of encapsulated NPs involves membrane deformation and formation of a lipid junction retaining the NP, which extends and eventually breaks; upon the junction break-up, the LM-coated NP spontaneously detaches.

The energetics of the intake and release processes was characterized by the respective free energy landscapes calculated with the GT method. Noteworthy, due to the spontaneous interfacial transitions no continuing translocation trajectory exists. The free energy landscapes of intake and release terminate at the respective points of spontaneous transitions and do not merge. This behavior of lipid pre-coated hydrophobic NPs is distinct from that of bare NPs with continuous translocation trajectories.[95] The interfacial transitions during intake and release are associated with free energy barriers, which depend on the particle size. The dynamics of these transitions was studied by the Fokker-Planck equation mimicking the NP Brownian motion along the calculated free energy landscape. We presented a novel modification of the FP approach, which accounts for the external diffusion of NP during the intake attempts. This factor has not been considered in prior works and, as shown here, it significantly affects the mean translocation time. This FP method allowed us to establish the relationships for the probabilities of intake and release transition and characteristic time needed for the successful translocation. We found a linear scaling between the translocation probability and the energy barrier.

While the energy barrier and respectively the rate of intake monotonically increase with the NP size, the rate of release does not scale exhibits a pronounced maximum for 2 nm NPs. The smallest (1 nm) and the largest (4 nm) particles have significantly higher energy barriers than the 2 nm particle. At the same time, the barriers of intake for small (1 and 2 nm) particles are negligible so that such particles would be eagerly encapsulated by lipid membranes and retained due the high release energy barriers. This conclusion is consistent with experimental observations from the literature that hydrophobic NPs comparable in size to the LB thickness remain inside the LBs without a chance to escape within reasonable time limits.[31, 108-110] For 4 nm NP, the energy barriers for both intake and release are significantly higher compared to those of 1 and 2 nm NPs, that makes unforced trans-membrane transfer of NP larger than ~2 nm hardly probable.

It follows from our analysis that there is an optimal size for the unforced trans-membrane transfer of hydrophobic NPs by the encapsulation-release mechanism. While 2 nm NPs may swiftly penetrate the membrane core and then escape within reasonable timeframe, 1 nm NPs are captured by the hydrophobic core and strongly retained, and 4 nm NPs experience prohibitively high-energy barrier preventing their intake. Moreover, if 8 nm NP is encapsulated by the membrane, it is strongly retained, and its release is restricted by prohibitively high barrier. Noteworthy, that the mechanism of encapsulation in the membrane interior we considered is different from the mechanism of NP wrapping by the membrane, which is possible only if the NP size exceeds a certain threshold. [111-113]

It is worth noting that here are multiple factors affecting trans-membrane transport that are not present in our simplistic coarse-grained models of the lipid membrane and its environment and should be addressed in the further studies. First, we consider an ideally

homogeneous LB without any defects and inclusions, which may facilitate NP translocation. Second, we do not consider any additives in the solvent. Third, the NP is round, smooth and chemically uniform without any ligands and hydrophilic entities. It is expected that non-spherical NPs with non-uniform hydrophobicity may translocate easier. Fourth, our estimates are done for one nanoparticle ignoring cooperative effects, like accumulation of small NPs inside the LB. Finally, our DPD model of water does not account for the long-range effects of the disjoining pressure in the thin water layers between NPs and membranes.[114, 115] These long-range interactions may prevent LB-LM fusion and hinder NP intake. In order to evaluate NP translocation through real cell membranes, this list must be expanded to account for their multicomponent nature, presence of cholesterol and proteins, inherent morphological defects (e.g. gel islands and rafts), and electrostatic interactions involving charged membrane components and solvent ions, etc. Further studies should also address the cooperative effects of nanoparticle interactions outside and inside the membrane to explore their possible aggregation.

Despite of the aforementioned reservations, the proposed model to study the NP-LB interactions sheds lights on the specifics of the mechanisms and dynamics of NP adhesion, intake and release, provides instructive quantitative estimates, and lays down a foundation for exploring more complex interfacial phenomena in biological environments. The conclusion about the existence of an optimal NP size for unforced translocation through the membrane may have practical implications for the choice of NPs for intracellular drug delivery and imaging.

3 Nanoparticle Engendered Rupture of Lipid Bilayers

This chapter is based on work that has been published to the reference shown below, and was used within the author rights as established with publishing company:

- Burgess, S., et al. Nanoparticle Engendered Rupture of Lipid Bilayers. *J. Phys. Chem. Lett.* **2018,** 9 (17), 4872-4877

3.1 Background and Motivation

A better understanding of the nanoparticle engendered mechanisms of membrane instabilities is required for developing new nanoparticle biotechnologies as well as for evaluating health threats related to nanoparticle manufacturing. In chapter, we explore tension-induced rupture of lipid membranes with encapsulated nanoparticles using dissipative particle dynamics (DPD) simulations.

Lipid-based membranes are prone to rupture under stress or being affected by external stimuli. The first thermodynamic theory of membrane rupture was suggested by Deryagin and Gutop (DG)[116] based on the classical nucleation theory (CNT) applied to a homogeneous two-dimensional free film. The DG model implies that film rupture is triggered by nucleation, due to thermal fluctuations, of an unstable hole (pore), which grows spontaneously upon achieving a certain critical size. The hole nucleation is controlled by the membrane surface tension, σ, and the line tension Γ, which represents the excess energy of the membrane edge per unit length. The work of formation of a round hole of radius r equals the difference between the work of formation of the hole edge of length $2\pi r$ and the work of extension the membrane area by πr^2,

$$E(r,\sigma) = 2\pi r\Gamma - \pi r^2\sigma \tag{3.1}$$

$E(r,\sigma)$ achieves maximum at $r_c = \Gamma/\sigma$, which represents the size of critical hole nucleus: holes of $r < r_c$ are reversible, while holes of $r > r_c$ expand irreversibly. The work of formation of the critical nucleus,

$$E_c = E(r_c,\sigma) = \pi r_c^2 \sigma = \pi\Gamma^2/\sigma \tag{3.2}$$

represents the free energy, or nucleation (activation) barrier of expanding hole formation, which is the main quantitative parameter for predicting the probability and kinetics of film rupture. The nucleation barrier determines the rate constant, k_f, of film rupture,

$$k_f = A_{f,0}\exp(-E_c/k_BT) = A_{f,0}\exp(-\pi\Gamma^2/\sigma k_BT), \tag{3.3}$$

$A_{f,0}$is the kinetic rate pre-factor that depends on the film area and lipid mobility.[117]

Lipid membrane rupture has been studied by various theoretical methods[118-121] to predict the membrane line tension, which may depend on the membrane and hole curvatures, membrane tension and bending rigidity, charge distribution, and other factors. The line tension is used to build the energy dependence $E(r,\sigma)$, which may have a non-trivial shape with minima, corresponding to stable or metastable holes, and maxima, corresponding to the nucleation barriers[122-124]. The reported values of the line tension and lysis tension (characteristic tension of rupture) of lipid membranes tend to be larger in simulated systems ($\Gamma = 12-40$ pN; $\sigma_c = 20-40$ pN/nm)[125-127], when compared to experimental systems ($\Gamma = 4-28$ pN; $\sigma_c = 5-7$ pN/nm)[124, 128-130] due, in part, to the 9 orders of magnitude difference in observation time. As a result of the time difference, the critical energy barrier of membrane rupture in a simulated membrane must be reduced in order to observe membrane lysis tension, which requires much larger applied surface tensions. The resulting differences in line tension may then be explained by the work of

Akimov et al.[131] who showed that membrane line tension depends strongly on membrane surface tension.

It is worth noting that the DG model is purely macroscopic and does not account for the molecular features of the lipid interfaces that are important at the nanoscale level of critical nuclei. Nevertheless, the DG model in its original and modified forms, has been widely used for interpretation of experimental, as well as molecular simulation data[132, 133] referenced throughout this Letter. In particular, Levadny et al[130] studied the tension-driven rupture of giant unilamelar vesicles (GUV) by the micropipette suction method[134] during the incremental increase of membrane tension σ. With repeating experiments, the authors determined the probability $P_f(t,\sigma)$ of the membrane rupture within given time *t* at fixed tension σ. The rupture probability $P_f(t,\sigma)$ as a function of σ was correlated with the predictions of the classical Kramers dynamics theory[135] that implies the Poissonian stochastic process of hole formation with the rate constant k_f determined by the energy barrier via

$$P_f(t,\sigma) = 1 - \exp\left(-k_f t\right) \tag{3.4}$$

From this correlation, the authors determined the line tension, Γ. This approach with various modifications was applied for interpretation of experimental studies of homogeneous lipid membranes of different type[136-138]. Below, we extend this method to analyze the stability of nanoparticle-loaded membranes *in-silico*.

Unfortunately, we are not aware of any experimental studies of heterogeneous hole nucleation engendered by adhered or encapsulated nanoparticles that is the focus of our work. While various simulation studies monitored the process of particle assisted membrane rupture[11, 139, 140], very few consider the NP effect on the nucleation barriers of

hole formation. By using SCFT, Ting and Wang[141] calculate free energy barriers for NPs to cross LBs. They showed different mechanisms of hydrophobic NP translocation through LB associated with NP-induced LB rupture: NP encapsulation followed by NP release and membrane relaxation, and NP encapsulation followed by membrane rupture. Yue et al.[34] employed DPD simulations to study membrane rupture triggered by rotating NPs brought into contact with LBs. The authors found that a critical surface tension exists, above which the membrane ruptures. The studies by Ting et al. and Yue et al. provide methods in order to calculate the energy and tension required to rupture a membrane with encapsulated particles, however a robust theoretical model capable of predicting how particle encapsulation affects membrane stability is lacking. In this work, the heterogeneous nucleation is treated in terms of an original theoretical model by introducing an effective contact angle on the three-phase, hole-membrane-solid, boundary into the DG theory.

3.2 Models and Methods

All systems are run in a box size of 30x60x25 R_c with a timestep of 0.01τ where $\tau = 88\,ps$, using the velocity Verlet algorithm. Calculations are performed using DL-Meso Open Source Software[142] run on the Extreme Science and Engineering Discovery Environment (XSEDE)[98]. The DPD model and simulation details are identical to those presented in the previous chapter.

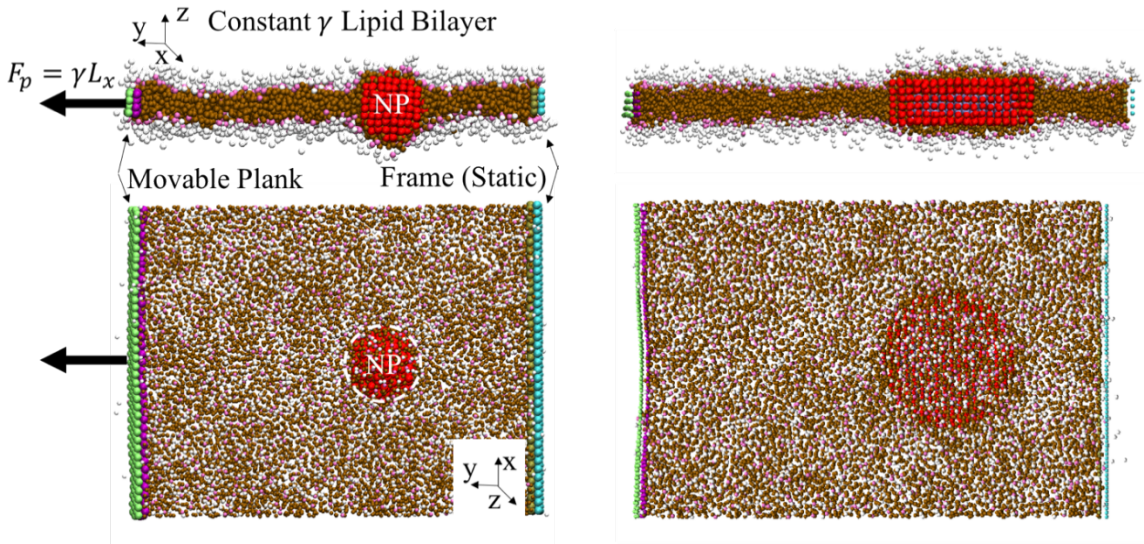

Figure 3.1- Initial state for rupture testing of the spherical NP-LB (left) and initial state for rupture testing of the cylindrical NP-LB (right)

In DPD simulations, we mimic real experiments with a film placed of a frame with a movable bar, to which a constant force is applied to control the membrane tension, Figure 3.1. The system is presented in the previous chapter in **Error! Reference source not found.**. To create the initial configuration, 1170 lipid molecules are placed between the bars and the system equilibrated under zero surface tension for one million steps (880 ns) to form a stable homogeneous LB. To model a NP-loaded membrane, a hydrophobic NP is placed at the frame center at $z = 0$ (the frame centerline) and is tethered to this location by a GT (Figure 3.1) to keep it from moving to the edges of the system. As a side effect of the tethering, the NP remains in a constant location as the pulling bar moves, causing the NP to be off-center with respect to the bars.

Upon creation of the equilibrated initial configuration, the applied force $\mathbf{F}_p$ is increased in small increments causing an increase of the membrane tension σ. It has been shown by Evans et al. [143] that the lysis tension strongly depends on the rate of tension increase and is distinguished by two kinetic regimes; the slow loading rate regime with

aligns with the DG model where lysis tension values vary little with tension loading rate, and the high loading rate regime where the lipids are not able to rearrange themselves in an equilibrium configuration causing the lysis tension to depend strongly on the rate. With specific interest to this study, Xie et al. used molecular dynamics to simulate both instantaneous and gradual loading rates on dipalmitoylphosphatidylcholine (DPPC)[144]. They observed a slow loading rate regime at 1.8 pN/nm/ns. To stay within this slow loading rate regime, we increase the surface tension at a rate of 0.0228 pN/nm/ns, to a point where preliminary scanning suggests ripping may occur. At this point, the rate is slowed to 0.0057 pN/nm/ns. Statistics are collected over 100 independent repeats with 200,000 steps at each σ to determine the probability $P_r(t, \sigma)$ of the membrane to rupture within given time t at fixed tension σ (membrane rupture probability).

3.3 Theoretical Model

3.3.1 Expanded Deryagin and Gutop Model

To consider the heterogeneous nucleation in the spirit of the DG theory, we present the hole as a circle with excluded lens due to the intersection with NP, as sketched in Figure 3.2. The hole is of quasi-circular shape resembling a 2D bubble residing on the curved NP surface with a certain contact angle at the solid-solvent-lipid points of contact. This 2D geometrical model allows one to calculate the change of the system free energy, $E_p(r, R_p, \Gamma_{ls}, \theta, \sigma)$, due to the formation of a hole of radius r at the NP of radius R_p at the constant tension conditions, which depends on lipid-solvent line tension Γ_{ls}, contact angle θ and given tension σ,

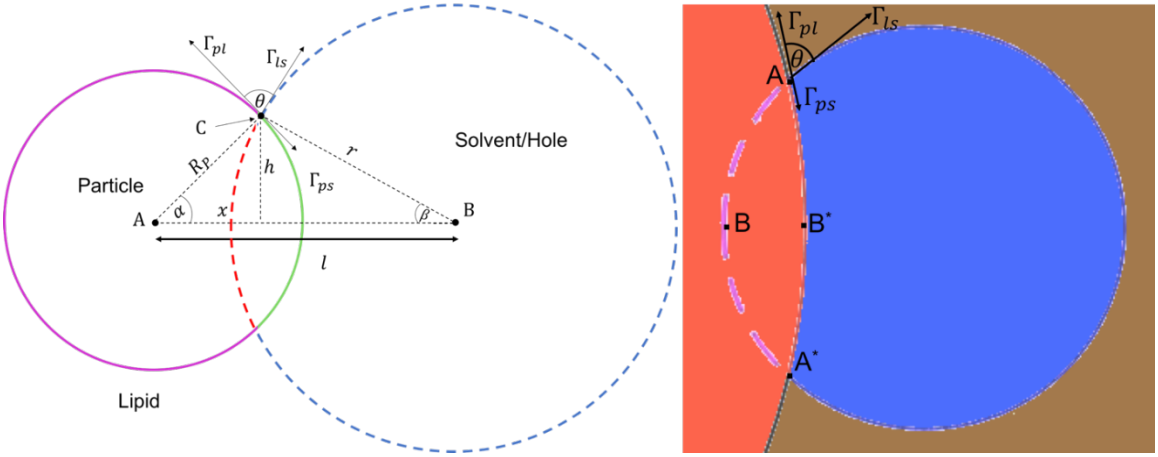

Figure 3.2 – Diagram of particle-hole overlap (left) and a zoom in on the area of interest that illustrates the definition of the contact angle θ at the three-phase solvent-lipid-solid points of contact (points A and A*). The value of $\cos\theta$ is determined from the balance of respective line tensions on lipid-solvent, Γ_{ls}, particle-solvent, Γ_{ps}, and particle-lipid, Γ_{pl}, boundaries (right).

The mechanical equilibrium in this three-phase two-dimensional is model determined by the balance of the line tensions, Γ_{ls}, Γ_{ps}, and Γ_{pl}, of, respectively, lipid-solvent, particle-solvent, Γ_{ps}, and particle-lipid, Γ_{pl},boundaries. The balance of line tensions defines the effective contact angle θ at the three-phase solvent-lipid-solid points of contact via the Young equation:

$$\cos(\theta) = (\Gamma_{ps} - \Gamma_{pl})/\Gamma_{ls} \tag{3.5}$$

Figure 3.2 (left) is described geometrically below.

$$l^2 = r^2 + R_p^2 + 2rR_p\cos(\theta) \tag{3.6}$$

$$x^2 + h^2 = R_p^2;\ \ (l-x)^2 + h^2 = r^2;\ \ x = \left(l^2 + R_p^2 - r^2\right)/2l \tag{3.7}$$

$$\alpha = \mathrm{acos}(x/R_p);\ \ \beta = \theta - \alpha;\ \ \alpha + \beta = \theta \tag{3.8}$$

where l is the length between particle and hole central points, A & B respectively; R_p is the particle radius, r is the hole radius, θ is the contact angle at the particle-hole contact point, C, x is the horizontal distance from A to C, h is the vertical distance from A to C,

α is $\angle$CAB, β is $\angle$CBA. The arc length of hole overlap s_H, and arc length of particle overlap s_p are given by

$$s_H = 2\beta r;\ s_p = 2\alpha R_p \tag{3.9}$$

The area of overlap between the particle and hole

$$A_{overlap} = \left(\alpha R_p^2 - hx\right) + \left(\beta r^2 - h(l-x)\right) \tag{3.10}$$

The expanded DG model is produced in (3.11a). The second two terms in the first (green) line represent the change in hole circumference as a consequence of hole-particle overlap, and the second two terms on the second line (red) represent the change in hole area as a consequence of hole-particle overlap

$$E_p\left(r,\theta,\Gamma_{fs},R_p,\sigma\right) = 2\pi r\Gamma_{fs} - 2\beta r\Gamma_{fs} + 2\alpha R_p\left(\Gamma_{ps}-\Gamma_{fp}\right) - \left[\pi r^2 - \left(\alpha R_p^2 - hx\right) - \left(\beta r^2 - h(l-x)\right)\right]\sigma \tag{3.11a}$$

where blue represents the terms in the original DG equation. Simplifying (3.11a) and using (3.5) we obtain the final expression

$$E_p\left(r,\theta,\Gamma_{fs},R_p,\sigma\right) = 2(\pi-\beta)r\Gamma_{fs} + 2\alpha R_p\Gamma_{fs}\,cos(\theta) - \left[(\pi-\beta)r^2 - \alpha R_p^2 + hl\right]\sigma \tag{3.12b}$$

This can be understood more simply using Figure 3.2 (right).

$$E_p\left(r,R_p,\Gamma_{ls},\theta,\sigma\right) = [2\pi r - l_{ABA^*}]\Gamma_{fs} + l_{AB^*A^*}\left(\Gamma_{ps}-\Gamma_{fp}\right) - [\pi r^2 - A_{AB^*A^*B}]\sigma =$$

$$= [2\pi r - l_{ABA^*} + l_{AB^*A^*}\cos(\theta)]\Gamma_{fs} - [\pi r^2 - A_{AB^*A^*B}]\sigma \tag{3.13}$$

Here, l_{ABA^*} and $l_{AB^*A^*}$ are, respectively, the lengths of arcs ABA* and AB*A*, and $A_{AB^*A^*B}$ is the area of lens AB*A*B, all of which depend on $r, R_p,$ and θ. The first term in the LHS of first line of (3.13) corresponds to the work of formation of the hole-lipid boundary of length $2\pi r - l_{ABA^*}$, the second term corresponds to the difference of line energy of solid-

lipid and solid-solvent boundaries of length ABA, and the third term corresponds to the surface energy gained due to formation of the hole of area $\pi r^2 - A_{AB^*A^*B}$

3.3.2 Probability of Rupture

The energy barrier determines the rate of heterogeneous nucleation in the same fashion as within the DG model does in case of homogeneous nucleation,

$$k_p = A_p \exp\left(-E_{p,c}/k_B T\right) \tag{3.14}$$

The proposed extension of the DG model to heterogeneous nucleation of holes in LB at the surface of encapsulated NPs is purely macroscopic and can be justified only for large particles of size significantly exceeding the LB thickness. However, as shown below it provides a useful insight on the heterogeneous mechanism of membrane rupture on the same level of accuracy as the original DG model for the homogeneous nucleation. In case of NP-loaded membranes, the rupture may be initiated by either heterogeneous or homogeneous nucleation, and the rupture probability $P_r(t, \sigma)$ is determined with the sum of the respective rates k_f (3.3) and k_p (3.14),

$$P_r(\sigma, t) = 1 - \exp\left(-\left(k_f + k_p\right)t\right) , \tag{3.15}$$

with the pre-factors depending on the system size and NP size.

3.3.3 Modifying the Pre-Exponential Factor as a Function of NP Size

In the case of 2 and 3 nm NPs, both homogeneous and heterogeneous nucleation need to be accounted for according to (3.15). Because the pre-exponential factor is determined for the largest system the dynamic pre-factors must be adjusted to account for the system geometry. The pre-factor for heterogeneous nucleation is scaled with respect to the NP radius as

$$A_p = A_{p,0} * R_p / R_{p,0} \tag{3.16}$$

Where $A_{p,0}$ is the pre-exponential factor found the reference system (4 nm NP) and $R_{p,0}$ is the radius of the reference NP (4 nm). The pre-factor $A_{f,0}$ for homogenous nucleation is adjusted by subtracting from the membrane area the area occupied by NP where the homogeneous nucleation cannot be initiated,

$$A_f = A_{f,0} * \left(S_p - \pi R_p^2\right) / S_0 \tag{3.17}$$

where S_0 is the total surface area of the homogenous membrane, S_p is the total surface area of the membrane under consideration, and $A_{f,0}$ is the pre-exponential factor for the unloaded membrane (3.3).

3.3.4 Special Considerations for Spherical Particles

The DG model considers two-dimension membranes as does our expanded DG model. When a spherical particle has a much larger diameter than the membrane thickness, this may be a reasonable approximation as the particle is approximately cylindrical with respect to the membrane. Therefore, each two-dimensional slice perpendicular to the coordinate of membrane thickness is approximately equal and Figure 3.3 remains constant throughout the thickness of the membrane. If particle diameter is comparable to membrane thickness, a cylindrical approximation does not hold as particle size changes with each two-dimensional slice. Accordingly, particle diameter relative to membrane thickness is considered for spherical particles. While Figure 3.3 views the membrane perpendicular to the XY plane, Figure 3.3 views the membrane parallel to the

XY plane. In this view, particle radius with respect to membrane height, r_{mod} is *not* constant.

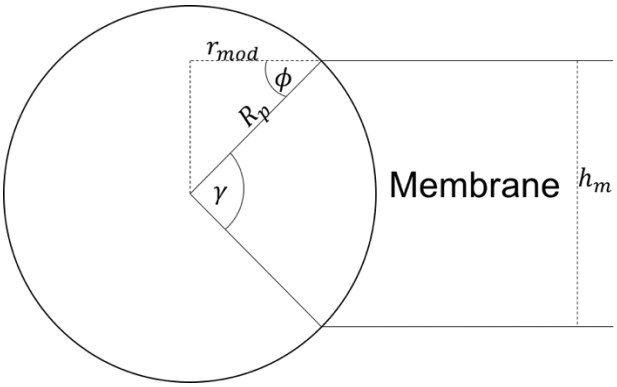

Figure 3.3 – Side view of membrane with submerged NP. For each 2-D slice of the membrane, the relative particle radius, r_{mod}, is not constant; rather it depends on the static NP central angle with LB edges, γ, and the variable angle, ϕ, that depends on the value of z within the membrane. $\phi = 0$ at $z = 0$, the membrane center.

We modify R_p as the average submerged particle radius $\bar{r}(R_p)_{mod}$ along the entire membrane height.

$$r_{mod}(\phi) = \begin{cases} 0 & for\ y < \frac{h_m}{2} - R_P \\ R_p \cos(\phi) \text{ for } \frac{h_m}{2} - R_P \le y \le \frac{h_m}{2} + R_P \\ 0 & for\ y > \frac{h_m}{2} + R_P \end{cases} \tag{3.18}$$

$$\bar{r}_{mod} = \frac{1}{b-a}\int_a^b r_{mod}(\phi)d\phi = \frac{R_P}{\gamma}\int_{-\gamma/2}^{\gamma/2} \cos(\phi)\, d\phi \tag{3.19}$$

$$\bar{r}(R_p)_{mod} = \begin{cases} \frac{2R_P}{\gamma}\sin(\gamma/2) \text{ for } R_{NP} \ge h_m \\ \frac{2R_P}{h_m}\left[\frac{2R_P}{\gamma}\sin(\gamma/2)\right] \text{ for } R_{NP} < h_m \end{cases} \tag{3.20}$$

$$\gamma = \begin{cases} 2\sin^{-1}\left(\frac{h_m}{2R_P}\right) \text{ for } R_P \ge h_m \\ \pi \qquad\qquad \text{for } R_P < h_m \end{cases} \tag{3.21}$$

In this case, we equivalently compare the side surface areas of cylinders with area $2\pi\bar{r}(R_p)_{mod}h_m$. For cylindrical particles with height equal to membrane thickness, all slices have the same radii, therefore the average observed radius is the same as cylinder

radius. Therefore, this modification is not necessary for a cylindrical particle of height equal to membrane thickness.

3.4 Results

The theoretical predictions are shown by solid lines in Figure 3.4. The calculations are performed without using any adjustable parameters with the values of line tension and contact angle determined for the homogenous system and the 4 nm spherical NP system. The cylindrical curves use the same contact angle, θ, and critical radius, r_c, as the spherical curves. The only fitted parameter for the cylindrical system is the lysis tension, which affects the value of the pre-exponential factor. The results of simulations are shown in Figure 3.4 by symbols.

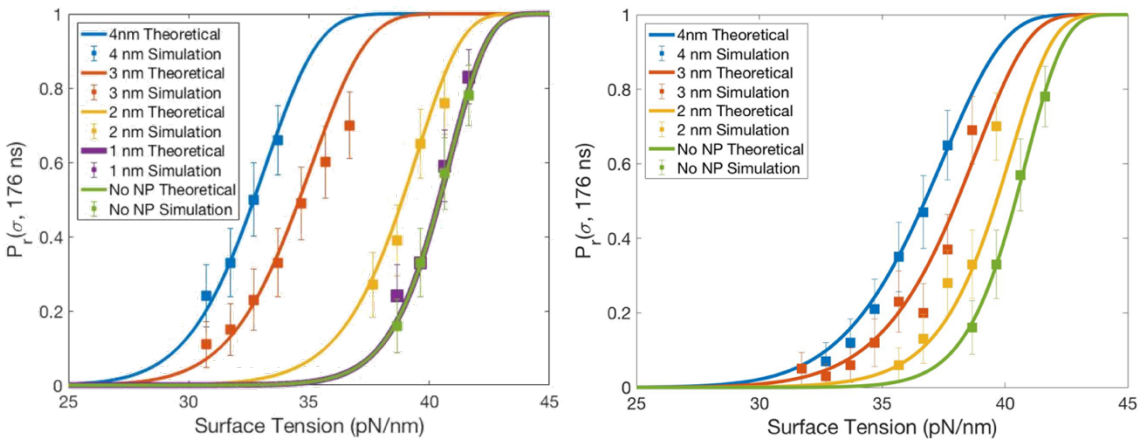

Figure 3.4 – Simulation data (symbols) and theoretical dependence of the rupture probability $P_r(\sigma, t)|_{t=176ns}$ as a function of the applied tension σ for DMPC membrane loaded with spherical (left) and cylindrical (right) particles of different radii. The error bars are calculated using the normal approximation interval with a 95% confidence interval. For a 1 nm NP, no effects of heterogeneous nucleation are found and the theoretical line (magenta) overlaps with the theoretical line for unloaded membrane (green).

The right-most green data corresponds to the homogeneous nucleation in unloaded membrane. The green solid line represents the predictions of the DG model according to

(3.3) and (3.4) with fitted membrane-solvent line tension $\Gamma_{fs} = 39$ pN and dynamic pre-factor $A_{f,0} = 9.4 * 10^{18}/s$. The characteristic tension, at which the 50% probability of rupture is achieved within given observation time of 176 ns (that is equivalent of 200,000 DPD time steps), is σ= 41pN/nm. The obtained value of the line tension is in agreement with the simulation and experimental data[126, 128, 145]. NPs of 1 nm radius, which are completely immersed within the hydrophobic interior of the membrane, do not affect the dynamics of hole nucleation significantly and showed no preference to occur near the NP. In contrast, in case of 4 nm NPs, diameter twice as large as the membrane thickness, all nucleation events occurred near the NP surface. In case of 2 and 3 nm nanoparticles, both homogeneous and heterogeneous nucleation events were observed with larger probability of heterogeneous nucleation for larger NPs. The calculated critical radii, lysis tensions, and critical energy barriers of heterogeneous nucleation for the spherical and cylindrical NPs is presented in Table 3.1and Table 3.2 respectively.

Table 3.1- Calculated Critical Radii, Lysis Tensions, and Critical Energy Barriers for Heterogeneous Nucleation of Spherical NPs

NP Radius (nm)	Critical Radius (nm)	Lysis Tension (pN/nm)	Energy Barrier (kT)
4	0.872	33.8	14.1
3	0.850	35.4	14.0
2	0.790	39.5	14.0
1	0.854	40.8	18.2

Table 3.2 - Calculated Critical Radii, Lysis Tensions, and Critical Energy Barriers for Heterogeneous Nucleation of Cylindrical NPs

NP Radius (nm)	Critical Radius (nm)	Lysis Tension (pN/nm)	Energy Barrier (kT)
4	0.787	36.7	12.7
3	0.774	38.1	12.6
2	0.776	39.7	13.0

To determine the contact angle θ, we applied the proposed model of heterogeneous nucleation to reproduce the simulation data for 4 nm NP as in this case no events of homogeneous nucleation were observed. The blue line in Figure 3.4 represents the predictions of the expanded DG model for the 4nm NP system according to (3.15) with fitted contact angle $\theta = 62^{o}$, dynamic pre-factor $A_{p,0} = 1.2 * 10^{13}/\text{s}$ for cylinder and $A_{p,0} = 4.5 * 10^{12}/\text{s}$, and respective critical hole radius $r_c = 0.89$ nm. To be clear, all parameters in the cylindrical system are the same as the spherical system except for the lysis tension, which is used to calculate the pre-exponential factor. A snapshot in Figure 3.5 presents the hole of about this size, which forms the contact angle of about 62^{o} in agreement with the obtained estimate. The lysis tension, within given observation time of 176 ns is σ^*= 33 pN/nm for the spherical 4 nm NP and σ^*= 38 pN/nm for the cylindrical 4 nm NP. Note that we assume the membrane-solvent line tension $\Gamma_{fs} = 39$ pN determined for the homogeneous nucleation and ignore its potential dependence on the membrane tension σ.

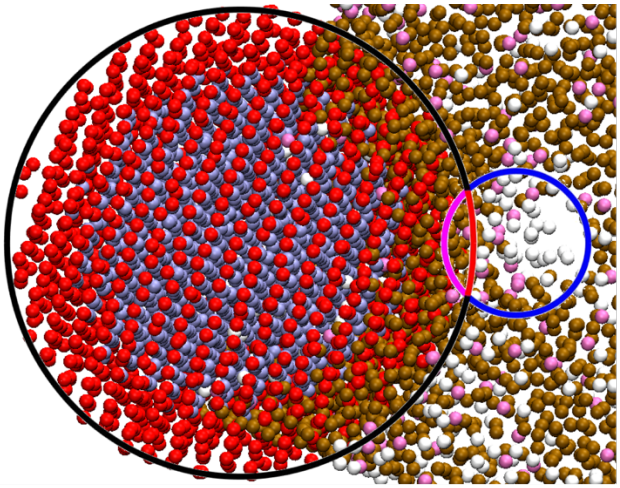

Figure 3.5 – Snapshot of a hole formed at the NP surface overlaid by theoretical prediction of NP-hole overlap (black, blue, red, and pink). The hole is filled by water has

a quasi-circular shape similar to a 2D bubble residing on a curved solid surface. (red – NP, blue – NP core, brown – lipid tails, pink – lipid junction, white – lipid heads)

A typical example of heterogeneous hole progression is presented in Figure 3.6.

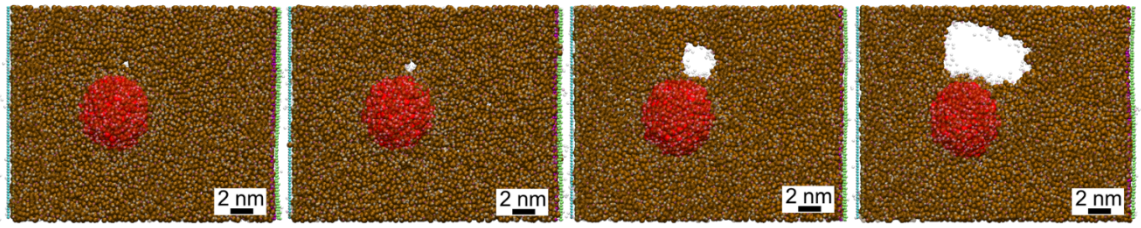

Figure 3.6 – Example of heterogeneous nucleation at a 3 nm spherical NP: (a) subcritical embryonic hole, (b) hole of nearly critical size of r_c=0.77 nm, (c) expanding overcritical hole, (d) large hole at the verge of membrane rupture. Lipid beads above NP are transparent

3.5 Conclusions

Overall, the agreement with the simulation data shown in Figure 3.2 confirms that the proposed model, despite of its simplistic 2D representation of NP-LB interface, captures the specifics of the heterogeneous hole nucleation and the mechanisms of rupture of NP-loaded membranes. The line tension, $\Gamma_{fs} = 39$ pN and dynamic pre-factor $A_{f,0} = 9.4 * 10^{18}/s$ for the homogeneous membrane. The contact angle, $\theta = 62^{o}$, for the three phase, lipid, solid, solvent boundary for the heterogeneous membrane. The dynamic pre-factor $A_{p,0} = 1.2 * 10^{13}/\mathrm{s}$ for spherical and $A_{p,0} = 4.5 * 10^{12}/\mathrm{s}$ for the cylinder. The calculated critical hole radius $r_c = 0.89$. The introduced contact angle provides a rational for quantitative assessments of NP-LB interactions. It can be estimated from the data of *in-silico* or *in-vitro* experiments on tension-driven membrane rupture based on the extended DG model presented here.

4 Nanoparticle Interactions with Supported Lipid Bilayers Using an Implicit Solvent Model

4.1 Background and Motivation

In recent years, supported lipid bilayers (SLBs) have generated research interest due to their applications in many areas.[146-150] They have been used as a simplified model to improve understanding of the properties and functions of biological membranes[148, 151] are used in experimental characterization techniques like NMR or FTIR,[152] for lateral diffusion measurements,[153] or for biosensing with NP-doped supported lipid bilayers (SLB)[154]. A thorough understanding of disjoining pressure, which mediates SLB interactions is necessary in order to understand how cells come in to contact and interact with each other. It has been shown that the disjoining pressure is a result of a hydration layer between the LB and the substrate[146, 149, 155, 156] Many experimental[157-167] and simulation studies[114, 168-172] have been conducted to understand this phenomenon . The disjoining pressure effect was quantified by Vishnyakov et. al.[114] with the help of atomistic molecular dynamics. A disjoining pressure isotherm, $\Pi(h)$, as a function of the separation between LB and hydroxylated amorphous silica was found. This isotherm has a double sigmoidal shape with two minima and one maximum corresponding to the limits of stability of the equilibrium states, Figure 4.1.

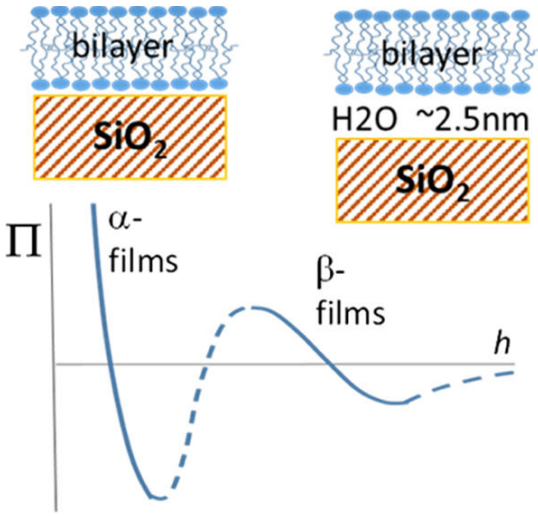

Figure 4.1 – Disjoining Pressure schematic. Top shown the α state (left) and β state (right). The corresponding pressure landscape is shown below.[114]

In α-state, when the LB is in close contact to the substrate, there exists an inhomogeneous distribution of water molecules trapped between the rough substrate surface and the LB. In β-state, the membrane is separated from the silica surface by the hydration film of ~2.5 nm in thickness that is stabilized by the specific interactions characteristic to thin water layers.

Though the understanding of SLBs is becoming clearer, nanoparticle (NPs) interactions with SLB is poorly understood. As NP use and manufacture becomes more common, understanding how they interact with cells is increasingly important. In atomic force microscopy studied Roiter et al.[173, 174] formed SLB on a silica substrate that was peppered with silica NPs observing three distinct states: if the NP was less than 1.2 nm in diameter, the LB bent over the NP and the LB was largely undisturbed; if the NP was 1.2-22 nm, the bending required by the LB was too extreme and a hole formed in the LB; and finally, if the NP was larger than 22 nm, the LB was able to envelope the NP, creating a continuous, but bumpy LB surface.

In order to study the NP-SLB interactions, a coarse-grained (CG) approach is needed as atomistic simulation are computationally prohibitively expensive. For example, Vishnyakov et. al.[114] were just able to model a LB with 92 lipids in the simulation box size of $5.21 \times 5.23 \times 19.08\ nm^3$, with the accessible time scale of 100 ns.[114] To simulate the larger systems that are necessary to observe the interaction of NPs with SLBs within larger scales, we employ implicit solvent (IS) CGMD method. In this method, solvent molecules are removed and an external force is introduced to compensate the solvent interactions. These interactions are incorporated using density-dependent potentials,[175, 176] angular dependent potentials,[177] Lennard-Jones tuned potentials[178] or modified Lennard-Jones potentials[179] between the lipid beads. In this work, we use the model proposed by Cooke et. al.[179] that was found to reproduce the properties of the DMPC membranes. The simulations were performed by a Masters student, Parva Patel, under my assistance.[180]

The main goals of this section are to understand the mechanism of interaction of 1) LB and the solid surface 2) LB with a hydrophilic surface with deposited hydrophilic and hydrophobic NPs. An original methodology based on an implicit solvent method that considers the effects of disjoining pressure between LB and hydrophilic surfaces Is developed. The disjoining pressure effects are modeled using a long-range potential that reproduces the disjoining pressure isotherm obtained from atomistic simulations. Using these tools, the LB interactions with surfaces containing hydrophilic and hydrophobic NPs of various sizes are studied. The long-range NP-LB-substrate interactions affect the SLB morphological changes, such as the pore formation and and stability of NP coatings. Finally, simulation results are compared with to the atomistic simulation work of Vishnykov et. al.[114] and the experimental work of Roiter et. al.[173, 174]

4.2 Models and Methods

4.2.1 Coarse-Grained Model

To accommodate the large system required for NP-SLB interactions, we implement an implicit solvent model. A force field is introduced in place of the solvent mediated interactions between lipid beads. The benefits of using an implicit solvent with respect to computational efficiency are two-fold. First, the solvent is removed which often composes 90%+ of all beads in the system. Second, as NP size increases, bead number only need increase quadratically, not cubically as in an explicit solvent system since beads are only added in the plane of the LB. This greatly reduces the computational cost of running a simulation. Cooke et al.[181,182] developed a simple implicit lipid model that represents a lipid as 3 beads – one head bead and two tails beads presented in Figure 4.2.

Figure 4.2– Pink is the head bead and blue are the tail beads

The nearest-neighbor bonds are described using the FENE potential

$$V_{bond}(r) = 0.5k_{bond}r_{\infty}^2 \log[1-(r/r_{\infty})^2];\ k_{bend} = 30\epsilon/\sigma^2\,; r_{\infty} = 1.5\sigma \tag{4.1}$$

Whereas a straightening bond between the head and terminal tail is given using a harmonic potential

$$V_{bend}(r) = 0.5k_{bend}(r-4\sigma)^2;\ k_{bend} = 10\epsilon/\sigma^2 \tag{4.2}$$

The interaction potential for the model is described in two parts. First, the repulsive part fixes the size of each bead with $r_c = 2^{1/6}b$.

$$V_{rep}(r,b) = \begin{cases} 4\epsilon[(b/r)^{12} - (b/r)^6 + 1/4] & \text{for } r \le r_c \\ 0 & \text{for } r > r_c \end{cases} \tag{4.3}$$

where $b = 0.95\sigma$ for head-head and head-tail, and $b = \sigma$ for tail tail. This is the complete description for the head-head and head-tail interaction potentials. To be clear, head-head and head-tail interactions are entirely repulsive. In addition to (4.3) the tail-tail interactions have an additional attractive potential

$$V_{att}(r) = \begin{cases} -\epsilon & \text{for } r < r_c \\ -\epsilon \cos^2[\pi(r - r_c)/2w_c] & \text{for } r_c \leq r \leq r_c + w_c \\ 0 & \text{for } r > r_c + w_c \end{cases} \tag{4.4}$$

The total tail-tail interaction potential is then exactly a Lennard-Jones to the minima, with an extended attractive potential of length w_c. A graph plotting the interaction potential is presented in the Figure 4.3.

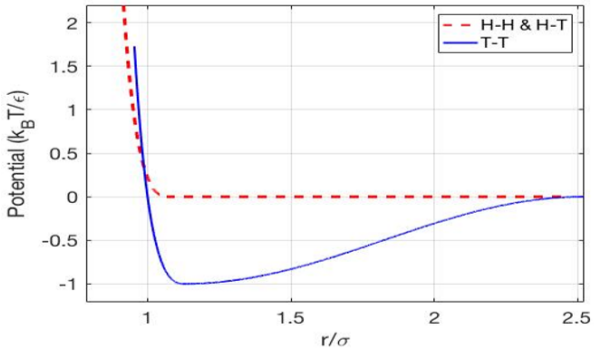

Figure 4.3 – Total interaction potential for H-H & H-T (red), and T-T (blue)

Both curves are continuous at all points. It is important to note that extending and tuning this attractive potential, the lipid diffusion rate and lipid order values agree with experiment.

4.2.2 Modeling a long-range potential to reproduce Disjoining Pressure Effects

While implicit solvent greatly decreases computational cost, some practical capitulations are made. Most relevant in the case of this study is the removal of the water molecules that cause a disjoining pressure (DJP). Accordingly, some external potential that

replicates DJP must be introduced, just as an additional attractive potential is added for tail-tail interactions in order consider the solvent mediated interactions that form a bilayer. To introduce the DJP, we first consider the interaction a single substrate bead has with the entire substrate at some distance, as illustrated in Figure 4.4.

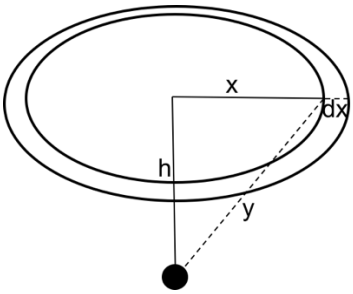

Figure 4.4– Interaction of a single substrate bead on a uniform surface at distance *h*

Taking the integral over the entire surface while considering both the lipid, ρ_l, and substrate, ρ_s, density:

$$V_{sl}(h) = \rho_s \int_0^\infty 2\pi\rho_l V_{bb}(h^2 + x^2)^{1/2}\mathrm{d}x = 2\pi\rho_s\rho_l \int_h^\infty yV(y)\mathrm{d}y \tag{4.5}$$

where V_{sl} is the total solvent-lipid disjoining potential and $V_{bb}(h)$ is the bead-bead disjoining potential. Noting that the disjoining pressure, $\Pi(z)$, is the derivative the solvent-lipid disjoining potential

$$V_{sl}(h) = \int_\infty^h \Pi(z)\mathrm{d}z \rightarrow \Pi(h) = \partial V_{sl}/\partial h = 2\pi\rho_s\rho_l h V_{bb}(h) \tag{4.6}$$

$$V_{bb}(h) = \Pi(h)/2\pi\rho_s\rho_l h \tag{4.7}$$

$$\partial V_{bb}(h)/\partial h = F_{bb}(h) = \big(h\,\partial\Pi(h)/\partial h - \Pi(h)\big)/2\pi\rho_s\rho_l h^2 \tag{4.8}$$

(4.7) and (4.8) are used to define interaction potentials input in LAMMPS. To calculate $V_{SB}(r)$ for the simulations, disjoining pressure values from atomistic MD simulations of Vishnyakov et. al.[114] are used. The pairwise interaction potential $V_{SB}(r)$ and force between substrate and lipid heads are shown in Figure 4.5. The pressure data point from

MD simulations are interpolated using the spline cubic fit, and the interpolated data is converted to the values of force and energy.

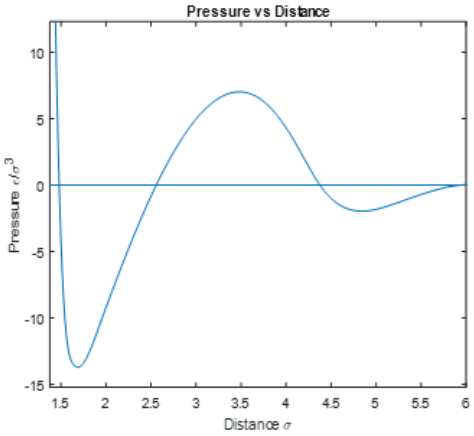

Figure 4.5 – a) Spline plot derived from the disjoining pressure value of Vishnyakov et al. b) Head-substrate potential which replicates disjoining pressure c) Forces derived from disjoining pressure potential

4.3 System Setup

The model is implemented using LAMMPS[183]. For verification of the disjoining pressure, no NP is needed, so the box size is relatively small. The box size is 16.5x16x17 σ *where* $\sigma = 1$ nm. The substrate spans the periodic box in the x and y directions and has a bead density of $1.15\ /\sigma^2$. 450 lipids compose the tensionless LB. At initial state, the lipids are placed within the system in a manner closely resembling a LB, as is done in the previous sections, and the system is allowed to equilibrate for 200,000 steps with a timestep of 0.005. A small external force is applied to all head beads proximal to the substrate for 200,000 steps. The external force is increased in small increments, holding constant at each value and the average separation between the head beads and substrate beads is measured.

The LB is placed between the two planks which is made up of 2 layer of beads arranged in the hcp lattice as illustrated in **Error! Reference source not found.**, right.

Using **Error! Reference source not found.** as a starting point, a hydrophobic substrate is added and the pulling plank height is extended preventing the LB from wrapping around the plank. The NP is placed on the surface of the substrate as illustrated in Figure 4.6.

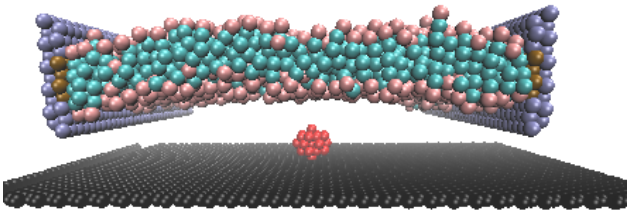

Figure 4.6 – Simulation setup illustrated an isotension LB as it approaches a hydrophobic substrate with surface NP

In this work we analyze the effects of various sizes of NP which can be characterized as small, medium and large particles.

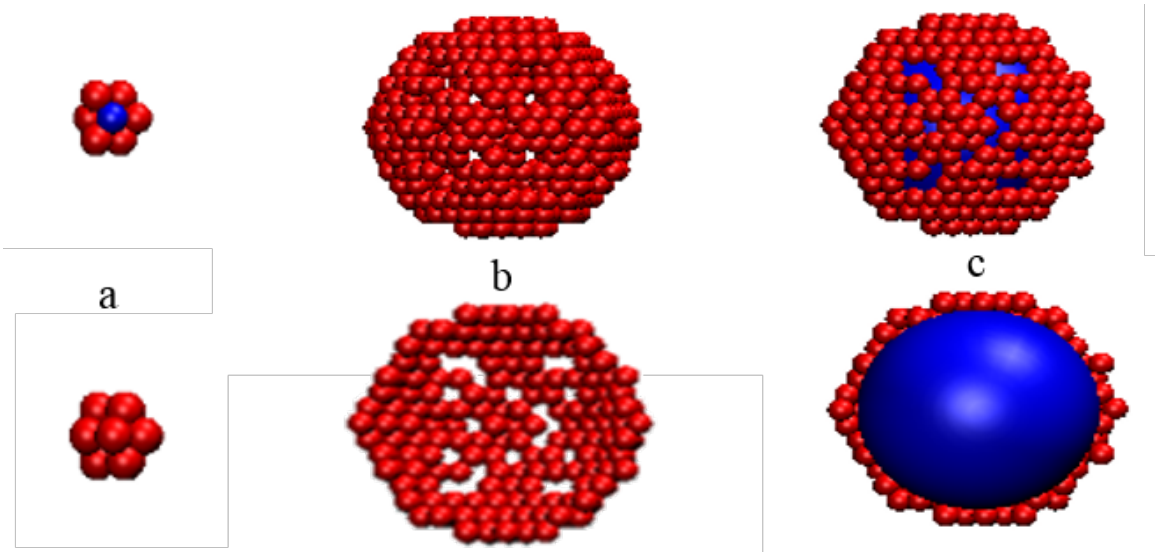

Figure 4.7 – Particle structure and cross-sectional view of 3 different NPs. Blue is the repulsive inner core and red is the NP shell (either hydrophobic or hydrophilic) a) 1.54 nm hydrophobic NP b) Large hydrophilic NP. Core beads are not necessary since disjoining pressure prevents penetration c) Large hydrophobic NP. Large core which prevents the lipids from entering the NP and saves computational time.

The smaller particles considered have diameters 1.54 nm, 3.08 nm, and 4.62 nm. The 1.54 nm NP consists of 13 beads (12 in the shell and 1 in the inner core). The 3.08

nm NP consist of 57 beads(38 in the shell and 19 in the inner core). The 4.62 nm NP consists of 159 beads (72 in the shell and 87 in the inner core). Large and medium sized nanoparticles are composed of beads in HCP lattice with a single large core bead that acts like a hardcore shell so no beads can penetrate inside. The hardcore shell effect is modelled using Weeks-Chandler-Andersen potential with $r_c = D_{NP}$. NPs of 9.24 nm, 15.4 nm, 23.1 nm, and 40.04 nm in diameter are studied. The 9.24 nm consists of 402 shell beads, 15.4 nm 1022 shell beads, 23.1 nm 2396 shell beads, and 40.04 nm 6924 shell beads.

4.3.1 Methodology

4.3.1.1 Interaction of LB with Silica Substrate

In order to validate the long-range pair potential to reproduce DJP, the LB-substrate system is studied in the absence of a NP. The LB is moved towards the substrate by applying a constant force to all head beads normal to the substrate. Note, when a constant force is applied to all lipid beads, the lipids flip, and tails face the substrate instead of the LB center. This happens because the pairwise disjoining pressure potential is only applied to head beads, so the head beads experience a repulsive force from the substrate, but tail beads do not. Force on the bottom heads is gradually increased their mean position at each force is calculated. From the force applied the position of LB position is obtained, the disjoining pressure is then calculated as a function of h.

4.3.1.2 $\boldsymbol{\beta}$-state Simulations

A NP is introduced to the substrate, with LB initially placed far from the substrate surface. No pairwise interaction between LB heads, NP, and substrate is imposed at this point. After the LB equilibrates, it is moved to the β-state by applying a very small force (0.001 ϵ/σ)

to all LB beads. The planks with are given a velocity towards the substrate, v_{plank} ($v_{plank} = 0.001\ \sigma/\tau$ for smaller particle and 0.0025-0.005 σ/τ for large particles). As the LB approaches the β-state, the constant velocity condition is removed. After the LB position stabilizes, all the external applied forces are removed, the planks are allowed to freely move normal to the substrate, and the LB finds its equilibrium position in the β-state.

4.3.1.3 α -state Simulations:

The bilayer in the α-state is simulated with a similar procedure, 4.3.1.2, but the disjoining pressure cutoff distance is temporarily shortened to 2.55 σ. This allows the large barrier to be overcome without causing the LB to break. After the LB reaches the α-state, the full disjoining pressure potential is applied. In this way, conformations of the LB in the α-state are explored. Note, the validation process for the substrate without the NP is carried out through a continuous increase in the force with no special treatment given at the point where the LB jumps from the β-state to the α-state, 4.4.

4.4 Results

4.4.1 Model Validation

Figure 4.8 illustrates the results of the of the DJP validation simulations. The procedure outlined in 4.3.1.1 is followed.

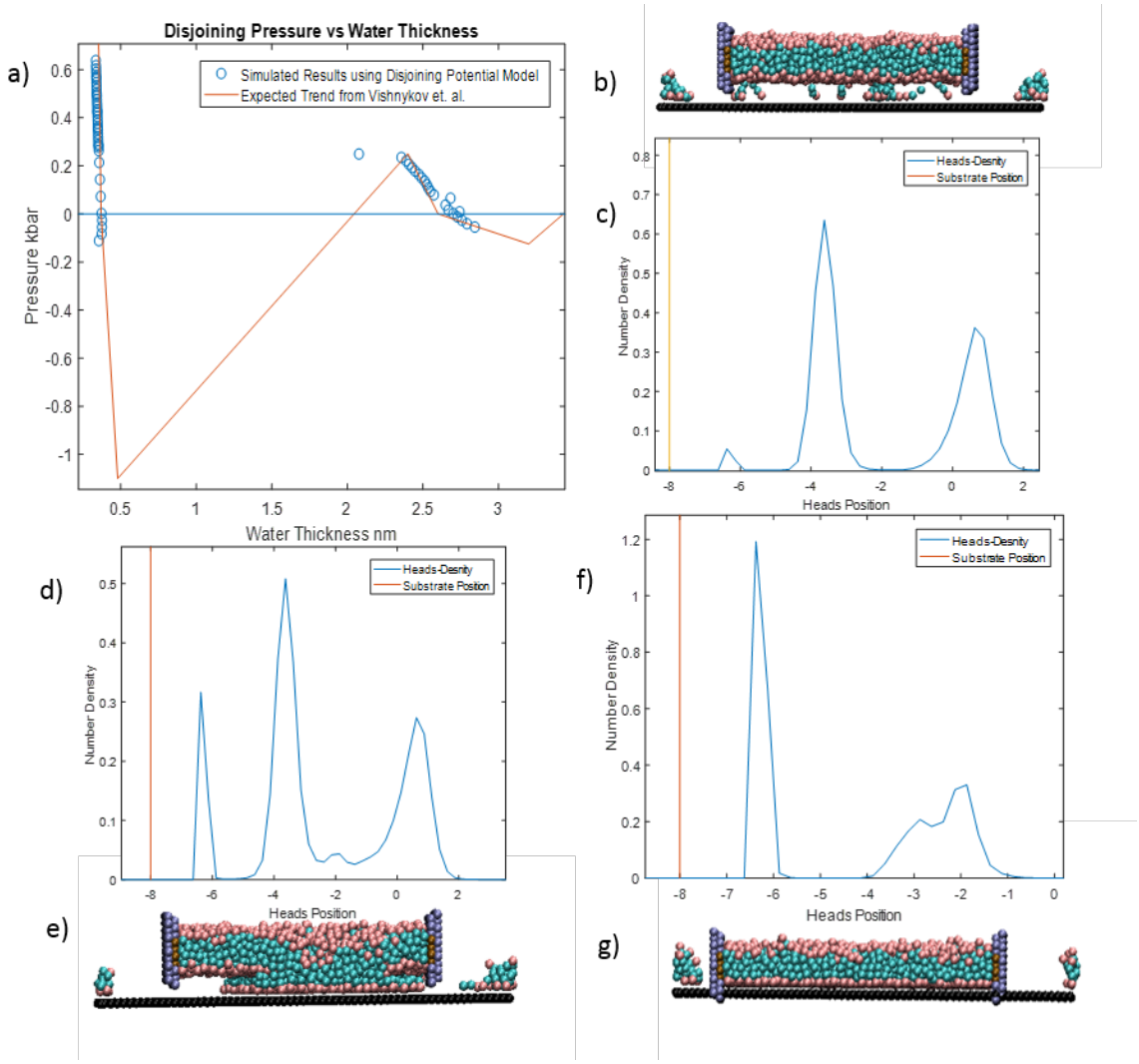

Figure 4.8 – a) Disjoining pressure landscape comparison between the atomistic simulations of Vishnyakov et al. [114] and the implicit DJP model. Snapshot and head density profile of the LB b-c) just prior to transition from the β-state to the α-state. d-e) transitioning into the α-state. f-e) in the α-state

The DJP values show very good agreement with the disjoining pressure landscape from Vishnykov et. al.[114] indicating the model reasonably reproduces the DJP from an explicity solvent system. In general, the head beads closest to the substrate has a narrower distribution due to the repulsion felt from the DJP that the top head beads do no feel. As force on the LB is increased, a few lipids have enough energy to overcome the maximum DJP in the β-state. These lipids are pulled out of the LB and jump toward the substrate

Figure 4.8 b). A pressure of ~0.26 kbar is required to overcome this barrier, close to 0.25 kbar obtained by Vishnykov et al.[114] Note, that the states with the negative values of the disjoining pressure correspond to experimental states that could be observed during the membrane detachment.

4.4.2 Interaction between SLB and hydrophilic NP in $\beta - state$:

For the smallest particle (1.54 nm) there is no effective interaction between the NP and LB. No pore formation or LB disturbance is observed allowing the LB to completely shroud the NP which can be seen from the Figure 4.9.

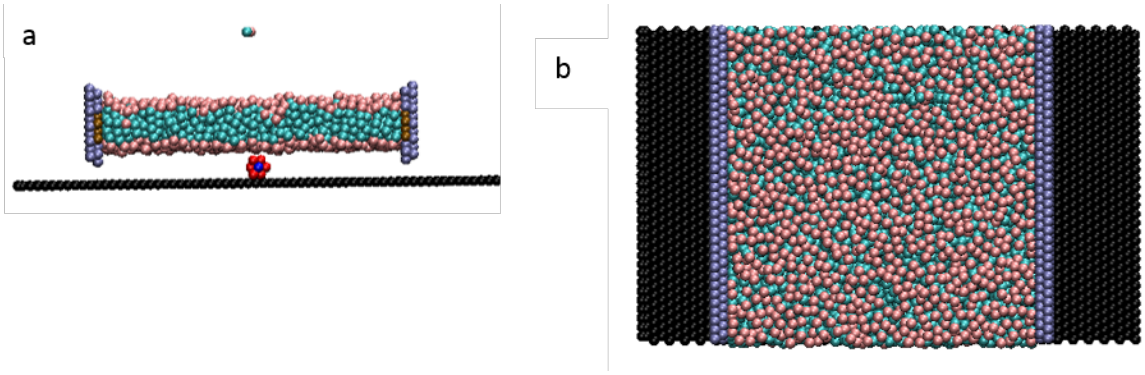

Figure 4.9 – NP-LB interaction with a 1.54 nm hydrophilic NP. a) Cross-sectional view with no apparent bulging of the LB b) Top-down view showing no pore formation in the LB

As the particle size is increased, pores in the membrane begin to form as a direct result of the disjoining pressure. This pore formation is illustrated in Figure 4.10 for the 5.39 nm NP.

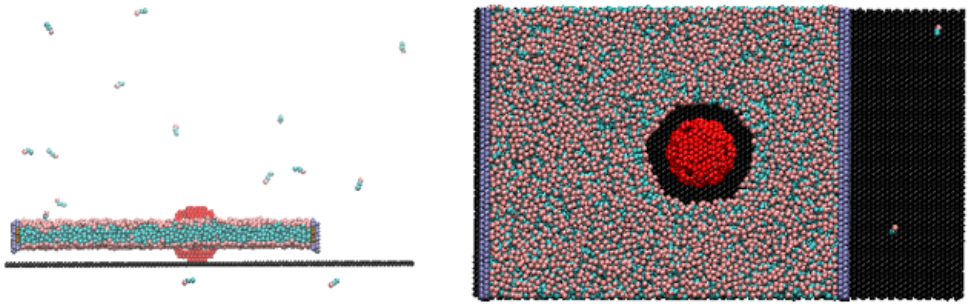

Figure 4.10 – Pore formation in a LB located in the β-state when a 5.39 nm NP is deposited on the substrate surface

Similar results are observed for NPs of size 10.01 nm and 15.4 nm. As the LB approaches the NP, a small pore opening near the NP-LB interaction appears. The DJP causes the LB to move towards the substrate until it reaches the β-state equilibrium position. During this process, the pore increases in size until equilibrated at with a diameter 2.6 nm larger than the NP.

For the 40.81 nm NP, the largest we simulate, the LB almost completely coats the NP with 70-85% coverage, as observed in Figure 4.11.

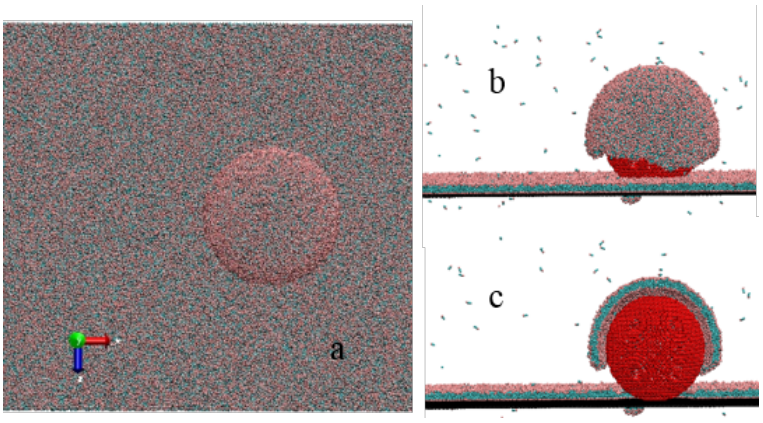

Figure 4.11 – LB coating of the 40.81 nm NP

From Figure 4.11, it appears that the LB completely blankets the NP. However, looking from the side, the LB that blankets the NP and the LB near the substrate do not connect. We suggest this is due to two possible reasons. The curvature that would occur to keep the

blanket connected to the rest of the LB would be extremely unstable structure. The second is due to a limitation of the lipid and DJP model. Because the lipid is only composed of three beads, it does not have the same flexibility that a real lipid would. Also, the DJP is developed for interactions between two flat surfaces, however, the NP is clearly not flat. Roiter et. al., also observe a discontinuity in the LB near the NP edge.

4.4.3 Interaction between SLB and hydrophilic NP in $\alpha - state$:

Simulations are also run for NPs of size 1.5, 2.31, 5.39, 10.01, 16.67, 23.87, 40.81 nm as describe in 4.3.1.3. For the 1.51 nm NP, the NP is too small to cause a pore to form in the LB, so the LB completely blankets it, as observed in Figure 4.12.

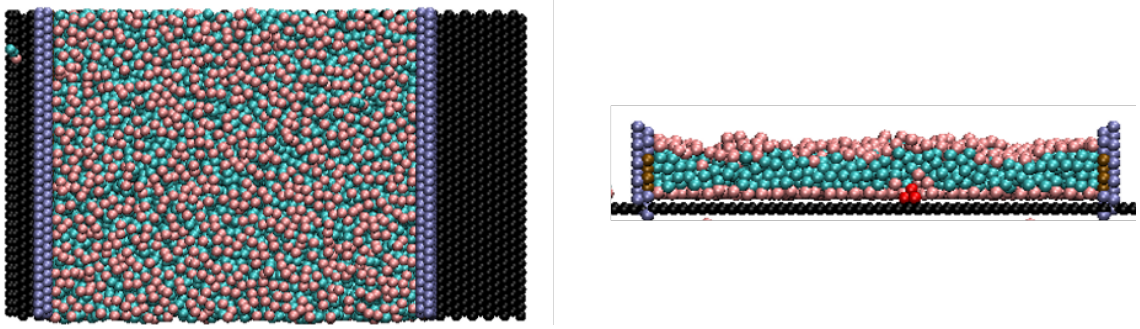

Figure 4.12 – Coating the of 1.51 nm NP with the LB in the α-state

Note how much closer the LB comes in to contact with the substrate. Just as with the β-state simulations, as NP size is increased, pores begin to form. However, the LB begins to blanket the NP at half the NP diameter when compared to the the β-state (10.01 nm

compared to 23.87 nm) as observed in Figure 4.13.

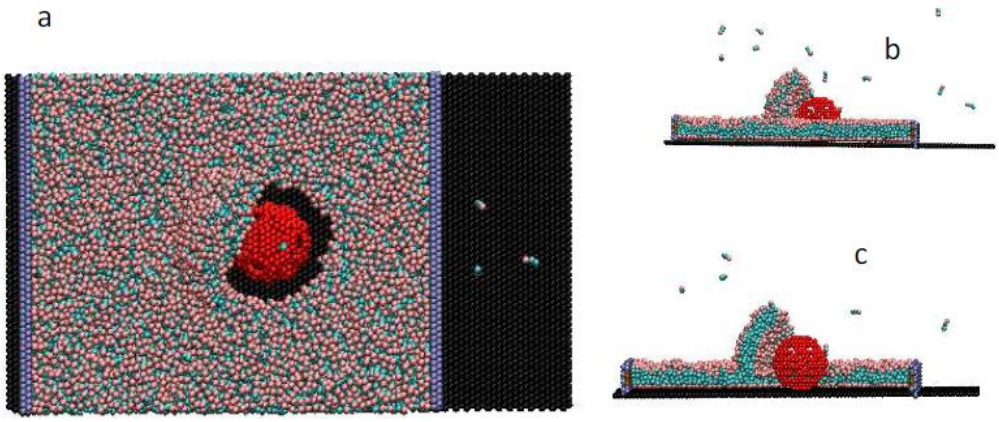

Figure 4.13 – Coating of the 10.01 nm NP with the LB in the α-state. Note the partial coating

4.5 Conclusions

In this chapter, a coarse-grained molecular dynamics (CGMD) with implicit solvent (IS) lipid bilayer (LB)is used to elucidate the stability of LBs supported on silica substrates decorated with hydrophilic NPs. We introduced novel features in the IS-CGMD set-up, which (a) secure the iso-tension membrane condition and (b) account for long-range lipid-substrate interactions due to the existence of the nanometer thick hydration layers between LB and silica. The latter effect is incorporated by using the effective long-range potential of interactions between lipid heads and silica mimicking the disjoining pressure developed in the hydration layer. The proposed IS-GCMD method allowed for simulation of large systems with up to 40 nm NPs and 80,000 lipids in the simulation cell of 231x154x77 nm in volume. In studies of interactions of LB with a plane silica surface, the IS-CGMD model is able to reproduce the predictions from atomistic MD simulations. Two distinct states are observed: α-states with the LB closely attached to the substrate and β-states with a nm thick hydration layer. This effect is accounted by introducing the

effective long-range potential that imitates the disjoining pressure in the hydration layer. For NPs less than 1.5 nm and greater than 24 nm, the NP is blanketed by the NP. For NPs in between these sizes, a pore is formed in the LB. These results agree with those of Roiter et al. This indicates the IS disjoining pressure model provides an alternative to explicit solvent simulations, allowing for much larger systems to be simulated than by standard methods.

5 Nanoparticle Flow in Polymer Grafted Channels

5.1 Background and Motivation

Santo et al.[15, 57] recently considered adhesion and separation of bare and functionalized NPs on polymer grafted substrates.[15, 57] It was shown that by varying the composition of the binary mixture of thermodynamically good and poor solvents, it is possible to control the PB conformation and regulate the conditions of solvent flow and NP adhesion. Using dissipative particle dynamics (DPD) simulations of slit-shaped channels, it was shown that solvent within the bulk of the PB is stagnant, and the solvent velocity in the central part of the channel outside the PB can be approximated by a parabolic Poiseuille profile with the diminishing velocity at the distance to the channel wall equaled the hydrodynamic width of PB, w_{PB},

$$u(z) = \frac{3}{2}\bar{u}_{slit}(1 - (z/(w - w_{PB}))^2), \tag{5.1}$$

where z is the coordinate across the channel with the origin in the channel center. The hydrodynamic width, w_{PB}, characterizes the extension of the PB and separates, using the chromatographic terminology, the mobile and stationary phases. w_{PB} depends on the solvent quality, PB density, and chain length. (5.1) implies that solvent flow in a PB-grafted channel of half-width, w, resembles solvent flow in the channel with hard walls of the effective half-width, w_H, reduced by the PB hydrodynamic thickness, $w_H = w - w_{PB}$. While modeling NP separation, the authors[15, 57] assumed that the NP has the same velocity as the solvent, and is immobile in the adhered state if it penetrates the PB within its hydrodynamic width ($w_H - R_{NP} < |z| < w$). When in the mobile state outside the PB at $|z| < w_H - R_{NP}$, the NP moves with velocity of the solvent. As such, the mean NP velocity and, respectively, the retention time in the mobile phase was calculated using

(1.1a) with $\lambda = R_{NP}/w_H$ and C=1 neglecting the specifics of NP motion in solvent flow. Investigating how the NP actually moves in this channel is an important next step.

In this chapter, NP flow in PB-grafted channels is studied using DPD, the coarse-grained method found efficient for modeling NP-PB systems in our earlier works[15, 57, 14, 184] as well as works of others is studied.[185-189] We consider two types of NPs, bare and functionalized by short chain ligands. We calculate the NP velocity profiles and conclude that, similarly to the solvent flow, NP flow in PB-grafted channels resembles NP flow in the hard wall channels of the effective size reduced by the hydrodynamic thickness of PB. This conclusion is confirmed by the experimental data of Staben & Davis.[67] We found that while for bare NPs, the mean NP velocity complies with (5.1a) with parameter C=2.5 in agreement with findings of Staben at al.,[66, 67] ligand-grafted NPs are characterized by a lower parameter, C=2.2. Our finds suggest a practical methodology of extension of the equations adopted in HDC on hard wall substrates to soft wall substrates – the effective channel size has to be reduced by the hydrodynamic thickness of the PB.

5.2 Computational Setup

We use the DPD model employed in our earlier works[15, 57] to simulate flow of bare and ligand-functionalized NPs of two different radii (2.84 and 5.68 nm) in a slit-shaped channel with PB-grafted walls. The ligands are represented by short chains composed of 6 beads each, which have the same interaction and bond parameters as the polymer brush beads. The simulation set-up with characteristic snapshots of the PB-grafted channel and NPs is presented in Figure 5.2. The PB forms a dense layer of the hydrodynamic thickness w_{PB} with a diffuse interface. Solvent moves under the action of a constant force applied to secure the constant volumetric solvent flux. The grafted ligands form a low-

density layer around the NP surface, effectively increasing their hydrodynamic size. For the sake of simplicity, the solvent, polymer chains, and NP are built of the beads of the same diameter, $R_c = 0.71$ nm, which represents the cut-off of the DPD repulsion potential. This size is determined based on the effective molecular volume of benzene, following the solvent parameterization of the previous work.[184]

In order to prevent any preferential adhesion or repulsion between the NP and PB, the DPD intra-component and inter-component repulsion parameters are taken equal to $a = 42\ k_B T/R_c$ for all the beads. This value corresponds to the DPD model of benzene, that is chosen to match the simulated and experimental compressibility of the solvent.[184] Excluding the channel walls, the system density is taken equal to 3 beads/R_c^3 that also corresponds to the density of liquid solvent (benzene) at ambient conditions.

Simulations are performed for NPs of two radii: $R_{NP} = 8R_c$ (2.84 nm) and $R_{NP} = 8R_c$ (5.68 nm). The NPs are composed of hexagonal packing lattice as illustrated in Figure 5.1**Error! Reference source not found.**. A set of simulations for a functionalized NP with ligand density of 0.6 ligands/nm^2 is also studied. The ligands are represented as 6-bead chains. The ligands are uniformly distributed over the NP surface bonded together in a linear fashion with K_i = 60 kT/R_c^2 and equilibrium bond distance of 0.8 R_c.

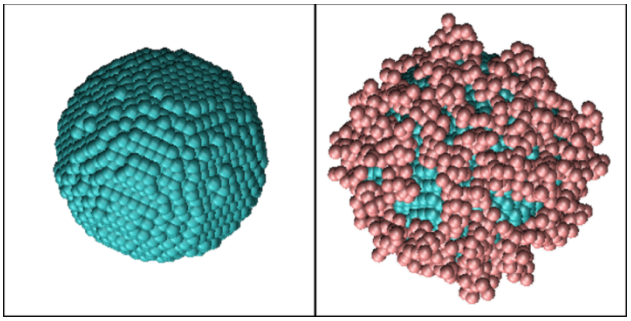

Figure 5.1 - Two different types of NPs studied. NP with a ligand coating of 0.6 ligands/nm^2 (left), and a bare NP (right).

The column wall also has the same lattice structure with a density of 12 beads/R_c^3 to prevent any penetration by the solvent. The lateral size of the simulation system, 28.4×28.4 nm^2 and 56.8×56.8 nm^2 for 2.84 nm and 5.68 nm NPs, respectively, is chosen to avoid the effects of periodic boundary conditions. Hydrodynamic channel halfwidth is varied from 3.7 to 57 nm to screen a wide range of scaling parameter, $\lambda = R_{NP}/w_H$ (from 0.1 to 0.75). The largest system considered contains 3,353,600 beads, to which Newton equations of motion are applied to monitor the system evolution to a steady state. The simulations start with a NP placed in the channel center, PB beads normal to the channel wall, and solvent beads placed randomly within the confines of the channel. The system setup is illustrated in Figure 5.2

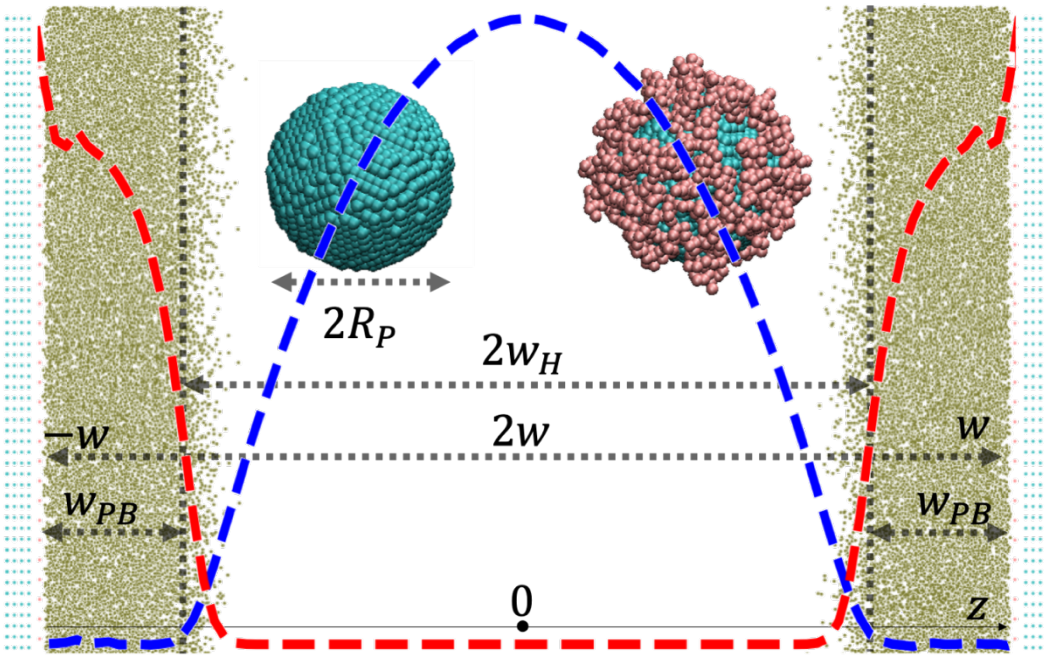

Figure 5.2 – Simulation set-up for modeling NP flow in PB-grafted channels. PB (green) is attached to the plain solid immobile substrate (light blue) with a certain density (here, 2.4 chains/nm^2, chains consist of 15 beads). Solvent not shown. PB density profile is shown in red. The solvent velocity profile (broken blue line) is approximated by a parabolic Poiseuille profile (5.1) with vanishing velocity at the distance to the wall equaled the hydrodynamic thickness, w_{PB}, of PB (vertical dotted black line, here, $w_{PB} =$ 6.2 nm).

A constant force is applied to all solvent particles to create a steady state flow. The system equilibrates under these conditions for 1 million steps with a with the timestep of 0.02τ, where $\tau \approx 50$ ps.[15] This corresponds to the simulation time of about 1 μs. The driving force is varied depending on the channel width to provide the maximum solvent velocity within $0.1\,R_c/\tau < u_{max} < 0.4\,R_c/\tau$. After the steady state is reached, in order to ensure sampling of the whole velocity profile across the channel, a set of parallel simulations is performed with the NP placed at different initial positions. The first 10% of the data gathering steps are ignored to ensure that the system reaches the steady state, then data is collected for the remaining 900,000 steps. Distance between initial NP positions depends on channel width, however the goal is to ensure the majority of the channel is explored, which is validated through observation of the results, as illustrated in Figure 5.3.

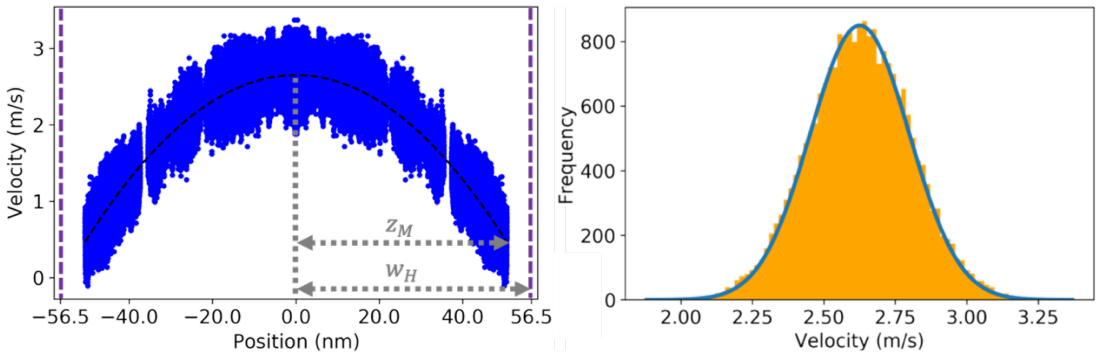

Figure 5.3 – Instantaneous NP velocity (blue) for the 5.68 nm NP in the channel of 62.7 nm, with the PB hydrodynamic width 6.2 nm, that corresponds to $\lambda = 0.1$. Black dashed line represents the parabolic approximation for the mean velocity (left). The distribution of instantaneous NP velocities is shown for the pore center ($\pm 0.5\ nm$) (right). The solid line corresponds to the expected Maxwell-Boltzmann distribution centered at the averaged NP velocity in the solvent flow.

As observed in Figure 5.3, the entire channel is explored. Note, because of the symmetry of the system, all data is reflected across the centerline to provide better statistics. The image provided represents 6.3 million individual data points.

Newton's equations of motion are solved using the Velocity-Verlet algorithm is employed in an *NVT*-ensemble. All simulations are run with LAMMPS[190] using the XSEDE Comet resource.[98].

5.3 Results and Discussion

5.3.1 Velocity Profile and NP Channel Exploration

For all systems studied, we confirmed the validity of the parabolic approximation **Error! Reference source not found.** for the solvent velocity.[15] We deal here with a good solvent, which penetrates into PB interior and remains stagnant within the distance of w_{PB} from the solid wall. Flow of solvent in PB-grafted channel of the width w is similar to that in a hard wall channel of the effective hydrodynamic radius (half-width) reduced by the hydrodynamic width of PB, $w_H = w - w_{PB}$. In the case shown in **Error! Reference source not found.**, $w_H = 27.9$ nm for the channel of $w = 34.1$ nm. The value of the hydrodynamic width of PB, w_{PB}, is determined from the fitting of the computed solvent flow profile to the Poiseuille parabolic approximation as the distance from the channel wall when the velocity vanishes. The PB hydrodynamic thickness, w_{PB}, increases with the increase of PB density and the chain length. For example, the PB hydrodynamic width equals $w_{PB} = 6.2$ nm at 2.4 chains/nm^2 and $w_{PB} = 3.3$ nm at 0.6 chains/nm^2 with same chain length of 15 beads//chain

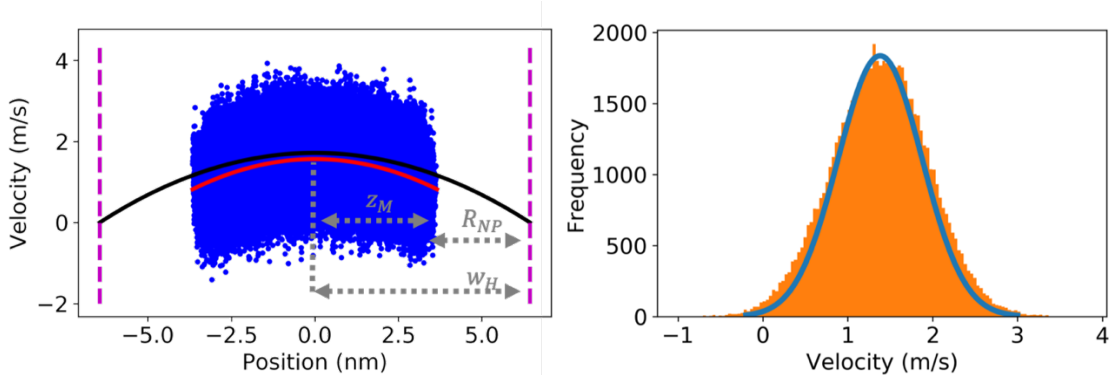

Figure 5.4 – Example of simulated NP velocity profile of 2.84 nm NP in the PB-grafted channel of hydrodynamic half-width of 6.46 nm (left). Blue points represent the instantaneous NP velocities samples along the simulation run. The black and red lines represent respectively the averaged solvent and NP velocity profiles fitted by the parabolic approximation. The purple dotted vertical lines mark the pore wall. The distribution of instantaneous NP velocities is shown for the pore center (right). The solid line corresponds to the expected Maxwell-Boltzmann distribution centered at the averaged NP velocity in the solvent flow.

5.3.2 Observed Velocities and Comparison with Experiments

Simulating the NP flow, we come to a similar conclusion that NP flow in soft-wall channel resembles the NP flow in a hard-wall channel with reduced, by the hydrodynamic width of PB, radius, $w_H = w - w_{PB}$. This is illustrated in Figure 5.4. The collection of blue points represents instantaneous velocities of NPs sampled in the course of DPD simulations. NPs are confined to the central mobile zone of the channel, expelled from the PB hydrodynamic boundary by its radius, Figure 5.4 (left). Due to Brownian diffusion induced by the pairwise Langevin thermostat, the thermal fluctuations of NP velocities are distributed with respect to the Boltzmann distribution centered around the mean NP velocity. Figure 5.4 (right) shows this distribution for the NP velocities sampled around the pore center. At the same time, the NP velocity, averaged along these fluctuations (depicted by the red line) is approximated by a parabola, which terminates at the boundary of the mobile zone z_M=$\pm(w_H - R_{NP})$ with a certain slip velocity. The

simulations show that NPs rotate in non-uniform solvent flow and lag behind the solvent. Of course, the PB surface is soft, so that NPs fluctuate and partially penetrate beyond the mobile zone boundary z_M. However, the analysis of the statistics of NP locations shows that the deviation between z_M and the farthest distances from the pore center achieved by NP due to radial diffusion is negligibly small.

As observed in Figure 5.4, the NP center of mass is excluded from the wall equal to its radius. This is an interesting result because, despite the channel thickness being defined by the average polymer brush thickness, the NP is excluded in the same manner as if it were a hard wall. However, the PB surface is soft, so that NPs fluctuate and partially penetrate beyond the mobile zone boundary z_M. To analyze the fluctuations of NP positions at the boundary of the PB, we collected statistics of the farthest distances, z_m, from the pore center achieved by the NP due to radial diffusion. The deviation of closest NP approach of a hard wall channel, $\Delta \mathrm{R_{HW}} = \mathrm{w_H} - (\mathrm{z_m} + \mathrm{R_{NP}})$ is averaged for all simulations of a certain type (bare and functionalized). In an ideal case of hard wall, $\Delta \mathrm{R_{HW}} = 0$, Figure 5.3, Figure 5.4.

For the bare NP, $\Delta R_{HW} = 0.04 \pm 0.31$ nm, where the error is the standard deviation. The results from the simulation indicate the NP-wall exclusion behaves similarly for both soft and hard walls. Carrying out the same calculation for the functionalized NPs, we found $\Delta R_{HW} = 1.18 \pm 0.55$ nm. This indicates the ligands increase the effective NP radius by 1.18 nm.

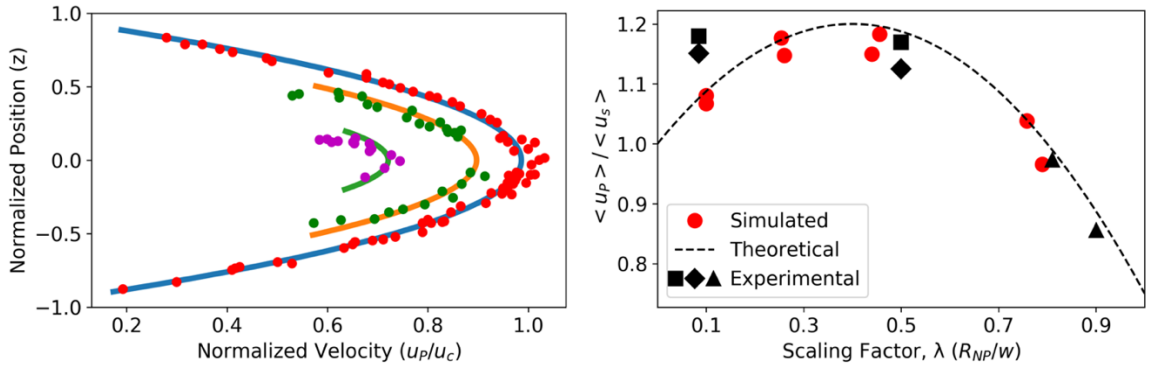

Figure 5.5 – Left: Simulated normalized NP velocity profiles for the scaling factors $\lambda = 0.1, 0.46, 0.76$ (blue, orange, and green lines, respectively). Experimental data as reported in Staben & Davis.[67] for $0.07 < \lambda < 0.1, 0.46 < \lambda < 0.54, 0.79 < \lambda < 0.84$ (red, green, and purple points respectively). Right: Comparison of the simulated and reported experimental data[28] for the reduced mean NP velocity. Red points represent the simulated results. Square points represent experimental data for the blunt channel entrance, diamond for the sloped channel entrance, and triangle for the average of the two.[67] Broken line – theoretical dependence of Staben et al. [27] approximated using Eq.1a with $C = 2.6$.

In Figure 5.5 (left), we compare the results of our simulations of NP flow in the systems with different scaling factors, $\lambda = R_{NP}/w_H$, with the experimental data of Staben et al.[67] on the particle flow in slit channels with hard walls. The data is presented in reduced units: velocities are normalized by the maximum solvent velocity in the pore center, and z-position across the channel is normalized by the halfwidth, w, of the channel with hard walls (experimental data) and by the hydrodynamic halfwidth, $w_H = w - w_{PB}$, (simulated data). Taking into account the huge difference of scales involved in simulations (NP size < 12 nm, channel width <120 nm) and experiments (NP size >36 μm, channel width >500 μm) the agreement is impressive. It shows that that this scaling works over 3 orders of magnitude, and thus, the results of simulations performed on the nanoscale level can be employed for making quantitative predictions for practical systems of significantly larger scales. This is specifically important for modeling

chromatographic columns with hierarchical pore structures ranging from tens of μm down to several nm.

Figure 5.5 (right) presents the simulated mean NP velocity across the PB-grafted channels normalized by the average solvent velocity as a function of the scaling factor, λ, in comparison with the experimental data and theoretical predictions (broken line) of Staben et al [66, 67] for hard-wall slit-shaped pores. This representation is useful for analyzing the chromatographic separation as the ratio of the mean velocities is reciprocal to the ratio of the respective retention times. Noteworthy, the data presented are reasonably approximated by (1.1a) with the parameter C=2.6, shown as the dotted black line. Apparent deviation of the experimental points from the theoretical curve at the smallest λ was explained by the authors[28] by the specifics of the channel entrance construction in their experimental setup. Agreement with the simulated data is within the accuracy of experimental data.

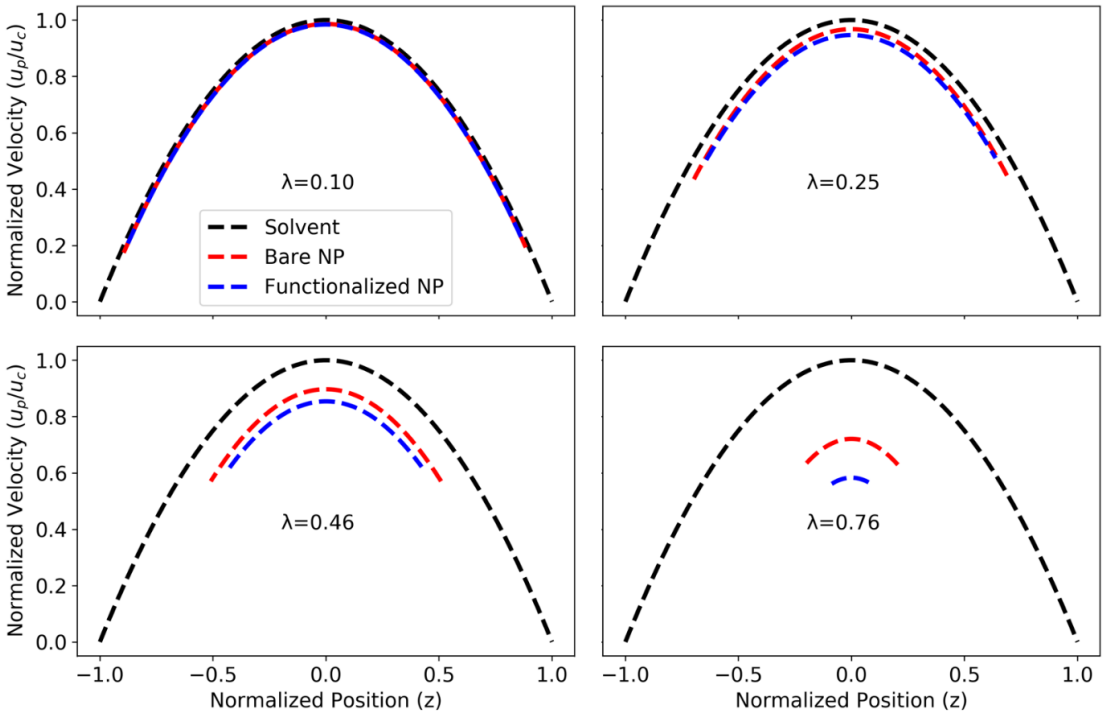

Figure 5.6 – Simulated velocity profiles for the solvent (black), bare NP (red), and functionalized NP (blue) for different values of the scaling factor λ. All velocities are normalized with respect to the maximum solvent velocity in the pore center.

Figure *5.6* presents the difference between the normalized (with respect to the maximum solvent velocity) velocity profiles for the solvent (black), bare NPs (red) and functionalized NPs (blue) for the systems with different values of λ. The NP velocities lag behind the solvent velocity profiles considerably as λ increases. When the size of the particles is an order of magnitude smaller than the channel size, $\lambda = 0.1$, all three velocity profiles fall nearly on top of each other. The similar velocity profiles indicate that small NPs move together with the solvent and the surface exclusion effect bares the first order contribution of λ into (1.1a). As λ increases, the distinction between the solvent and NP velocities become more and more apparent. The normalized velocity of ligand-functionalized NP is slower than that for the bare NP at the same value of λ due to the enhanced friction between grafted chains, PB and solvent, which intensifies NP

rotation. The effective radius of functionalized NPs is 1.18 nm larger than that of their bare counterparts. This fact causes a smaller width of the mobile zone sampled by functional NPs visible in **Figure *5.6***.

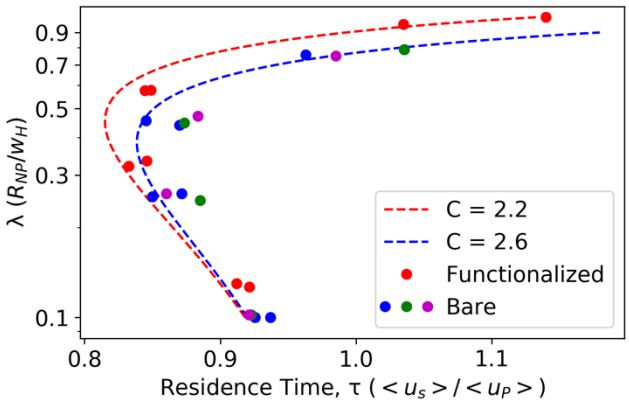

Figure 5.7 – Dependence of the reduced residence time on the scaling factor for bare and functionalized NPs. Lines represent the fit with (1.1a) with the parameter $C = 2.6$ for bare NPs and $C = 2.2$ for functionalized NPs. Simulated data are presented for two PB grafting densities of 2.4 (blue) and 0.6 chains/nm^2 (green) and hydrodynamic width of 6.2 and 3.3 nm, respectively, and PBs of different chain lengths at density 2.4 chains/nm^2. Channel width is varied to keep the ratio $w_{PB}: w = 1:3$, constant for all λ. At maximum $w = 60$ with $w_{PB} \approx 20$ and $w_H \approx 40$. At minimum, $w = 8$ with $w_{PB} \approx 2.7$ and $w_H \approx 5.3$

In Figure 5.7, the relationship between the NP residence time, τ and the scaling factor, λ is presented in the coordinates employed for analyses of the NP separations in HDC. The NP residence time,τ is given here in reduced units as the inverse of the mean NP velocity with respect to the mean solvent velocity. As observed in Figure 5.7, when λ is small, the residence time decreases as λ increases. This is due to the exclusion of the NP from the slower flow zone. However, as λ increases further, the residence time begins to increase due to the enhanced rotation as a result of the encroaching wall. While not

simulated, it is expected that as $\lambda \to 0$, the residence time asymptotically approaches 1. This is logical considering the solvent is effectively a very small sphere. Note that thus defined reduced NP residence time does not represent the ratio of the NP and solvent residence times, since the latter depends on the volume of immobile solvent retained in the PB, which is determined by the PB density and its hydrodynamic width. Instead, the relative time is calculated by integration of their respective velocity profiles. Taking Figure 4 as an example, the mean residence time of the solvent, $\langle u_s \rangle = \int_{-1}^{1} u_s(z)dz/2$, and the mean residence time of the NP, $\langle u_p \rangle = \int_{-(R_c-R_{NP})}^{R_c-R_{NP}} u_p(z)dz/2(R_c - R_{NP})$. The simulated data for bare NPs and different PB lengths and densities are reasonably approximated by Eq.1a with the same parameter $C \approx 2.6$ in agreement the theoretically prediction and experimentally observations[66, 67] shown in **Error! Reference source not found.**3. A smaller value of parameter $C \approx 2.2$ in the case of functionalized NPs is also in line with theoretical and experimental findings for soft polymeric particles.

5.4 Conclusions

In conclusion, we show that the NP flow in soft-wall polymer-grafted channels is similar to that in hard-wall channels of effective radius, reduced by the PB hydrodynamic width. Using the scaling factors, $\lambda = R_{NP}/w_H$, agreement is found between the simulated and experimental data for NPs and channels that differ in size by 3 orders of magnitude. This agreement confirms that the results of simulations can be used for modeling experimental systems of larger dimensions. The PB hydrodynamic width, which determines the boundary between mobile and stationary phases in polymer-grafted channels, is determined by the solvent quality and does not depend appreciably on the

channel shape and intensity of solvent flow.[15, 57] This independence suggests that the NP flow in polymer-grafted channels of other shapes (cylindrical, within packed bed and monolith columns) is similar to the NP flow of the hard-wall channels of effective radius reduced by the PB hydrodynamic width. This conclusion brings about an important practical recommendation: for modeling NP separation on polymer-grafted capillaries and columns grafted with polymers, one may use the models employed for hard-wall channels, like (1.1b), with the effective channel radius reduced by the PB hydrodynamic width.

6 GOALI INTERNSHIP a DuPont

6.1 GOALI Program and Project Background

From 09/01/2018 to 08/30/2019, I worked as an intern at DuPont under the guidance of Dr. Yefim Brun and funded by the NSF INTERN grant under the project titled GOALI: Theoretical Foundations of Interaction Nanoparticle Chromatography. This internship is aimed at graduate students who plan on finding a position in industry after graduation. This is a National Science Foundation funded internship with the goal of preparing the graduate student for a career in the engineering workforce. The specific goals of the internship project were learning and utilization of existing nanoparticle characterization techniques as well as developing novel approaches to chromatographic separations of polymer and nanoparticle (NP) dispersions, important in various industrial applications. Among the most important structural parameters affecting end-use properties of the polymer-nanoparticles formulations, are chemical composition, macromolecule/particle size and shape, molecular weight. Because samples are practically always polydisperse in most of these parameters, characterization is often associated with two processes – separation and detection. For NPs, the most important detection techniques are ones which quantify their size and shape of the particles. For this purpose, light scattering is the most suitable technique. Light scattering detection can be done 'offline' where nanoparticles are dissolved or suspended in solvent to measure the average properties of the sample.[191] Alternatively, measurements may be done 'online' where particles are first separated, e.g. by size and shape using an appropriate separation technique, following by the detection which allows for the measurement of the size and shape of macromolecules across their entire size distribution.[55]

To conduct the detection and separation experiments, I first needed to learn new for me experimental techniques. Among these techniques were sample preparation (i.e. preparation of stable nanoparticle dispersions) , high performance liquid chromatography (HPLC), dynamic light scattering (DLS) including depolarized dynamic light scattering (DDLS), and multi-angle static light scattering (MALS). Under supervision of professional lab occupants, I routinely ran arrays of experiments analyzing various nanoparticle sizes using HPLC in combination with in-line and off-line LS detection.

While in DuPont, I contributed in both aspects of nanoparticles characterization, i.e. made some improvement in existing data reduction approaches in characterization of geometry (shape) of non-spherical nanoparticles, and participated (both, theoretically and experimentally) in development of a novel "hybrid" chromatography technique for separation of nanoparticles and macromolecules with broad size distributions.

With respect to detection, I wrote several auxiliary programs for dynamic light scattering data treatment for a new light scattering device obtained from Light Scattering Instruments (Switzerland). The software was developed to measure length and diameter of cylindrical particles based on the work of Lima et al.[192] Since no commercially available software exists for this purpose, it is expected this will have a large impact within the characterization group at DuPont. With respect to separation, a new hybrid liquid chromatography (HLC) theory was suggested which was realized on commercially available silica monoliths. The model was experimentally verified with various polymer standards and applied to characterize complex polysaccharides such as starch. The HLC approach combines two size separation chromatographic techniques – hydrodynamic chromatography (HDC) and size-exclusion chromatography (SEC). The theory is verified

through experiments of various polymer standards on commercial available silica monolith columns.

Additionally, I conducted modeling studies to investigate how a soft column wall in a chromatographic channel, such as those in in the monolith columns, affect the standard theory for chromatographic separations.

6.2 Improvement of data reduction in DLS

As a part of a general task of characterizing nanoparticle materials, I worked on improving a commercial DLS data reduction package obtained from LS Instruments. DLS measures the scattered light with focusing on the small fluctuations of light emitted. These fluctuations can be autocorrelated, and the rate of decay of that function corresponds to the hydrodynamic size of the particle scattering light. DLS is a fast, integral measurement for particle size characterization, important in various fields from life sciences to catalysis. The instrument used for DLS is shown in **Figure 6.1**.

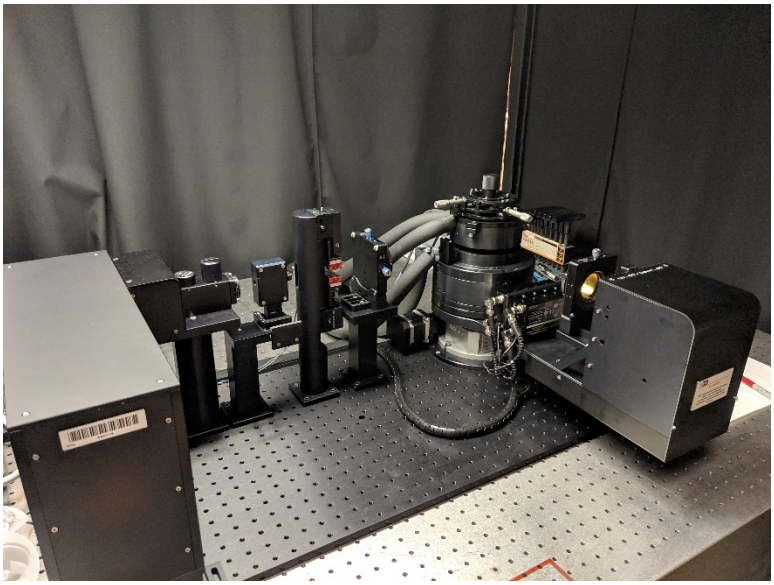

Figure 6.1 - 3D LS Spectrometer by LS Instruments, DuPont

I was tasked with two software development problems. The first feature adds a particle log normal distribution output. This type of distribution can be used to find the average particle diameter at various important points in the distribution. Adding this functionality presents the data into a format that customers are more accustomed to seeing allowing more actionable information regarding the tested samples. The second feature significantly increases the characterization capability of the software by introducing a module that employs depolarized DDLS to determine particle shape. This method measures scattered light through a depolarizing filter; since incoming light is polarized, only scattering from rotating anisotropy is measurement. Thus, the rotational diffusion coefficient can be measured. If knowledge of the general particle shape exists (e.g. from microscopy), a viscous force model can be applied to obtain size parameters.[192]

6.2.1 Results and Discussion

The first feature that was added to the LS instrument software was addition of a particle log normal distribution output. This type of distribution can be used to find the average particle diameter at various important points in the distribution. Adding this functionality presents the data into a format that customers are more accustomed to seeing allowing more actionable information regarding the tested samples. Such as distribution is shown in Figure 6.2.

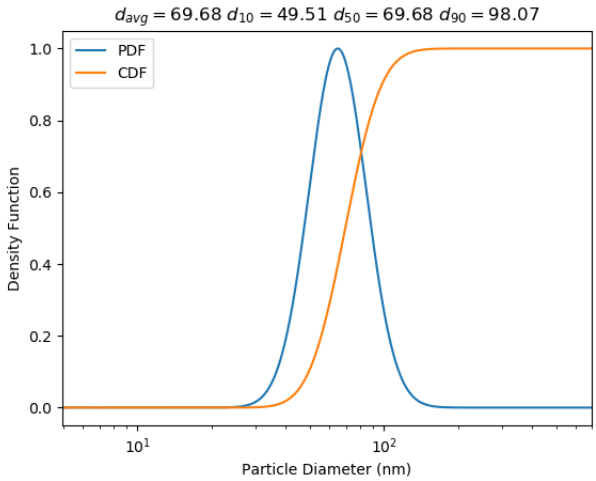

Figure 6.2 – A log normal distribution of a polystyrene standard created using the data reduction program I developed

Additionally, I added significant functionality to the characterization capability of the software by introducing a module that employs depolarized DDLS to determine particle shape. This method measures scattered light through a depolarizing filter; since incoming light is polarized, only scattering from rotating anisotropy is measurement. Thus, the rotational diffusion coefficient can be measured. If knowledge of the general particle shape exists (e.g. from microscopy), a viscous force model can be applied to obtain size parameters.[192] This was applied successfully to study size and morphology of microcrystalline cellulose whiskers dispersions used for viscosity modification of beverages. DDLS is consistent with findings from TEM, offering a fast, accurate

approach to measurement of rod-like particles in solution Figure 6.3.

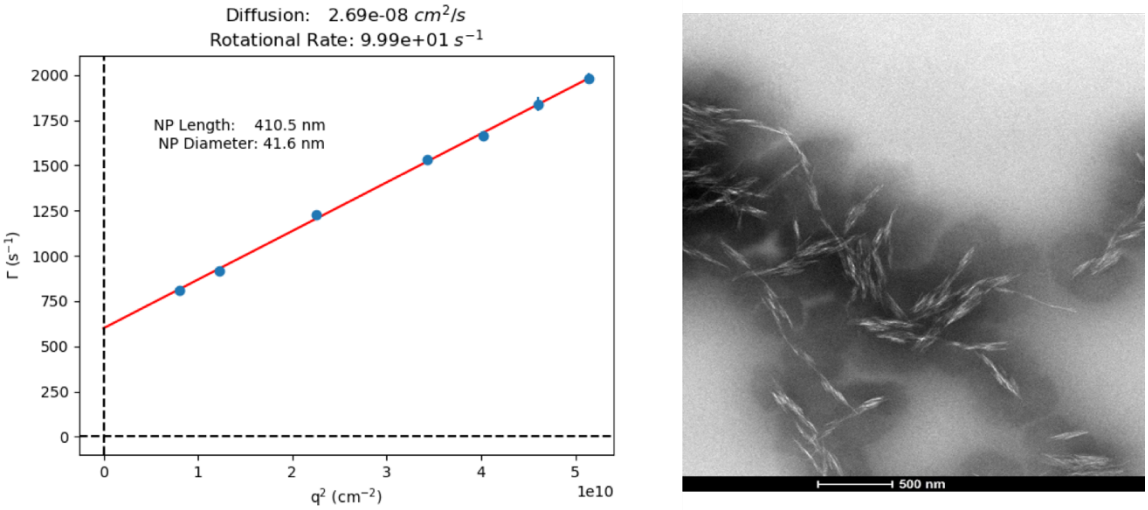

Figure 6.3 - (Left) Determination of length and diameter of a rod-like particle using multi-angle depolarized DLS, interpreted via custom software developed by the authors. Measurement is consistent with (right) TEM images of the same sample

6.3 Hybrid Liquid Chromatography Theory

A new hybrid liquid chromatography (HLC) theory is suggested which is realized on commercially available silica monolith. The model is used to characterize complex polysaccharides such as starch. The HLC approach combines two size separation chromatographic techniques – hydrodynamic chromatography (HDC) and size-exclusion chromatography (SEC). The theory is verified through experiments with various polymer standards on silica monolith columns, which allows the construction of column calibration curves. In order to construct such curve, a range of molecular weights for the three different polymers (pullulan, PMMA, and polystyrene) were dissolved in mobile phase. The data and resulting calibration curves for the monolith column is illustrated in Figure 6.4. This figure represents about thirty separate experiments.

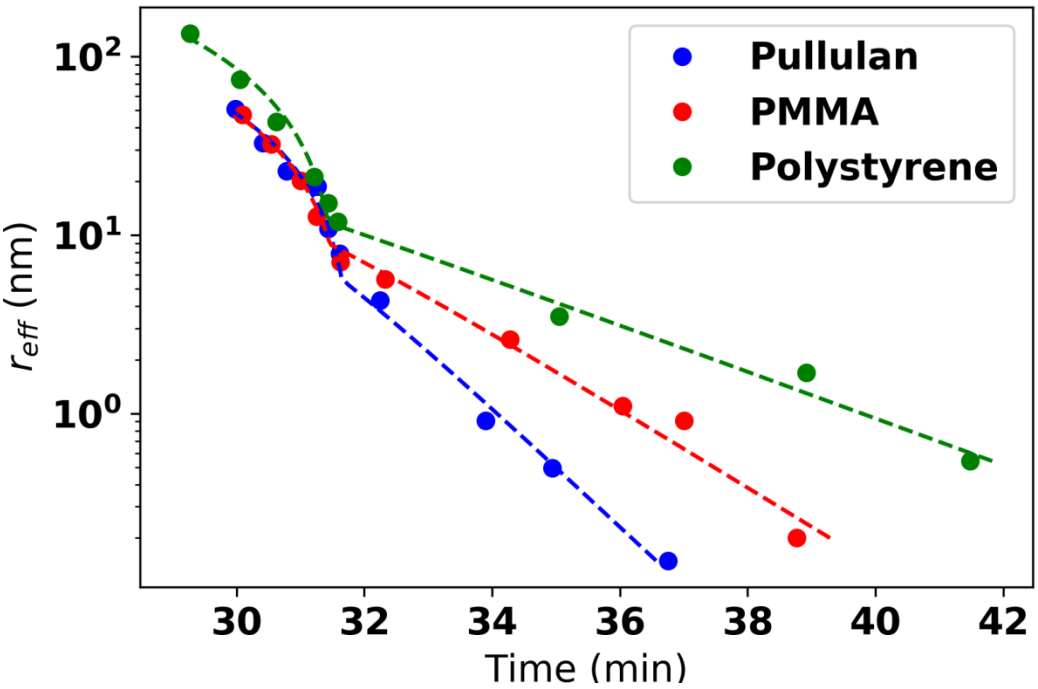

Figure 6.4 – Individual data points (circles), and calibration curves (dashed lines) for pullulan, PMMA, and polystyrene run through three monolith columns connected in series at a flow rate of 0.5 ml/min.

Because of the suggested theory, the parameters that are fit to the calibration curve provide structural details about the silica monolith column. The details, along with the vendor reported details, are presented in Table 6.1.

Table 6.1 - Resulting parameters for the column from the model and comparison with vendor reported values. Mesopore size is given as a range for the model because this value is sensitive to noise. The two mesopore sizes are calculated using the calibration curves from pullulan and PMMA.

Parameter	**Model**	**Vendor**
Channel Size	1.5 μm	1 μm
Mesopore Volume Fraction	0.128	0.1-0.15
Channel Volume	5.3 mL	5.78 - 6.12 mL
Mesopore Volume	0.78 mL	0.68 - 1.02 mL
Mesopore Size*	11.2 nm	13 nm

As is evident from the table, the model captures the column structure quite well. All calculated values (except for some deviation for channel volume) fall within the vendor reported values for this column.

Chapter 7 provides more details regarding the work on development of theory of HLC and its experimental verification.

6.4 Key Outcomes

As a direct result of this internship, I was offered and accepted a position as Post-Doctoral Fellow - Purification Development- Chromatography Modeling at Genentech. Additionally, two manuscripts are prepared for publication (one was already submitted and accepted) because of the support of this internship. Using dissipative particle dynamics, the first manuscript, Nanoparticle Flow in Polymer Grafted Channels, studies how polymer brush-grafted channel effects elution time of nanoparticles in solvent flow. The second manuscript, Hybrid Liquid Chromatography – Synergistic Effects of Hydrodynamic and Size-Exclusion Chromatography, proposes a new theory to describe elution time in real chromatographic systems. This study predominantly utilized experimental and computational resources provided by DuPont.

7 Hybrid Liquid Chromatography in Silica Monolith Columns

7.1 Background and Motivation

Separation of particulate matter (macromolecules and nanoparticles) by size is commonly used in both preparative (e.g. purification) and analytical goals.[55, 193, 194] Traditionally, there are two main methods to separate the particles by size: HDC[55] and SEC.[52] HDC separates particles by flow and is typically performed in columns packed with non-porous or porous beads. As a result of the irregular flow paths and pinch points that occur in the interstitial volume of packed columns, there is often a low mass recovery, which sometimes leads to completely plugged columns. This is particularly an issue with solid impenetrable solute like the majority of NPs because they cannot travel past the pinch points. Alternatively, HDC may be performed in long narrow dimeter tubing (capillaries), where the original theory was first developed.[63-65] While such capillaries have a much more regular structure than that of packed columns, and therefore do not easily become plugged, they have significantly less surface area per unit length. Therefore, extremely long columns and experiment times are required for separations with sufficient selectivity. Additionally, because there is only one path for an analyte to follow, capillary columns are easily overloaded so very low analyte concentrations must be injected in order to separate the sample, which leads to low detection sensitivity. In general, they are not compatible with modern separation techniques.[55] Like HDC, SEC also separates molecules by size, but through an entirely different mechanism. Similar to HDC, SEC is often performed in packed columns but always packed with porous beads. When a molecule enters one of the bead pores, it stagnates, effectively causing the molecules residence time (the time spent in the column)

to increase. The smaller a particle is, the easier it can enter a pore, and the longer it stagnates and larger its residence time. As molecule size increases, so does the probability its exclusion from the pores, effectively increasing the time spent in the hydrodynamic mode. In this work, a new hybrid liquid chromatography (HLC) theory is proposed which has implemented on commercially available silica monoliths. The HLC approach combines two size separation chromatographic techniques – hydrodynamic chromatography (HDC) and size-exclusion chromatography (SEC) and was verified through experiments of various polymer standards on silica monolith columns.

7.2 Theoretical Description of Hydrodynamic and Size-exclusion Chromatography

To create a HLC theory, the existing theories for HDC and SEC are first discussed separately. HDC theory was previously described in section 1.3. To reiterate the main point, elution time is predicted by (1.1) listed again here for clarity.[55]

$$\tau_{HDC} = \bar{u}_{solv}/\bar{u}_{NP} = (1 + 2\lambda - C\lambda^2)^{-1} \quad (7.1)$$

Here $\lambda = r/r_c$ and C is an adjustment factor. For colloidal dispersions of non-spherical particles or polymer chains in solutions, equation (7.1) is also used, but particle radius r is replaced with some effective polymer radius r_{eff}.[55]

As discussed previously, SEC, performed in packed or monolith columns, separates solute based on the amount of time the particle spends in a diffusional mesopore, where convection is absent and the molecule enters and exits the pore based on steric interactions. The existing mechanistic theory of SEC is quite complex and should take into account mesopore size distribution, specifics of steric interactions, effect of particle shape, column dimensions, among other structural and geometrical

characteristics. However, the practical outcome of size-exclusion separations is the linear dependence of the log of the hydrodynamic radius of the analyte as a function of elution time,[195] which is assume in our model.

As we mentioned above, HLC can be performed in columns packed with porous beads or monolith columns with bimodal pore-size distribution. In case the packed columns, hydrodynamic separation occurs in the interstitial volume of the beads, while size-exclusion occurs in beads' mesopores. In monolith columns, flow-through channels provide hydrodynamic separation, while diffusional pores – size exclusion. To the best of our knowledge, there were only two attempts to create a theory of HLC. The first attempt to create a HLC theory is the work by Stegeman et al.[196] To describe the hybrid separation process in a column, packed with porous beads, they arbitrary introduced a so-called 'polymer migration velocity', which they use as a measure of average velocity of particle migrating along the columns. Unfortunately, the authors failed to relate this quantity to any physical characteristics of the separation process such as polymer residence time or volumetric flow rate. For this reason, the authors come to the erroneous equation (7.2)

$$\tau = \tau_{HDC}\left[\frac{V_0}{V_0+V_i} + \frac{K_{SEC}V_i}{(V_0+V_i)(1-\lambda)^2}\right] \tag{7.2}$$

describing elution (residence) time τ of the macromolecule in the hybrid chromatography process. Here V_0 and V_i are the macropore and mesopore volume respectively, τ_{HDC} and λ are defined previously in (7.2), and K_{SEC} is a size exclusion coefficient which depends on the mesopore size distribution. Let us, for example, look at the elution time predicted by this equation in the case of mesopore volume much bigger relative to the channel volume. For $V_i \gg V_0$, equation (7.2) reduces to $\tau = \tau_{HDC}K_{SEC}/(1-\lambda)^2$. But it is obvious, that in

this limiting case, τ should not depend on interstitial volume V_0 at all, and one would expect $\tau = K_{SEC}V_i$. For example, when all mesopores are accessible ($K_{SEC} = 1$), elution time reduces to $\tau = V_i$ and not to $\tau = \tau_{HDC}/(1-\lambda)^2$, as predicted by equation (7.2).

Another attempt to develop a theory of hybrid chromatography on packed columns was undertaken by Guillaume et al.[197] They considered the particle separation process as an equilibrium exchange of these particles between two phases: size-exclusion mesopores and flow-through channels, but completely ignore separation within these phases. This means that the separation is a result of difference in relative time solute spends in two phases and no separation would be observed for particles within each phase, completely ignoring the separation by flow. In a such empirical approach, the elution volume (using the same notation as the authors), τ, of a particle inside the column is described by the equation

$$\tau = \xi\hat{\tau} + (1-\xi)\check{\tau} \tag{7.3}$$

Where $\xi(r)$ is molar fraction of the macromolecules inside flow-through channels, i.e. completely excluded from mesopores, and $\hat{\tau}$ and $\check{\tau}$ are relative retention volumes of particles spent all time in the flow-through channels, and particles that sample only the mesopore volume, respectively. These two relative retention volumes are considered as adjustable parameters and do not depend on particle size. For the "exchange" function $\xi(r)$, the following equation is suggetsted[197]

$$\xi(r) = \exp(\lambda_1 r - \beta)/(1 + 0.5\xi_c \exp(\lambda_1 r - \beta)), \tag{7.4}$$

which is defined as a sigmoidal function of particle radius r with an inflection point ξ_c as another system related adjustable parameter (λ_1 and β are additional independent of r adjustable parameters). Unfortunately, such definition does not adequately describe the

exchange between the phases, and therefore leads to erroneous results. Thus, by definition, for large r, $\xi \rightarrow 1$, as the majority of particles should be excluded from the mesopores. But from equation (7.4), $\xi \rightarrow 2\xi_c$., so that $\xi_c = 1/2$. However, based on the description of the authors, the adjustable parameter of ξ_c should be defined entirely based on the column structure, and not on particle radius, so that $\xi_c = 1/2$ for particles with all possible sizes. But this value contradicts to numbers found in the paper by fitting the experimental data for various chromatographic systems

To the best of our knowledge, there is only few published efforts to quantitatively describe separation of narrow polydispersity polystyrene standards in custom-made organic-based monolith columns using existing theory of hybrid chromatography.[58, 87, 88] Unfortunately, the authors of these publications applied the aforementioned theory of Stegeman et al.[196] to describe the hybrid separation. We propose a new physical model of hybrid chromatography which uses only easily measured physical parameters of the column, like channel and pore size and volume. This model is verified on commercially available silica-based monoliths (Merck Chromolith SemiPrep RP-18e 100-10mm). The feasibility of such column for separation of complex natural polymers is tested using natural starch as an example of polymer with very broad molar mass distribution. Such polysaccharide is not soluble in water, but soluble in polar organic solvents like dimethyl sulfoxide (DMSO) or dimethyl acetamide (DMAc) in presence of salt, e.g. LiCL.[198]

7.3 Theoretical Model for HLC

To develop the combined HDC-SEC mathematical model, we begin with a standard mass balance equation used to describe SEC separation in columns packed with porous beads, $V_r(r_{eff}) = V_0 + K_{SEC}V_i$.[199] In this model, $V_r(r_{eff})$ is the relative elution

volume for a particle with radius r_{eff}, V_0 is the total bead interstitial volume, V_i is the total mesopore volume inside beads, and K_{SEC} is a scaling factor that ranges from 0 to 1 . It represents the fraction of accessible pores and is a function of r_{eff}. $K_{SEC} = 1$ if the entire mesopore volume is accessible to the particle, and $K_{SEC} = 0$ if the particle is totally excluded from this volume. In the described model, both volumes V_0 and V_i are constants and do not depend on particle size. The same equation can be used also to describe the size exclusion separation on monolith columns, but the interstitial volume should be replaced by the volume of flow-through channels. When flow (hydrodynamic) separation between beads or in the flow-through channels is taken in considerations, then the dependence on particle size scaling factor K_{HDC} should also be introduced, i.e.

$$V_r(r_{eff}) = K_{HDC}V_0 + K_{SEC}V_i \tag{7.5}$$

Where K_{HDC} is simply $(1 + 2\lambda + C\lambda^2)^{-1}$ as described in (7.1)**.** As was mentioned above, the typical size-exclusion separation in both packed and monolithic columns is described by linear dependence of logarithm of the particle hydrodynamic size, r_{eff}, on elution volume[195], which is used in our model below.

Equation (7.5) reflects the physical foundation of the mathematical model which we use to describe the elution of particle and/or macromolecule with size r_{eff} in the monolith column, where separation by size occurs by two mechanisms: size-exclusion and hydrodynamic. More specifically, equation (7.5) can be written as a piecewise function

$$V_r(r_{eff}) =$$

$$\begin{cases} V_0(1+2\lambda-C\lambda^2)^{-1} & \text{if } r_{eff} > r_{max} \\ V_0(1+2\lambda-C\lambda^2)^{-1} + V_i \log(r_{max}/r_{eff})/\log(r_{max}/r_{min}) & \text{if } r_{min} \le r_{eff} \le r_{max} \\ V_0 + V_i & \text{if } r_{eff} < r_{min} \end{cases} \quad (7.6)$$

where r_{max} is the maximum mesopore size, r_{min} in the minimum mesopore size, and $\log(r_{max}/r_{min})$ is a normalization factor which ensures $0 \le K_{SEC} \le 1$. (7.6) assumes that particles with $r_{eff} > r_{max}$ are completely excluded from mesopores, i.e. $K_{SEC} = 0,$ and their separation occurs by flow only. At the same time, both hydrodynamic and size-exclusion separations occur if the effective molecule radius is less than maximum mesopore size, $0 < K_{SEC} < 1$, as such macromolecules constantly migrate between mesopores and flow-through channels. Finally, if the molecule is smaller than minimum mesopore size, it explores the entire column volume and elutes with solvent, i.e. $K_{SEC} = 1$.

Fitting parameters for this model are then V_0, V_i, r_c, r_{max}, and r_{min} . Contrary to earlier discussed empirical models of HLC, all parameters of our model have clear physical meaning and represent a geometrical structure of the column. In the subsequent discussion, experimental data obtained with 3 series of narrow polydispersity polymer standards to find these parameters by fitting with linear regression procedure is used, and then compare the fitted data with estimation of the same parameters from the independent experiments.

7.4 Experimental System

All chromatographic experiments were performed using Alliance™ 2695 Separation module from Waters Corporation (Milford, MA) coupled with 3 on-line

detectors: differential refractometer 2414 from Waters, multiangle light scattering photometer Dawn Heleos-II from Wyatt Technologies (Santa Barbara, CA) and ViscoStar-II differential viscometer from Wyatt. N,N'- Dimethyl Acetamide (DMAc) from J.T Baker, Phillipsburg, NJ with 0.11% LiCl (Aldrich, Milwaukee, WI) at 40^0 C was used as a mobile phase in all experiments. Two chromatographic software packages, Empower™ version 3, multidetector GPC option, from Waters and Astra version 7.3 from Wyatt, were used for data acquisition and reduction.

The SEC separations were performed on a set of four styrene-divinyl benzene columns from Shodex (Japan): two linear KD-806M, KD-802 and KD-801 at 0.5 ml/min flow rate. The size of each column was 300 x 8 mm ID with 10 um particle diameter. Hybrid chromatography experiments were performed at room temperature on a set of 3 semi-preparative silica-based Chromolith SemiPrep RP-18e monolith 100 x 10mm size columns from Merck (Germany) containing C_{18} bonded phase, at 0.5 ml/min flow rate.

Three sets of narrow polydispersity individual standards with molecular weights from several hundreds to several million Daltons, i.e. pullulan, polystyrene and polymethyl methacrylate (PMMA), were used for verification of the proposed theory of hybrid chromatography and column calibration. All standards, except for those with molecular weight exceeding 1 million Daltons, were prepared in the mobile phase solvent at concentration 1 mg/ml in 4-ml vials with mild agitation overnight, filtered through 200 nm PTFE membranes, and injected into the both chromatographic system with 100 µl (SEC) and 10 µl (hybrid chromatography) injections. PS and PMMA standards with molecular weight exceeding 1 million Daltons were prepared in the mobile phase solvent at concentration 0.1 mg/ml. All polysaccharides used in this research were dissolved at a

concentration 1 mg/ml in dimethyl sulfoxide (DMSO) with 2% LiCl at 80 ^{o}C for 4 hours, then kept at room temperature for 1 day with moderate agitation. 100 µl injections were used for the SEC experiments, and 10 µl for hybrid chromatography.

7.5 Results and Discussion

As was mentioned previously, a polar organic solvent DMAc was selected as a mobile phase for all hybrid chromatography experiments. This choice was caused by solubility of starch. To prove the existence of both modes of chromatographic separation (size exclusion and hydrodynamic), which is a prerequisite for hybrid chromatography, as well as for calculating geometric parameters of the proposed mathematical model (1.6), we needed a set of particles/polymers ("standards") with similar chemical structures but a broad range of sizes (molecular weights) covering both modes of the chromatographic separations. The necessary conditions for such standards is separation by size without any non-size-exclusion effects, e.g. adsorption. We tried three series of commercially available with a broad range of molecular weights narrow polydispersity polymer standards with different chemistries, i.e. polystyrene, PMMA and polysaccharide pullulan, all soluble in DMAc. These standards are listed in Table 1.1, with weight average molecular weights provided by the vendors. The standards were individually dissolved in the mobile phase solution run through both SEC and monolith columns. Using triple detection SEC system, equipped with on-line differential refractometer, multiangle light scattering photometer and capillary differential viscometer, we confirmed the reported M_w-values (within 3%), as well as calculated radius of gyration, r_g, and intrinsic viscosity $[\eta]$ for each standard. All calculations were made using

commercial Astra 7.3 chromatographic software per the procedure described in ref[200] Effective (hydrodynamic) radius r_{eff} for each standard was calculated using equation[200]

$$r_{eff} = (3H/10\pi N_A)^{1/3\ 3} \quad (7.7)$$

where hydrodynamic volume $H = [\eta]M_w$ and N_A is Avogadro's number. Molecular weights, radius of gyrations, and effective radii for all standards are shown in Table 7.1.

Table 7.1 – Weight-average molecular weight (M_w), radius of gyration (r_g), and effective (hydrodynamic) radius (r_{eff}) for all polymer standards tested

Pullulan			Polystyrene			PMMA		
M_w (kDa)	r_g (nm)	r_{eff} (nm)	M_w (kDa)	r_g (nm)	r_{eff} (nm)	M_w (kDa)	r_g (nm)	r_{eff} (nm)
0.04		0.13	1.4		0.54	1.3		1.1
0.5		0.49	8.7		1.69	6.4		2.6
1.3		0.91	28.0		3.51	20.4	6.4	5.7
14.6		4.3	173.1	13.4	11.9	50.0	8.0	7.1
37.7		7.9	250.6	17.0	15.1	152.4	14.3	12.7
61.7		10.8	424.8	24.0	21.3	305.1	22.7	20.1
116.4	21.1	18.7	1285.6	48.6	43.1	657.2	36.5	32.3
201.9	25.7	22.8	3020.7	83.6	74.1	1172.9	53.4	47.3
334.1	37.2	33.0	7427.0	151.9	134.6			
582.6	57.3	50.8						

It should be noticed that the radius of gyration values for lower molecular standards are absent from the table by the following reason. The values are calculated using standard static light scattering (SLS) techniques as described by Nordemeier.[201] Such calculations require measuring the change in light intensity at varying detector angles. However, when a polymer is too small, it is a point scatterer so reflected light is a constant with respect to detector angle preventing r_g from being obtained. This is evident in Table 7.1 as only larger polymers have a corresponding r_g value. Using the same experimental data, we were able for the first time determine the scaling parameters A and α for all three set of

standards in DMAc for the exponential relationship $r_g = AM^{\alpha}$, frequently used in literature.[202] A is 0.87, 0.49, 1.08 and α is 0.64, 0.62, and 0.54 for pullulan, PS, and PMMA respectively. Parameter values are calculated from the scaling observed for the larger polymers. That is, a r_g is plotted as a function of M_w, and a best fit curve of form $r_g = AM^{\alpha}$ is found.

The same three sets of standards were run also on the set of monolith columns. The corresponding refractometer chromatograms are shown in Figure 7.1, Figure 7.2, Figure 7.3.

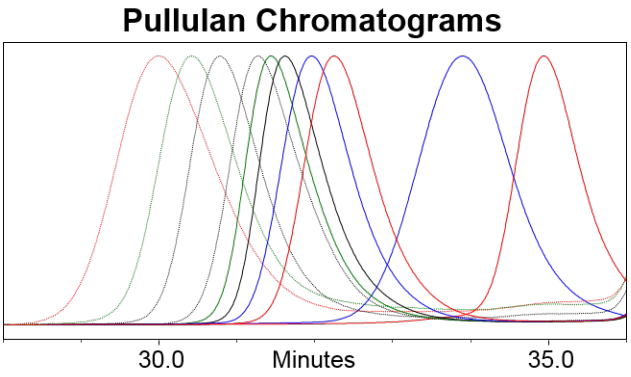

Figure 7.1 – Chromatograms for pullulan standards. By peak, from left to right the standards have a molecular weight of (units in kDa): 708, 337, 194, 107, 50, 24.5, 6.2, 1.08, 0.342. The salt peak (36 min, not shown) elutes just after the 0.342 kDa pullulan

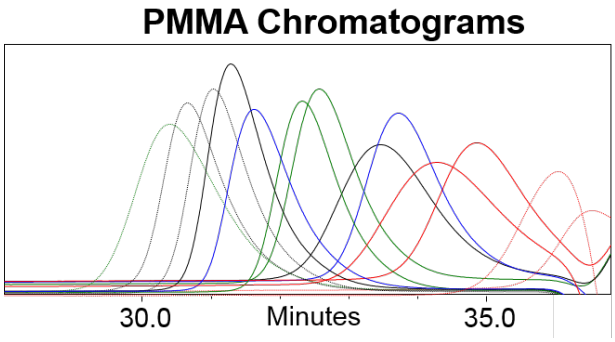

Figure 7.2 – Chromatograms for PMMA standards. By peak, from left to right the standards have a molecular weight of (units in kDa): 1600, 845, 364.9, 185, 64, 24.83, 7.8, 2.4. The right-most peak is the salt peak.

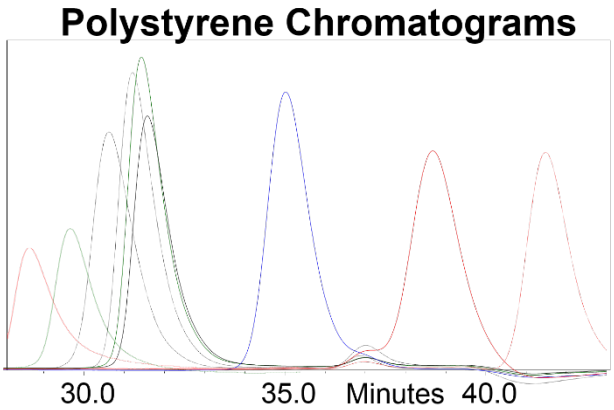

Figure 7.3 – Chromatograms for PS standards. By peak, from left to right the standards have a molecular weight of (units in kDa): 8000, 3150, 1460, 500, 283.3, 185.4, 30, 1.26

We analyzed these chromatograms for the evidence of non-size-exclusion separation. As one can see from the retention time, a significant difference is observed between for the three polymers in the lower molecular weight (size-exclusion) region. Thus, only in pullulan series, shown at Figure 7.1, the salt (LiCl) peak (37 min retention time) elutes after all standards including the one with the lowest molecular weight 342 Da. This salt peak indicates so called system peak (i.e. peak corresponding the entire pore volume of the columns) and should follow all polymer standards partially or completely excluded from the diffusional pores in case of ideal size-exclusion separation. In case of PMMA (Figure 7.2), the lowest MW polymer elutes after the salt peak, while for polystyrenes (Figure 7.3). not only lowest MW elutes after the salt peak, but so do even higher molecular weight standards. We attribute this to the effect of adsorption of the polymers dissolved in polar organic solvent to the non-polar C_{18} oligomeric chains grafted on the porous surface of the monolith. The most non-polar polystyrene appears to be most strongly adsorbed to these chains, followed by more polar PMMA, and then the

most polar pullulan, which appeared to be eluting in size-exclusion mode without any adsorption interaction.

The observations are confirmed by corresponding elution profiles (sometimes called calibration curves) shown at Figure 7.4. At this figure, effective (hydrodynamic) radii, $r_{eff.}$ for each standard from Table 7.1 are plotted as a function of peak elution time from the corresponding chromatograms at Figure 7.1, Figure 7.2, Figure 7.3. LiCl salt peak elution point was added to the pullulan calibration in Figure 7.4, while for PMMA, acetonitrile is chosen as a small molecule that would elute along the PMMA calibration curve, representing similar chemical structure and polarity to PMMA. This is used as the last point on the calibration curve for PMMA in Figure 7.4.

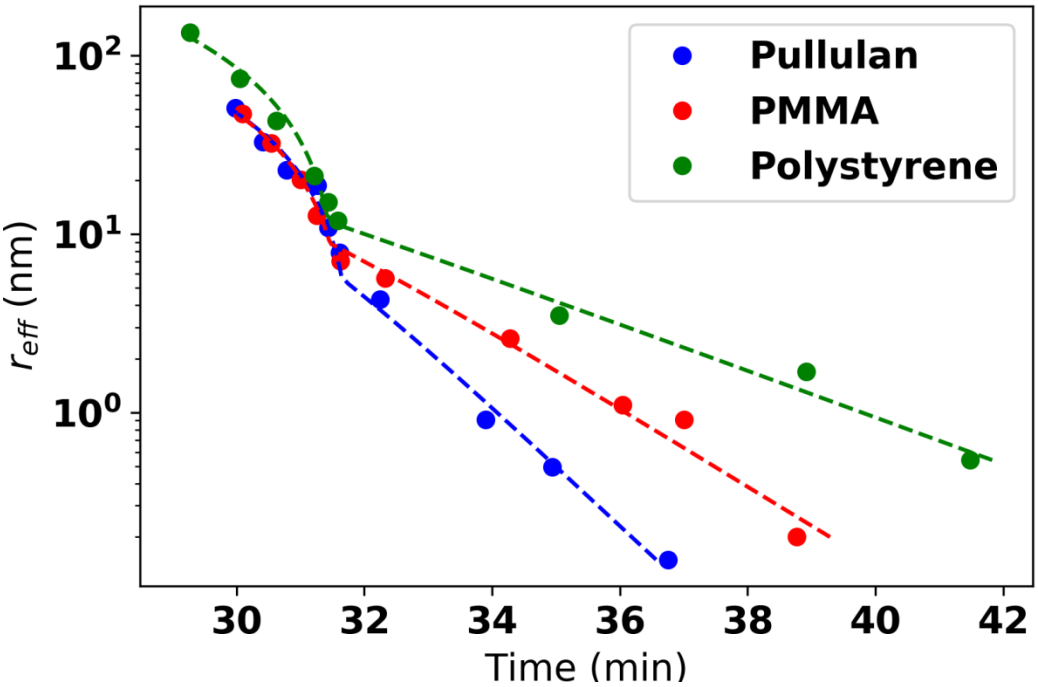

Figure 7.4 – Individual data points (circles), and calibration curves (dashed lines) for pullulan (blue), PMMA (red), and polystyrene (green) run through three monolith columns connected in series at a flow rate of 0.5 ml/min.

Each of the calibration curves in Figure 7.4 clearly shows two characteristic regions with different slopes and transition point close to 32 min. Such shape of calibration curves indicates two different mechanisms of retention, i.e. hybrid separation. As has been shown for SEC[22] and HDC[2,9], hydrodynamic size is a control parameter of the separation in each regime, as soon as non-size exclusion effects (like adsorption) are absent. In other words, in case of ideal hybrid separation, all three curves should coincide with each other. But it is obvious from Figure 7.4, all three curves in SEC region are significantly separated from each other, indicating a strong adsorption of both polystyrene and PMMA. At the same time, the calibration curves for pullulan and PMMA in the HDC region appear to lie right on top of each other, and only polystyrenes curves still deviate in direction of stronger retention. Assuming the difference in retention times is due to interaction between the C_{18} oligomers and analyte, the smaller difference between the corresponding polymers in the HDC mode compared to the SEC regime, indicates fewer accessible C_{18} chains within the channels. It is to be expected that the adsorption effect would be more pronounced in the mesopores considering they have significantly higher specific surface area than the macropores (flow-through channels).

Based on this analysis, we concluded that pullulan is the only polymer that does not have any affinity to the C_{18} chains, and selected its elution profile in Figure 7.4 to fit model. The data is to (7.6) using a non-linear regression code written in Python. Residuals between all points are weighted evenly. The results from the model fit are presented in Table 7.2 and compared against vendor reported values. A discussion of how vendor values are calculated follow.

Table 7.2 - Resulting parameters for the silica monolith column from the model and comparison with vendor reported values.

Parameter	Model	Vendor
Mesopore Channel Radius ($\boldsymbol{\lambda(r_c, r_{eff})}$)	1.5 μm	1 μm
Mesopore Volume Fraction ($\boldsymbol{V_i/(V_i + V_0)}$)	0.13	0.1-0.15
Channel Volume ($\boldsymbol{V_0}$)	5.3 mL	5.78 - 6.12 mL
Mesopore Volume ($\boldsymbol{V_i}$)	0.78 mL	0.68 - 1.02 mL
Mesopore Size*	11 nm	13 nm

As is evident from the table, the model captures the column structure quite well. All calculated values, except for channel volume and mesopore size, fall within the vendor reported values for this column. It should be noted mesopore size is very sensitive to statistical noise. This is because this term describes the point when the HDC and SEC curves meet. A very small change the other 4 parameters may cause a large change in the mesopore size. The method the vendor uses to calculate mesopore size is similar and also sensitive to error, as described below.[203]

Column structure may be calculated using a handful of techniques including inverse size exclusion chromatography (ISEC), transmission electron microscopy, mercury porosimetry, and nitrogen sorption as described by Lubda et al.[83] The vendor reported values are calculated using ISEC.[204] This method is similar to the method discussed in this chapter. A polymer with varying molecular weights is run through the column and elution time is measured. In this method, molecular size as a function of elution volume is plotted. The graph looks similar in that there are two distinct regions.

Both slopes are assumed to be log-linear, which is different from how we treat the data. The total pore volume ($V_0 + V_i$) is the retention volume of a small molecule, in this case, toluene. The macropore volume (V_0) is calculated using the point where the two log-linear lines intersect.

Finally, the mesopore volume is calculated as total pore volume minus macropore volume. From Table 7.2, the largest observed difference is between the mesopore channel radius values. In order to calculate mesopore channel radius, previous works, including the method used by the vendor, use an approximation relating monolith columns to packed columns. In a packed column, there is a relationship between the 'effective channel size' and the packed bead diameter. There is a second relationship which relates bead diameter to hydraulic resistance. Therefore, the assumption made for ISEC to calculate mesopore channel size in monolithic columns is to use the described relationship backwards – the hydraulic resistance is related to some channel size.[203] For example, a column similar to the one used in the present study is stated by Al-Bokari et al.[203] to have the same hydraulic resistance as a column packed with 11 μm spherical particles. Using $r_c = \sqrt{8k_0}d_p$ where k_0 is the permeability coefficient, assumed to equal 0.001, and d_p is the particle diameter, $2r_c = 2\ \mu m$ for a column packed with 11 μm spherical particles. However, since this relationship is first developed for packed columns, there likely is some error in the calculation. The method used by the authors of the present study makes no such assumption and uses HDC theory (7.1) to calculate mesopore radius. We suggest this is a more reliable description of the real mesopore size.

Separation on silica monolith columns are also performed for a potato starch sample because of starch's binary composition. Potato starch is composed of 20-30%

amylose, a linear polysaccharide with radius 7-22 nm.[205] The remaining composition is amylopectin, a large hyperbranched polysaccharide, representing even in solution by soft particles with size exceeding hundreds nanometers and molecular weight of 10^6-10^9 Da. The macromolecules of amylopectin are susceptible to shear-based decompositions at high pressures.[205] This binary composition – lower molecular weight amylose with radius corresponding to SEC regime and amylopectin with size typical for HDC – makes potato starch an ideal potential candidate to demonstrate the advantages of the hybrid chromatography. The binary pore structure facilitates separations through both size-exclusion (SEC) and flow in a channel (HDC). Additionally, the flow through channels allow much lower operating pressures when compared to standard bead packed columns (which prevents shear degradation). These aspects makes monolith columns the ideal candidate to separate such complex mixtures. We demonstrated this by running the same solution of potato starch in both the standard SEC and monolith columns as illustrated in Figure 7.5.

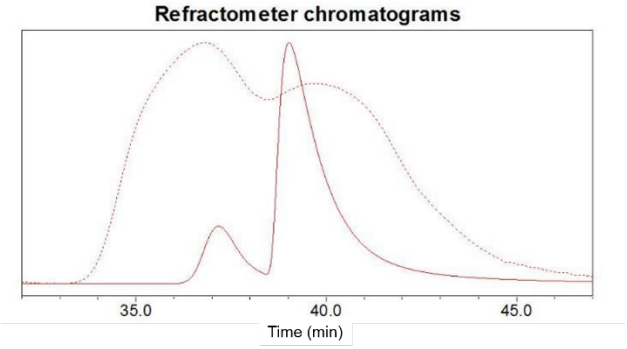

Figure 7.5– Resulting chromatograms of potato starch in a silica monolith (dashed line) and standard packed bead SEC column (solid line). Results are normalized to maximum peak height.

As is observed in Figure 7.5, the high molecular weight peak (lower elution time) is larger than the low molecule weight peak, indicating a higher concentration of the high molecular weight species (amylopectin). However, for the SEC column, the high molecular weight peak is significantly lower than the low molecular peak. We suggest this is due to two factors. First, the sample preparation method is different for these two columns. For the SEC sample preparation, the potato starch solution is filtered through a 0.2 μm filter to prevent the column from becoming plugged. When larger filters (e.g. 1.0 μm) are used, the column becomes plugged after injection. As a result of the smaller filter, high molecular weight species in the sample are filtered out. However, because of the continuous flow through channels in the silica monoliths, 1.0 μm filters are used without issue. Second, due to the pinch points in packed-beds, much higher pressures are required in the SEC columns compared to the silica columns. High pressures are likely to cause shear degradation of the high molecular weight species, further decreases the corresponding peak.

Our analysis shows that only monolith columns allow for quantitative characterization of polymers and particles with broad size distribution covering both regimes of separation by size.

7.6 Conclusion

A new hybrid liquid chromatography (HLC) theory is developed which describes separations in different types of chromatographic columns. The HLC theory combines the existing theory for hydrodynamic chromatography and size-exclusion chromatography. The elution time is described as $V_r(r_{eff}) = K_{HDC}V_0 + K_{SEC}V_i$, where scaling functions

K_{HDC} and K_{SEC} are calculated from theories of corresponding separations. The theory is tested using commercially available silica monolith columns with narrow polydispersity polymer standards of broad range of sizes. It is found that PMMA and polystyrene standards adsorb to the column wall, whereas pullulan appears not to have any column affinity. Using regression, the model parameters, which describe the column structure, are fit to the pullulan data, providing a very close match with the vendor reported column parameters. Difference is observed for calculated macropore radius, however we suggest the method we use to find this value is a much more reliable approach than the one suggested in literature. This claim is supported by the fact that the current suggestion in literature requires finding an equivalent macropore radius from relationships that are developed (and assume) a packed bed, whereas the HLC uses HDC theory to calculate macropore radius. The monolith columns and HLC is then used to characterize a complex polysaccharide, i.e potato starch, with broad size distribution. Our work clearly demonstrated that commercially available silica monoliths can be used for HLC characterization of complex polysaccharides and other highly polydisperse polymer and nanoparticle samples.

8 Conclusions

8.1 Adhesion, Encapsulation, and Release of Nanoparticles by Lipid Bilayers

First discussed was the process of NP intake then release from LBs. It was found that the energy barrier of intake increases with NP size. However, for release, the energy barrier is non-monotonic. It is smallest for the middle sized 2 nm NP, then larger for the 1 nm NP, and finally largest for the 4 nm NP. The high energy barrier for the release of the

1 nm NP appears to be associated with a junction that forms between the LB and NP, which has a very high energy penalty. We also used the Fokker-Planck equation to investigate the dynamics of NP intake and release. The time calculated from this model indicated that the two smallest NPs would quickly become incorporated into the LB in a real biological environment. However, the time of release, especially for the 1 nm NP, is prohibitively long. This result explains the experimentally observed phenomena of NPs accumulated in a LB. This work was presented at:

Burgess et al., Adhesion and Translocation of Nanoparticles through Lipid Bilayers *90th ACS Colloid & Surface Science Symposium* **2016**

Burgess et al. Adhesion and Translocation of Nanoparticles through Lipid Bilayers Studied by Mesoscale Simulations, *AIChE National Conference* **2016**

This work also resulted in the publication:

Burgess et al., Adhesion, Intake, and Release of Nanoparticles by Lipid Bilayers. *JCIS*, **2020**, *561*, 58-70.

8.2 Nanoparticle Engendered Rupture of Lipid Bilayers

Investigating a second aspect of NP-LB interactions, the effect an incorporated NP on LB stability was studied. NPs of different sizes (1, 2, 3, and 4 nm) and of both spherical and cylindrical shape were studied. Starting from the Deryugin-Gutop model of film rupture, which describes the energy change associated with hole formation in a film, the model was expanded to include incorporated NPs. This was done by suggesting hole formation can occur either homogenously (as if a NP were not there) or heterogeneously (near the surface of the NP). Using line tension as a fitting parameter, which is constant

across all NP shapes and sizes, the model is able to capture simulated results very well. It was found that as NP size increases, stability of the membrane decreases. Additionally, a spherical NP reduces the LB stability less than a cylindrical NP of the same radius. In the course of this project I mentored an undergraduate student, Christopher Tsovko who is listed on an author on the associated publication. This work was presented at:

Burgess et al. Nanoparticle Induce Rupture of Lipid Bilayers. *AIChE National Conference* **2018**

This worked resulted in the publication:

Burgess et al., Nanoparticle-Engendered Rupture of Lipid Membranes. *J. Phys. Chem. Lett*. **2018**, *9(17)* 4872-4877

8.3 Nanoparticle Interactions with Supported Lipid Bilayers Using an Implicit Solvent Models

The only simulation project that did not use DPD, I mentored a Master's student to conduct simulations to study NP interactions with supported LBs through the use of a coarse-grain molecular dynamics implicit solvent model. Using results from atomistic molecular dynamics, a force field was developed which reasonably reproduces the disjoining pressure between a silica substrate and lipid bilayer. This model allowed us to probe the cause of hole formation as a LB is laid across a substrate that is peppered with NPs. Qualitatively replicating experimental results with respect to the size of hole formation, we were able to determine holes form within the membrane due to excess bending of the LB. This project lasted about three years, all of which I was actively involved in mentoring Parva Patel. I helped him to understand how to properly set up a computational experimental, how to run simulations, investigate difficult questions, etc.

8.4 Nanoparticle Flow in Polymer Grafted Channels

This project investigated NP flow in polymer grafted channels. Previous work in the Neimark group had shown that the fluid has a Poiuselle flow profile in a channel with soft walls, but it was unclear whether the NP moved along with solvent velocity. It was found that NP flowed as if the channel walls were composed of a hard surface, that is, there is no difference with existing theory with respect to the rate of analyte flow in a channel. We further went on to show that the simulated results for a NP in a soft-walled channel matched the experimental results for NP flow in a hard wall channel. The agreement existed despite the 3 order in magnitude difference in scale. This work resulted in the publication Burgess et al., Nanoparticle Flow in Polymer Grafted Channels. *J. Phys. Chem. C* **2020** (At the time of writing, this paper was still in preprint and did not have page numbers or volume assigned).

8.5 Hybrid Liquid Chromatography in Silica Monolith Columns

The last project was experimental in nature and studied chromatography in monolith columns. A new theoretical model to describe monolith columns was developed by combining existing HDC and SEC theories. Using this theory, the column parameters were determined and matched well with the vendor reported values. It was also shown that monolith columns are very useful for separations of complex compounds (a mixture of two compounds) such as potato starch. The macropores are able to resolve amylopectin (a large polymer) contained within potato starch, while the mesopores can resolve amylose (a small polymer). Because of the flow through pores in monolith columns, amylopectin does not experience shear degradation like it would in standard SEC columns. Preparation of a manuscript is ongoing.

9 Bibliography

1. Hinde, R. J., Quantum Chemistry, 5th Edition (by Ira N. Levine). *Journal of Chemical Education* **2000,** *77* (12), 1564.
2. Gorban, A. N.; Karlin, I. V., Beyond Navier-Stokes equations: capillarity of ideal gas. *Contemp Phys* **2017,** *58* (1), 70-90.
3. Glotzer, S. C.; Paul, W., Molecular and mesoscale simulation methods for polymer materials. *Annu Rev Mater Res* **2002,** *32*, 401-436.
4. Moeendarbary, E.; Ng, T. Y.; Zangeneh, M., Dissipative Particle Dynamics: Introduction, Methodology and Complex Fluid Applications - a Review. *Int J Appl Mech* **2009,** *1* (4), 737-763.
5. Espanol, P.; Warren, P. B., Perspective: Dissipative particle dynamics. *J Chem Phys* **2017,** *146* (15).
6. Hoogerbrugge, P. J.; Koelman, J. M. V. A., Simulating Microscopic Hydrodynamic Phenomena with Dissipative Particle Dynamics. *Europhys Lett* **1992,** *19* (3), 155-160.
7. Groot, R. D.; Warren, P. B., Dissipative particle dynamics: Bridging the gap between atomistic and mesoscopic simulation. *J Chem Phys* **1997,** *107* (11), 4423-4435.
8. Groot, R. D.; Rabone, K. L., Mesoscopic simulation of cell membrane damage, morphology change and rupture by nonionic surfactants. *Biophys J* **2001,** *81* (2), 725-736.
9. Pool, R.; Bolhuis, P. G., Can purely repulsive soft potentials predict micelle formation correctly? *Phys Chem Chem Phys* **2006,** *8* (8), 941-948.
10. Smith, K. A.; Jasnow, D.; Balazs, A. C., Designing synthetic vesicles that engulf nanoscopic particles. *J Chem Phys* **2007,** *127* (8).
11. Alexeev, A.; Uspal, W. E.; Balazs, A. C., Harnessing Janus Nanoparticles to Create Controllable Pores in Membranes. *ACS Nano* **2008,** *2* (6), 1117-1122.
12. Ginzburg, V.; Balijepalli, S.; Smith, K. A.; Balaszs, A., Approaches to Mesoscale Modeling of Nanoparticle–Cell Membrane Interactions. *Nanotechnologies for the Life Sciences* **2010**.
13. Djohari, H.; Dormidontova, E. E., Kinetics of Nanoparticle Targeting by Dissipative Particle Dynamics Simulations. *Biomacromolecules* **2009,** *10* (11), 3089-3097.
14. Cheng, J. L.; Vishnyakov, A.; Neimark, A. V., Adhesion of nanoparticles to polymer brushes studied with the ghost tweezers method. *J Chem Phys* **2015,** *142* (3).
15. Santo, K. P.; Vishnyakov, A.; Brun, Y.; Neimark, A. V., Adhesion and Separation of Nanoparticles on Polymer-Grafted Porous Substrates. *Langmuir* **2018,** *34* (4), 1481-1496.
16. Schlick, T., *Molecular Modeling and Simulation: An Interdisciplinary Guide*. Springer Science+Business Media, LLC: New York, New York, 2010; Vol. 21, p 723.
17. Teli, M. K.; Mutalik, S.; Rajanikant, G. K., Nanotechnology and Nanomedicine: Going Small Means Aiming Big. *Curr. Pharm. Des.* **2010,** *16* (16), 1882-1892.
18. Gonzalez-Perez, A.; Persson, K. M., Bioinspired Materials for Water Purification. *Materials* **2016,** *9* (6).

19. Rosenholm, J.; Sahlgren, C.; Linden, M., Cancer-Cell Targeting and Cell-Specific Delivery by Mesoporous Silica Nanoparticles. *J. Mater. Chem.* **2010,** *20* (14), 2707-2713.
20. Witasp, E.; Kupferschmidt, N.; Bengtsson, L.; Hultenby, K.; Smedman, C.; Paulie, S.; Garcia-Bennett, A. E.; Fadeel, B., Efficient internalization of mesoporous silica particles of different sizes by primary human macrophages without impairment of macrophage clearance of apoptotic or antibody-opsonized target cells. *Toxicol Appl Pharm* **2009,** *239* (3), 306-319.
21. Nel, A.; Xia, T.; Madler, L.; Li, N., Toxic Potential of Materials at the Nanolevel. *Science* **2006,** *311* (5761), 622-627.
22. Nel, A. E.; Madler, L.; Velegol, D.; Xia, T.; Hoek, E. M. V.; Somasundaran, P.; Klaessig, F.; Castranova, V.; Thompson, M., Understanding Biophysicochemical Interactions at the Nano-Bio Interface. *Nat. Mater.* **2009,** *8* (7), 543-557.
23. Lu, F.; Wu, S. H.; Hung, Y.; Mou, C. Y., Size Effect on Cell Uptake in Well-Suspended, Uniform Mesoporous Silica Nanoparticles. *Small* **2009,** *5* (12), 1408-1413.
24. Lin, Y. S.; Haynes, C. L., Impacts of Mesoporous Silica Nanoparticle Size, Pore Ordering, and Pore Integrity on Hemolytic Activity. *J. Am. Chem. Soc.* **2010,** *132* (13), 4834-4842.
25. Slowing, I. I.; Wu, C. W.; Vivero-Escoto, J. L.; Lin, V. S. Y., Mesoporous Silica Nanoparticles for Reducing Hemolytic Activity Towards Mammalian Red Blood Cells. *Small* **2009,** *5* (1), 57-62.
26. Yang, K.; Ma, Y. Q., Computer simulation of the translocation of nanoparticles with different shapes across a lipid bilayer. *Nat. Nano.* **2010,** *5* (8), 579-583.
27. Bedrov, D.; Smith, G. D.; Davande, H.; Li, L. W., Passive transport of C-60 fullerenes through a lipid membrane: A molecular dynamics simulation study. *J Phys Chem B* **2008,** *112* (7), 2078-2084.
28. Fiedler, S. L.; Violi, A., Simulation of Nanoparticle Permeation through a Lipid Membrane. *Biophys J* **2010,** *99* (1), 144-152.
29. Sridhar, A.; Srikanth, B.; Kumar, A.; Dasmahapatra, A. K., Coarse-grain molecular dynamics study of fullerene transport across a cell membrane. *J Chem Phys* **2015,** *143* (2).
30. Makarucha, A. J.; Todorova, N.; Yarovsky, I., Nanomaterials in biological environment: a review of computer modelling studies. *Eur Biophys J Biophy* **2011,** *40* (2), 103-115.
31. Schulz, M.; Olubummo, A.; Binder, W. H., Beyond the lipid-bilayer: interaction of polymers and nanoparticles with membranes. *Soft Matter* **2012,** *8* (18), 4849-4864.
32. Guo, Y. T., E; Seemann R; Fleury J.B.; Baulin, V.A., Direct proof of spontaneous translocation of lipid-covered hydrophobic nanoparticles through a phospholipid bilayer. *Sci Adv* **2016,** *2*.
33. Ding, H. M.; Tian, W. D.; Ma, Y. Q., Designing Nanoparticle Translocation through Membranes by Computer Simulations. *ACS Nano* **2012,** *6* (2), 1230-1238.
34. Yue, T. T.; Zhang, X. R.; Huang, F., Molecular modeling of membrane responses to the adsorption of rotating nanoparticles: promoted cell uptake and mechanical membrane rupture. *Soft Matter* **2015,** *11* (3), 456-465.

35. Gupta, R.; Rai, B., Effect of Size and Surface Charge of Gold Nanoparticles on their Skin Permeability: A Molecular Dynamics Study. *Sci Rep-Uk* **2017,** *7*.
36. Mhashal, A. R.; Choudhury, C. K.; Roy, S., Probing the ATP-induced conformational flexibility of the PcrA helicase protein using molecular dynamics simulation. *J Mol Model* **2016,** *22* (3).
37. Gupta, R.; Kashyap, N.; Rai, B., Transdermal cellular membrane penetration of proteins with gold nanoparticles: a molecular dynamics study. *Phys Chem Chem Phys* **2017,** *19* (11), 7537-7545.
38. Li, Y. F.; Li, X. J.; Li, Z. H.; Gao, H. J., Surface-structure-regulated penetration of nanoparticles across a cell membrane. *Nanoscale* **2012,** *4* (12), 3768-3775.
39. Pogodin, S.; Baulin, V. A., Equilibrium Insertion of Nanoscale Objects into Phospholipid Bilayers. *Curr Nanosci* **2011,** *7* (5), 721-726.
40. Alipour, E.; Halverson, D.; McWhirter, S.; Walker, G. C., Phospholipid Bilayers: Stability and Encapsulation of Nanoparticles. *Annu Rev Phys Chem* **2017,** *68*, 261-283.
41. Keating, J. J.; Imbrogno, J.; Belfort, G., Polymer Brushes for Membrane Separations: A Review. *Acs Appl Mater Inter* **2016,** *8* (42), 28383-28399.
42. Ayres, N., Polymer brushes: Applications in biomaterials and nanotechnology. *Polym Chem-Uk* **2010,** *1* (6), 769-777.
43. Kumar, S. K.; Benicewicz, B. C.; Vaia, R. A.; Winey, K. I., 50th Anniversary Perspective: Are Polymer Nanocomposites Practical for Applications? *Macromolecules* **2017,** *50* (3), 714-731.
44. Crosby, A. J.; Lee, J. Y., Polymer nanocomposites: The "nano" effect on mechanical properties. *Polym Rev* **2007,** *47* (2), 217-229.
45. Paul, D. R.; Robeson, L. M., Polymer nanotechnology: Nanocomposites. *Polymer* **2008,** *49* (15), 3187-3204.
46. Borukhov, I.; Leibler, L., Enthalpic stabilization of brush-coated particles in a polymer melt. *Macromolecules* **2002,** *35* (13), 5171-5182.
47. Witten, T. A.; Pincus, P. A., Colloid Stabilization by Long Grafted Polymers. *Macromolecules* **1986,** *19* (10), 2509-2513.
48. Prokhorova, S. A.; Kopyshev, A.; Ramakrishnan, A.; Zhang, H.; Ruhe, J., Can polymer brushes induce motion of nano-objects? *Nanotechnology* **2003,** *14* (10), 1098-1108.
49. Roda, B.; Zattoni, A.; Reschiglian, P.; Moon, M. H.; Mirasoli, M.; Michelini, E.; Roda, A., Field-flow fractionation in bioanalysis: A review of recent trends. *Anal Chim Acta* **2009,** *635* (2), 132-143.
50. Baalousha, M.; Stolpe, B.; Lead, J. R., Flow field-flow fractionation for the analysis and characterization of natural colloids and manufactured nanoparticles in environmental systems: A critical review. *J Chromatogr A* **2011,** *1218* (27), 4078-4103.
51. Liu, J.; Andya, J. D.; Shire, S. J., A critical review of analytical ultracentrifugation and field flow fractionation methods for measuring protein aggregation. *Aaps J* **2006,** *8* (3), 580-589.
52. Berek, D., Size exclusion chromatography - A blessing and a curse of science and technology of synthetic polymers. *J Sep Sci* **2010,** *33* (3), 315-335.

53. Wei, G.-T.; Liu, F.-K., Separation of Nanometer Gold Particles by Size Exclusion Chromatography. *J. Chromatogr. A* **1999,** *836* (2), 253-260.
54. Barth, H. G.; Boyes, B. E.; Jackson, C., Size exclusion chromatography. *Anal Chem* **1996,** *68* (12), 445-466.
55. Striegel, A. M.; Brewer, A. K., Hydrodynamic Chromatography. *Annu Rev Anal Chem* **2012,** *5*, 15-34.
56. Arita, T.; Yoshimura, T.; Adschiri, T., Size exclusion chromatography of quantum dots by utilizing nanoparticle repelling surface of concentrated polymer brush. *Nanoscale* **2010,** *2* (8), 1467-1473.
57. Santo, K. P.; Vishnyakov, A.; Brun, Y.; Neimark, A. V., Critical Conditions of Adhesion and Separation of Functionalized Nanoparticles on Polymer Grafted Substrates. *J Phys Chem C* **2019,** *123* (26), 16091-16106.
58. Korolev, A.; Victorova, E.; Ibragimov, T.; Kanatyeva, A.; Kurganov, A., Monolithic columns with optimized pore structure for molecular size-based separations of synthetic polymers. *J Sep Sci* **2012,** *35* (8), 957-963.
59. Gritti, F.; Piatkowski, W.; Guiochon, G., Study of the mass transfer kinetics in a monolithic column. *J Chromatogr A* **2003,** *983* (1-2), 51-71.
60. Cabrera, K.; Machtejevas, E., New Generation Monolithic Silica Columns for Fast, High Resolution Drug Separations without High Pressures. *Lc Gc N Am* **2013**, 25-25.
61. Tijssen, R.; Bos, J.; Vankreveld, M. E., Hydrodynamic Chromatography of Macromolecules in Open Microcapillary Tubes. *Anal Chem* **1986,** *58* (14), 3036-3044.
62. Brenner, H.; Gaydos, L. J., Constrained Brownian-Movement of Spherical-Particles in Cylindrical Pores of Comparable Radius - Models of Diffusive and Convective Transport of Solute Molecules in Membranes and Porous-Media. *J Colloid Interf Sci* **1977,** *58* (2), 312-356.
63. Dimarzio, E. A.; Guttman, C. M., Separation by Flow. *J Polym Sci Pol Lett* **1969,** *7* (4pb), 267-272.
64. Dimarzio, E. A.; Guttman, C. M., Separation by Flow and Its Application to Gel Permeation Chromatography. *J Chromatogr* **1971,** *55* (1), 83-97.
65. Guttman, C. M.; Dimarzio, E. A., Separation by Flow .Part 2. Application to Gel Permeation Chromatography. *Macromolecules* **1970,** *3* (5), 681-691.
66. Staben, M. E.; Zinchenko, A. Z.; Davis, R. H., Motion of a particle between two parallel plane walls in low-Reynolds-number Poiseuille flow. *Phys Fluids* **2003,** *15* (6), 1711-1733.
67. Staben, M. E.; Davis, R. H., Particle transport in Poiseuille flow in narrow channels. *Int J Multiphas Flow* **2005,** *31* (5), 529-547.
68. Dechadilok, P.; Deen, W. M., Hindrance factors for diffusion and convection in pores. *Ind Eng Chem Res* **2006,** *45* (21), 6953-6959.
69. Weinbaum, S.; Dagan, Z.; Ganatos, P.; Pfeffer, R., Strong Interaction between Particles and Boundaries at Low Reynolds-Numbers. *Ann Ny Acad Sci* **1983,** *404* (May), 308-309.

70. Ganatos, P.; Pfeffer, R.; Weinbaum, S., A Strong Interaction Theory for the Creeping Motion of a Sphere between Plane Parallel Boundaries .Part 2. Parallel Motion. *J Fluid Mech* **1980,** *99* (Aug), 755-783.
71. Korolev, A. A.; Viktorova, E. N.; Kurganov, A. A., Hydrodynamic Chromatography of Polystyrenes on Hollow Capillary Columns. *Russ J Phys Chem A* **2018,** *92* (11), 2320-2324.
72. Tijssen, R.; Bleumer, J. P. A.; Vankreveld, M. E., Separation by Flow (Hydrodynamic Chromatography) of Macromolecules Performed in Open Microcapillary Tubes. *J Chromatogr* **1983,** *260* (2), 297-304.
73. Stegeman, G.; Oostervink, R.; Kraak, J. C.; Poppe, H.; Unger, K. K., Hydrodynamic Chromatography of Macromolecules on Small Spherical Nonporous Silica Particles. *J Chromatogr* **1990,** *506*, 547-561.
74. Skudas, R.; Grimes, B. A.; Thommes, M.; Unger, K. K., Flow-through pore characteristics of monolithic silicas and their impact on column performance in high-performance liquid chromatography. *J Chromatogr A* **2009,** *1216* (13), 2625-2636.
75. Edam, R.; Eeltink, S.; Vanhoutte, D. J. D.; Kok, W. T.; Schoenmakers, P. J., Hydrodynamic chromatography of macromolecules using polymer monolithic columns. *J Chromatogr A* **2011,** *1218* (48), 8638-8645.
76. Ikegami, T.; Tanaka, N., Recent Progress in Monolithic Silica Columns for High-Speed and High-Selectivity Separations. *Annual Review of Analytical Chemistry, Vol 9* **2016,** *9*, 317-342.
77. Tanaka, N.; Kobayashi, H.; Nakanishi, K.; Minakuchi, H.; Ishizuka, N., Monolithic LC columns. *Anal Chem* **2001,** *73* (15), 420a-429a.
78. Groarke, R. J.; Brabazon, D., Methacrylate Polymer Monoliths for Separation Applications. *Materials* **2016,** *9* (6).
79. Ali, I.; Gaitonde, V. D.; Aboul-Enein, H. Y., Monolithic Silica Stationary Phases in Liquid Chromatography. *J Chromatogr Sci* **2009,** *47* (6), 432-442.
80. Bakry, R.; Huck, C. W.; Bonn, G. K., Recent Applications of Organic Monoliths in Capillary Liquid Chromatographic Separation of Biomolecules. *J Chromatogr Sci* **2009,** *47* (6), 418-431.
81. Causon, T. J.; Nischang, I., Critical differences in chromatographic properties of silica- and polymer-based monoliths. *J Chromatogr A* **2014,** *1358*, 165-171.
82. Nischang, I.; Causon, T. J., Porous polymer monoliths: From their fundamental structure to analytical engineering applications. *Trac-Trend Anal Chem* **2016,** *75*, 108-117.
83. Lubda, D.; Lindner, W.; Quaglia, M.; von Hohenesche, C. D.; Unger, K. K., Comprehensive pore structure characterization of silica monoliths with controlled mesopore size and macropore size by nitrogen sorption, mercury porosimetry, transmission electron microscopy and inverse size exclusion chromatography. *J Chromatogr A* **2005,** *1083* (1-2), 14-22.
84. Wouters, S.; Hauffman, T.; Mittelmeijer-Hazeleger, M. C.; Rothenberg, G.; Desmet, G.; Baron, G. V.; Eeltink, S., Comprehensive study of the macropore and mesopore size distributions in polymer monoliths using complementary physical

characterization techniques and liquid chromatography. *J Sep Sci* **2016,** *39* (23), 4492-4501.
85. Leinweber, F. C.; Lubda, D.; Cabrera, K.; Tallarek, U., Characterization of silica-based monoliths with bimodal pore size distribution. *Anal Chem* **2002,** *74* (11), 2470-2477.
86. Svec, F.; Lv, Y. Q., Advances and Recent Trends in the Field of Monolithic Columns for Chromatography. *Anal Chem* **2015,** *87* (1), 250-273.
87. Viktorova, E. N.; Korolev, A. A.; Ivanov, V. A.; Ibragimov, T. R.; Kurganov, A. A., Molecular mass analysis of polymers on monolithic capillary columns based on divinylbenzene. *Russ J Phys Chem a+* **2012,** *86* (9), 1473-1478.
88. Viktorova, E. N.; Korolev, A. A.; Rodionov, S. V.; Kurganov, A. A., Investigating the Structure of a Monolithic Capillary Column by Means of Hydrodynamic and Size-Exclusion Chromatography. *Russ J Phys Chem a+* **2011,** *85* (1), 125-129.
89. Groot, R. D.; Rabone, K. L., Mesoscopic Simulation of Cell Membrane Damage, Morphology Change and Rupture by Nonionic Surfactants. *Biophys. J.* **2001,** *81* (2), 725-736.
90. Evans, E.; Rawicz, W., Entropy-Driven Tension and Bending Elasticity in Condensed-Fluid Membranes. *Phys Rev Lett* **1990,** *64* (17), 2094-2097.
91. Petrache, H. I.; Tristram-Nagle, S.; Nagle, J. F., Fluid phase structure of EPC and DMPC bilayers. *Chem Phys Lipids* **1998,** *95* (1), 83-94.
92. Petrache, H. I.; Tristram-Nagle, S.; Nagle, J. F., Fluid Phase Structure of EPC and DMPC Bilayers. *Chem Phys Lipids* **1998,** *95* (1), 83-94.
93. Forgacs, G.; Foty, R. A.; Shafrir, Y.; Steinberg, M. S., Viscoelastic properties of living embryonic tissues: a quantitative study. *Biophys. J.* **1998,** *74* (5), 2227-2234.
94. Burgess, S., Vishnyakov, A., Tsovko, C., Neimark, A.V., Nanoparticle-Engendered Rupture of Lipid Membranes. *J. Chem. Phys.* **2018,** *9*, 4872-4877.
95. Jusufi, A.; DeVane, R. H.; Shinoda, W.; Klein, M. L., Nanoscale carbon particles and the stability of lipid bilayers. *Soft Matter* **2011,** *7* (3), 1139-1146.
96. Smit, B.; Frenkel, D., *Understanding Molecular Simulation: From Algorithms to Applications*. Academic Press: 2012.
97. Plimpton, S., Fast Parallel Algorithms for Short-Range Molecular-Dynamics. *J. Comput. Phys.* **1995,** *117* (1), 1-19.
98. Towns, J.; Cockerill, T.; Dahan, M.; Foster, I.; Gaither, K.; Grimshaw, A.; Hazlewood, V.; Lathrop, S.; Lifka, D.; Peterson, G. D.; Roskies, R.; Scott, J. R.; Wilkins-Diehr, N., XSEDE: Accelerating Scientific Discovery. *Comput Sci Eng* **2014,** *16* (5), 62-74.
99. Seaton, M. A.; Anderson, R. L.; Metz, S.; Smith, W., DL_MESO: Highly Scalable Mesoscale Simulations. *Mol. Simulat.* **2013,** *39* (10), 796-821.
100. Cheng, J. L.; Vishnyakov, A.; Neimark, A. V., Adhesion of nanoparticles to polymer brushes studied with the ghost tweezers method. *J. Chem. Phys.* **2015,** *142* (3).
101. Kong, C. Y.; Muthukumar, M., Polymer translocation through a nanopore. 2. Excluded volume effect. *J. Chem. Phys.* **2004,** *120* (7), 3460-3466.
102. Park, P. J.; Sung, W., Polymer release out of a spherical vesicle through a pore. *Phys. Rev. E* **1998,** *57* (1), 730-734.

103. Kuni, F. M.; Grinin, A. P.; Shchekin, A. K., The microphysical effects in nonisothermal nucleation. *Physica A* **1998,** *252* (1-2), 67-84.
104. Barkai, E., Fractional Fokker-Planck equation, solution, and application. *Phys. Rev. E* **2001,** *63* (4).
105. Khan, S.; Reynolds, A. M., Derivation of a Fokker-Planck equation for generalized Langevin dynamics. *Physica A* **2005,** *350* (2-4), 183-188.
106. Metzler, R.; Barkai, E.; Klafter, J., Anomalous diffusion and relaxation close to thermal equilibrium: A fractional Fokker-Planck equation approach. *Phys. Rev. Lett.* **1999,** *82* (18), 3563-3567.
107. Kramers, H. A., Brownian Motion in a Field of Force and the Diffusion Model of Chemical Reactions. *Physica VII* **1940,** *4*.
108. Su, C. F.; Merlitz, H.; Rabbel, H.; Sommer, J. U., Nanoparticles of Various Degrees of Hydrophobicity Interacting with Lipid Membranes. *J. Phys. Chem. Lett.* **2017,** *8* (17), 4069-4076.
109. Guo, Y. C.; Terazzi, E.; Seemann, R.; Fleury, J. B.; Baulin, V. A., Direct proof of spontaneous translocation of lipid-covered hydrophobic nanoparticles through a phospholipid bilayer. *Sci. Adv.* **2016,** *2* (11).
110. Makarucha, A. J.; Todorova, N.; Yarovsky, I., Nanomaterials in biological environment: a review of computer modelling studies. *Eur Biophys J Biophy* **2011,** *40* (2), 103-115.
111. Bahrami, A. H.; Raatz, M.; Agudo-Canalejo, J.; Michel, R.; Curtis, E. M.; Hall, C. K.; Gradzielski, M.; Lipowsky, R.; Weikl, T. R., Wrapping of nanoparticles by membranes. *Advances in Colloid and Interface Science* **2014,** *208*, 214-224.
112. Lipowsky, R.; Dobereiner, H. G., Vesicles in contact with nanoparticles and colloids. *Europhysics Letters* **1998,** *43* (2), 219-225.
113. Meng, X. P.; Li, X. L., Size Limit and Energy Analysis of Nanoparticles during Wrapping Process by Membrane. *Nanomaterials* **2018,** *8* (11).
114. Vishnyakov, A.; Li, T.; Neimark, A. V., Adhesion of Phospholipid Bilayers to Hydroxylated Silica: Existence of Nanometer-Thick Water Interlayers. *Langmuir* **2017,** *33* (45), 13148-13156.
115. Pertsin, A.; Grunze, M., Possible mechanism of adhesion in a mica supported phospholipid bilayer. *J. Chem. Phys.* **2014,** *140* (18).
116. Deryagin, B. V.; Gutop, Y. V., Theory of the Breakdown (Rupture) of Free Films. *Kolloidn Zh.* **1962,** *24*, 370-374.
117. Akimov, S. A.; Volynsky, P. E.; Galimzyanov, T. R.; Kuzmin, P. I.; Pavlov, K. V.; Batishchev, O. V., Pore formation in lipid membrane I: Continuous reversible trajectory from intact bilayer through hydrophobic defect to transversal pore. *Sci Rep-Uk* **2017,** *7*.
118. Ting, C. L.; Appelo, D.; Wang, Z. G., Minimum Energy Path to Membrane Pore Formation and Rupture. *Phys Rev Lett* **2011,** *106* (16).
119. Zhdanov, V. P., Mechanism of rupture of single adsorbed vesicles. *Chem Phys Lett* **2015,** *641*, 20-22.

120. Wohlert, J.; den Otter, W. K.; Edholm, O.; Briels, W. J., Free energy of a trans-membrane pore calculated from atomistic molecular dynamics simulations. *J Chem Phys* **2006,** *124* (15).
121. Tolpekina, T. V.; den Otter, W. K.; Briels, W. J., Nucleation free energy of pore formation in an amphiphilic bilayer studied by molecular dynamics simulations. *J Chem Phys* **2004,** *121* (23), 12060-12066.
122. Pera, H.; Kleijn, J. M.; Leermakers, F. A. M., On the edge energy of lipid membranes and the thermodynamic stability of pores. *J Chem Phys* **2015,** *142* (3).
123. Dehghan, A.; Pastor, K. A.; Shi, A. C., Line tension of multicomponent bilayer membranes. *Physical Review E* **2015,** *91* (2).
124. Portet, T.; Dimova, R., A New Method for Measuring Edge Tensions and Stability of Lipid Bilayers: Effect of Membrane Composition. *Biophys J* **2010,** *99* (10), 3264-3273.
125. Ting, C. L.; Appelo, D.; Wang, Z. G., Minimum Energy Path to Membrane Pore Formation and Rupture. *Phys. Rev. Lett.* **2011,** *106* (16), 168101.
126. Tolpekina, T. V.; den Otter, W. K.; Briels, W. J., Simulations of stable pores in membranes: System size dependence and line tension. *J Chem Phys* **2004,** *121* (16), 8014-8020.
127. Jiang, F. Y.; Bouret, Y.; Kindt, J. T., Molecular dynamics simulation of the lipid bilayer edge. *Abstr Pap Am Chem S* **2003,** *226*, U332-U332.
128. Zhelev, D. V.; Needham, D., Tension-Stabilized Pores in Giant Vesicles - Determination of Pore-Size and Pore Line Tension. *Biochim. Biophys. Acta* **1993,** *1147* (1), 89-104.
129. Kim, D. H.; Frangos, J. A., Effects of amyloid beta-peptides on the lysis tension of lipid bilayer vesicles containing oxysterols. *Biophys J* **2008,** *95* (2), 620-628.
130. Levadny, V.; Tsuboi, T.; Belaya, M.; Yamazaki, M., Rate Constant of Tension-Induced Pore Formation in Lipid Membranes. *Langmuir* **2013,** *29* (12), 3848-3852.
131. Akimov, S. A.; Volynsky, P. E.; Galimzyanov, T. R.; Kuzmin, P. I.; Pavlov, K. V.; Batishchev, O. V., Pore formation in lipid membrane II: Energy landscape under external stress. *Sci Rep-Uk* **2017,** *7*.
132. Evans, E.; Smith, B. A., Kinetics of Hole Nucleation in Biomembrane Rupture. *New J. Phys.* **2011,** *13*, 095010.
133. Shibly, S. U. A.; Ghatak, C.; Karal, M. A. S.; Moniruzzaman, M.; Yamazaki, M., Experimental Estimation of Membrane Tension Induced by Osmotic Pressure. *Biophys J* **2016,** *111* (10), 2190-2201.
134. Hochmuth, R. M., Micropipette aspiration of living cells. *J Biomech* **2000,** *33* (1), 15-22.
135. Hanggi, P.; Talkner, P.; Borkovec, M., Reaction-Rate Theory - 50 Years after Kramers. *Rev Mod Phys* **1990,** *62* (2), 251-341.
136. Karal, M. A.; Levadnyy, V.; Yamazaki, M., Analysis of constant tension-induced rupture of lipid membranes using activation energy. *Phys Chem Chem Phys* **2016,** *18* (19), 13487-13495.
137. Karal, M. A. S.; Yamazaki, M., Communication: Activation Energy of Tension-Induced Pore Formation in Lipid Membranes. *J. Chem. Phys.* **2015,** *143* (8), 081103.

138. Karal, M. A.; Levadnyy, V.; Tsuboi, T. A.; Belaya, M.; Yamazaki, M., Electrostatic interaction effects on tension-induced pore formation in lipid membranes. *Phys Rev E* **2015,** *92* (1).
139. Ginzburg, V. V.; Balijepailli, S., Modeling the Thermodynamics of the Interaction of Nanoparticles with Cell Membranes. *Nano Lett.* **2007,** *7* (12), 3716-3722.
140. Vacha, R.; Martinez-Veracoechea, F. J.; Frenkel, D., Receptor-Mediated Endocytosis of Nanoparticles of Various Shapes. *Nano Lett* **2011,** *11* (12), 5391-5395.
141. Ting, C. L.; Wang, Z. G., Minimum free energy paths for a nanoparticle crossing the lipid membrane. *Soft Matter* **2012,** *8* (48), 12066-12071.
142. Seaton, M. A., The DL_Meso Mesoscale Simulation Package. *STFC Scientific Computing Department* **2012**.
143. Evans, E.; Heinrich, V.; Ludwig, F.; Rawicz, W., Dynamic tension spectroscopy and strength of biomembranes. *Biophys J* **2003,** *85* (4), 2342-2350.
144. Xie, J. Y.; Ding, G. H.; Karttunen, M., Molecular dynamics simulations of lipid membranes with lateral force: Rupture and dynamic properties. *Bba-Biomembranes* **2014,** *1838* (3), 994-1002.
145. Moroz, J. D.; Nelson, P., Dynamically stabilized pores in bilayer membranes. *Biophys J* **1997,** *72* (5), 2211-2216.
146. Castellana, E. T.; Cremer, P. S., Solid supported lipid bilayers: From biophysical studies to sensor design. *Surface Science Reports* **2006,** *61* (10), 429-444.
147. Groves, J. T.; Dustin, M. L., Supported planar bilayers in studies on immune cell adhesion and communication. *Journal of Immunological Methods* **2003,** *278* (1-2), 19-32.
148. Knoll, W.; Naumann, R.; Friedrich, M.; Robertson, J. W. F.; Losche, M.; Heinrich, F.; McGillivray, D. J.; Schuster, B.; Gufler, P. C.; Pum, D.; Sleytr, U. B., Solid supported lipid membranes: New concepts for the biomimetic functionalization of solid surfaces. *Biointerphases* **2008,** *3* (2), Fa125-Fa135.
149. Richter, R. P.; Berat, R.; Brisson, A. R., Formation of solid-supported lipid bilayers: An integrated view. *Langmuir* **2006,** *22* (8), 3497-3505.
150. Sackmann, E., Supported membranes: Scientific and practical applications. *Science* **1996,** *271* (5245), 43-48.
151. Tamm, L. K.; Mcconnell, H. M., Supported Phospholipid-Bilayers. *Biophys J* **1985,** *47* (1), 105-113.
152. Fischer, A.; Lösche, M.; Möhwald, H.; Sackmann, E., On the nature of the lipid monolayer phase transition. *Journal de Physique Lettres* **1984,** *45* (16), 785-791.
153. Eggl, P.; Pink, D.; Quinn, B.; Ringsdorf, H.; Sackmann, E., Diffusion in quasi two-dimensional macromolecular solutions. *Macromolecules* **1990,** *23* (14), 3472-3480.
154. Ye, J. S.; Ottova, A.; Tien, H. T.; Sheu, F. S., Nanostructured platinum-lipid bilayer composite as biosensor. *Bioelectrochemistry* **2003,** *59* (1-2), 65-72.
155. Bayerl, T. M.; Bloom, M., Physical-Properties of Single Phospholipid-Bilayers Adsorbed to Micro Glass-Beads - a New Vesicular Model System Studied by H-2-Nuclear Magnetic-Resonance. *Biophys J* **1990,** *58* (2), 357-362.

156. Johnson, S. J.; Bayerl, T. M.; Mcdermott, D. C.; Adam, G. W.; Rennie, A. R.; Thomas, R. K.; Sackmann, E., Structure of an Adsorbed Dimyristoylphosphatidylcholine Bilayer Measured with Specular Reflection of Neutrons. *Biophys J* **1991,** *59* (2), 289-294.
157. Anderson, T. H., Formation of Supported Bilayers on Silica Substrates. . *Langmuir* **2009,** *25*, 6997-700.
158. Valtiner, M.; Donaldson, S. H.; Gebbie, M. A.; Israelachvili, J. N., Hydrophobic Forces, Electrostatic Steering, and Acid–Base Bridging between Atomically Smooth Self-Assembled Monolayers and End-Functionalized PEGolated Lipid Bilayers. *Journal of the American Chemical Society* **2012,** *134* (3), 1746-1753.
159. Rapp, M. V.; Donaldson, S. H.; Gebbie, M. A.; Gizaw, Y.; Koenig, P.; Roiter, Y.; Israelachvili, J. N., Effects of Surfactants and Polyelectrolytes on the Interaction between a Negatively Charged Surface and a Hydrophobic Polymer Surface. *Langmuir* **2015,** *31* (29), 8013-8021.
160. Yu, J.; Kan, Y.; Rapp, M.; Danner, E.; Wei, W.; Das, S.; Miller, D. R.; Chen, Y.; Waite, J. H.; Israelachvili, J. N., Adaptive hydrophobic and hydrophilic interactions of mussel foot proteins with organic thin films. *Proceedings of the National Academy of Sciences* **2013,** *110* (39), 15680-15685.
161. Donaldson, S. H.; Das, S.; Gebbie, M. A.; Rapp, M.; Jones, L. C.; Roiter, Y.; Koenig, P. H.; Gizaw, Y.; Israelachvili, J. N., Asymmetric Electrostatic and Hydrophobic–Hydrophilic Interaction Forces between Mica Surfaces and Silicone Polymer Thin Films. *ACS Nano* **2013,** *7* (11), 10094-10104.
162. Das, C.; Sheikh, K. H.; Olmsted, P. D.; Connell, S. D., Nanoscale mechanical probing of supported lipid bilayers with atomic force microscopy. *Physical Review E* **2010,** *82* (4).
163. Schneider, J.; Barger, W.; Lee, G. U., Nanometer Scale Surface Properties of Supported Lipid Bilayers Measured with Hydrophobic and Hydrophilic Atomic Force Microscope Probes. *Langmuir* **2003,** *19* (5), 1899-1907.
164. Rico, F.; Abdulreda, M. H.; Moy, V. T.; Bhalla, A.; Chapman, E. R.; Berggren, P.-O., Pulling force generated by interacting SNAREs facilitates membrane hemifusion. *Integrative Biology* **2009,** *1* (4), 301-310.
165. Israelachvili, J. N.; Wennerstroem, H., Entropic forces between amphiphilic surfaces in liquids. *The Journal of Physical Chemistry* **1992,** *96* (2), 520-531.
166. Pera, I.; Stark, R.; Kappl, M.; Butt, H.-J.; Benfenati, F., Using the Atomic Force Microscope to Study the Interaction between Two Solid Supported Lipid Bilayers and the Influence of Synapsin I. *Biophysical Journal* **2004,** *87* (4), 2446-2455.
167. Kim, H. I.; Mate, C. M.; Hannibal, K. A.; Perry, S. S., How Disjoining Pressure Drives the Dewetting of a Polymer Film on a Silicon Surface. *Physical Review Letters* **1999,** *82* (17), 3496-3499.
168. Heine, D. R.; Rammohan, A. R.; Balakrishnan, J., Atomistic simulations of the interaction between lipid bilayers and substrates. *Molecular Simulation* **2007,** *33* (4-5), 391-397.

169. Roark, M.; Feller, S. E., Structure and Dynamics of a Fluid Phase Bilayer on a Solid Support as Observed by a Molecular Dynamics Computer Simulation. *Langmuir* **2008,** *24* (21), 12469-12473.
170. Pertsin, A.; Grunze, M., Possible mechanism of adhesion in a mica supported phospholipid bilayer. *Journal of Chemical Physics* **2014,** *140* (18), 8.
171. Xing, C. Y.; Faller, R., Interactions of lipid bilayers with supports: A coarse-grained molecular simulation study. *Journal of Physical Chemistry B* **2008,** *112* (23), 7086-7094.
172. Hoopes, M. I.; Deserno, M.; Longo, M. L.; Faller, R., Coarse-grained modeling of interactions of lipid bilayers with supports. *Journal of Chemical Physics* **2008,** *129* (17).
173. Roiter, Y.; Ornatska, M.; Rammohan, A. R.; Balakrishnan, J.; Heine, D. R.; Minko, S., Interaction of nanoparticles with lipid membrane. *Nano Letters* **2008,** *8* (3), 941-944.
174. Roiter, Y.; Ornatska, M.; Rammohan, A. R.; Balakrishnan, J.; Heine, D. R.; Minko, S., Interaction of Lipid Membrane with Nanostructured Surfaces. *Langmuir* **2009,** *25* (11), 6287-6299.
175. Noguchi, H.; Takasu, M., Self-assembly of amphiphiles into vesicles: A Brownian dynamics simulation. *Physical Review E* **2001,** *64* (4), 041913.
176. Drouffe, J.; Maggs, A.; Leibler, S., Computer simulations of self-assembled membranes. *Science* **1991,** *254* (5036), 1353-1356.
177. Brannigan, G.; Brown, F. L. H., Solvent-free simulations of fluid membrane bilayers. *Journal of Chemical Physics* **2004,** *120* (2), 1059-1071.
178. Farago, O., "Water-free" computer model for fluid bilayer membranes. *Journal of Chemical Physics* **2003,** *119* (1), 596-605.
179. Cooke, I. R.; Deserno, M., Solvent-free model for self-assembling fluid bilayer membranes: Stabilization of the fluid phase based on broad attractive tail potentials. *Journal of Chemical Physics* **2005,** *123* (22), 224710.
180. Patel, P. Coarse-grained modeling of interactions of nanoparticles with lipid membranes. Rutgers University, Piscataway, 2019.
181. Cooke, I. R.; Deserno, M., Solvent-free model for self-assembling fluid bilayer membranes: Stabilization of the fluid phase based on broad attractive tail potentials. *J Chem Phys* **2005,** *123* (22).
182. Cooke, I. R.; Kremer, K.; Deserno, M., Tunable generic model for fluid bilayer membranes. *Phys Rev E* **2005,** *72* (1).
183. Plimpton, S., Fast Parallel Algorithms for Short-Range Molecular-Dynamics. *J Comput Phys* **1995,** *117* (1), 1-19.
184. Cheng, J. L.; Vishnyakov, A.; Neimark, A. V., Morphological Transformations in Polymer Brushes in Binary Mixtures: DPD Study. *Langmuir* **2014,** *30* (43), 12932-12940.
185. Chen, S.; Phan-Thien, N.; Khoo, B. C.; Fan, X. J., Flow around spheres by dissipative particle dynamics. *Phys Fluids* **2006,** *18* (10).
186. Willemsen, S. M.; Hoefsloot, H. C. J.; Iedema, P. D., Mesoscopic simulation of polymers in fluid dynamics problems. *J Stat Phys* **2002,** *107* (1-2), 53-65.

187. Fedosov, D. A.; Karniadakis, G. E.; Caswell, B., Dissipative particle dynamics simulation of depletion layer and polymer migration in micro- and nanochannels for dilute polymer solutions. *J Chem Phys* **2008,** *128* (14).
188. Millan, J. A.; Jiang, W. H.; Laradji, M.; Wang, Y. M., Pressure driven flow of polymer solutions in nanoscale slit pores. *J Chem Phys* **2007,** *126* (12).
189. Millan, J. A.; Laradji, M., Cross-Stream Migration of Driven Polymer Solutions in Nanoscale Channels: A Numerical Study with Generalized Dissipative Particle Dynamics. *Macromolecules* **2009,** *42* (3), 803-810.
190. Plimpton, S., Fast Parallel Algorithms for Short-Range Molecular Dynamics. *Journal of Computational Physics* **1995,** *117* (1), 1-19.
191. Wyatt, P. J., Light-Scattering and the Absolute Characterization of Macromolecules. *Anal Chim Acta* **1993,** *272* (1), 1-40.
192. Lima, A. M. D.; Wong, J. T.; Paillet, M.; Borsali, R.; Pecora, R., Translational and rotational dynamics of rodlike cellulose whiskers. *Langmuir* **2003,** *19* (1), 24-29.
193. Pitkanen, L.; Striegel, A. M., Size-exclusion chromatography of metal nanoparticles and quantum dots. *Trac-Trend Anal Chem* **2016,** *80*, 311-320.
194. Hamielec, A.; Styring, M., Recent Advances in the Characterization and Analysis of Polymers and Polymer Particles by Size Exclusion Chromatography. *Pure Appl Chem* **1985,** *57* (7), 955-970.
195. Striegel, A. M., *Modern size-exclusion liquid chromatography : practice of gel permeation and gel filtration chromatography*. 2nd ed.; Wiley: Hoboken, N.J., 2009; p xvi, 494 p.
196. Stegeman, G.; Kraak, J. C.; Poppe, H., Hydrodynamic and Size-Exclusion Chromatography of Polymers on Porous Particles. *J Chromatogr* **1991,** *550* (1-2), 721-739.
197. Guillaume, Y. C.; Robert, J. F.; Guinchard, C., A mathematical model for hydrodynamic and size exclusion chromatography of polymers on porous particles. *Anal Chem* **2001,** *73* (13), 3059-3064.
198. El Seoud, O. A.; Nawaz, H.; Areas, E. P. G., Chemistry and Applications of Polysaccharide Solutions in Strong Electrolytes/Dipolar Aprotic Solvents: An Overview. *Molecules* **2013,** *18* (1), 1270-1313.
199. Brun, Y.; Rasmussen, C. J., Interaction Polymer Chromatography. In *Liquid Chromatography - Fundamentals and Instrumentation*, 2017; pp 275-318.
200. Brun, Y., Data Reduction in Multidetector in SEC for Molar Mass Sensitive Detectors. *ACS Symposium Series* **2005,** *893*, 281-301.
201. Nordmeier, E., Static and Dynamic Light-Scattering Solution Behavior of Pullulan and Dextran in Comparison. *J Phys Chem-Us* **1993,** *97* (21), 5770-5785.
202. Vankreveld, M. E.; Vandenhoed, N., Mechanism of Gel-Permeation Chromatography - Distribution Coefficient. *J Chromatogr* **1973,** *83* (Aug29), 111-124.
203. Al-Bokari, M.; Cherrak, D.; Guiochon, G., Determination of the porosities of monolithic columns by inverse size-exclusion chromatography. *J Chromatogr A* **2002,** *975* (2), 275-284.

204. Miyabe, K.; Guiochon, G., Characterization of monolithic columns for HPLC. *J Sep Sci* **2004,** *27* (10-11), 853-873.
205. Parker, R.; Ring, S. G., Aspects of the physical chemistry of starch. *J Cereal Sci* **2001,** *34* (1), 1-17.